Imperial College London
Department of Physics

Constraining theories of modified gravity with atom interferometry

Dylan Owusu Achiew Banahene-Sabulsky

Submitted in part fulfillment of the requirements for the degree of
Doctor of Philosophy in Physics of Imperial College London
London, United Kingdom
May 2018

Abstract

Matter-wave interferometry is ideal for detecting small forces, being able to sense changes of acceleration as small as 1 nm s^{-2} as a result of quantum interference. In this thesis, I prepare a cloud of ultracold ^{87}Rb atoms and measure the force between an atom and a cm-sized source mass using atom interferometry. The interferometer uses a sequence of optical Raman pulses to split, reflect, and recombine the atomic wavefunction. The force that is measured is consistent with standard Newtonian gravity. Some theories that have been advanced to explain the accelerating expansion of the universe - otherwise known as dark energy - predict a departure from the Newtonian force in my experiment. I use my result to constrain the parameters of these theories. The sensitivity of the experiment is sufficient to probe physics at energies approaching the Planck scale.

Declaration

I declare that the contents of this thesis are entirely my own doing; contributions from other sources are acknowledged and cited.

Contents

Abstract i

Declaration i

List of Tables vii

List of Figures ix

1 Introduction 1

2 Atom interferometer theory 7

2.1 Principle of the atom interferometer 7

2.2 Description of the proposed acceleration 16

3 The apparatus 20

3.1 The vacuum system 20

3.1.1 3D MOT Chamber 23

3.2 The Laser system 26

3.2.1 The MOT laser system 27

3.2.2 The Interferometer laser system . . . 34

3.3 Optics, Imaging and Detection . . . 37

3.3.1 2D and 3D MOT optics . . . 37

3.3.2 Interferometer beam collimator and optics . . . 38

3.3.3 CCD camera and optics . . . 39

3.3.4 Photodetector, noise limits and optics . . . 40

3.4 The 3D MOT and Sisyphus cooling . . . 42

3.4.1 Shim electromagnets and field control . . . 42

3.4.2 Temperature and number measurements . . . 43

3.5 The Honeywell QA-750 MEMS Accelerometer and vibration isolation . . . 46

3.5.1 Electronics . . . 46

3.5.2 Vibration isolation . . . 47

3.6 The source mass . . . 48

3.6.1 Light scatter tests . . . 51

3.7 Computer control system, sequencing and pattern generation . . . 54

4 Setting up the interferometer **60**

4.1 Studies with Co-propagating Raman beams . . . 62

4.1.1 Rabi flops and Raman Spectroscopy . . . 62

4.1.2 Ramsey Interferometry . . . 68

4.1.3 Ramsey's method with frequency and phase scanning . . . 70

4.1.4 Spin Echo Interferometry . . . 73

4.2 Studies with Counter-propagating Raman beams . . . 74

4.2.1 Velocity selection . . . 74

4.2.2 Checking the applied phase accuracy with the atom interferometer . . . 76

4.2.3 Calibrating the MEMS accelerometer with the atom interferometer . . . 80

5 Primary experiment **85**

5.1 Explanation of the experiment and the run pattern . . . 85

5.2 The primary result . . . 89

5.3 Constraints on Chameleon Gravity . . . 98

6 Conclusion **107**

6.1 Summary of achievements . . . 107

6.2 Improvements for future work . . . 108

A Magnetic field sensitivity **112**

B SI to GeV conversion **114**

C Symmetron constraints **116**

Bibliography **117**

List of Tables

5.1 MEMS accelerometer voltages for the primary experiment. 91

B.1 SI to GeV conversions 114

List of Figures

2.1 Principle of the interferometer 8

2.2 Energy level scheme for Raman transitions 9

2.3 Light shifts in kHz versus detuning of ω_1 from the interval $g \leftrightarrow 5P_{3/2}(F' = 3)$ . . 14

2.4 Light shift Δ_{eg} of the hyperfine interval versus detuning of ω_1 from the interval $g \leftrightarrow 5P_{3/2}(F' = 3)$ 15

2.5 Intensity ratio as a function of the frequency at which the light shift of the hyperfine interval is zero 15

2.6 Probability of spontaneous scattering by an atom during the time of a π pulse . 16

2.7 Experiment schematic 19

3.1 Schematic representation of the vacuum system and surrounding optical elements 21

3.2 In-vacuum 3D MOT Electromagnet profile 25

3.3 In-vacuum 3D MOT electromagnet 26

3.4 Laser system for cooling, trapping, and detection 27

3.5 Acousto-optical modulator and fiber splitting tray 30

3.6 Colinear Polarization Spectrometer and the reference laser 31

3.7 Repump laser 6.6 GHz frequency offset lock for addressing the dark hyperfine ground state . . . 32

3.8 Cooling laser 220 MHz frequency offset lock for laser cooling and trapping . . . 33

3.9 Schematic view of the commercial μQuans UKUS . . . 35

3.10 Raman laser intensity ratio and phase noise trials . . . 37

3.11 Interferometer and detection optics . . . 40

3.12 Femto photodiode noise figures . . . 41

3.13 Electronics for controlling the magnetic field . . . 43

3.14 Shim field trials . . . 44

3.15 TOF temperature measurements for the 3D MOT and Sisyphus cooling . . . 45

3.16 QA750 MEMS vibration trials . . . 48

3.17 Source mass geometry . . . 49

3.18 Source mass angles and the force projection factor . . . 50

3.19 Light scatter near the source mass . . . 53

3.20 Schematic experiment run pattern . . . 56

3.21 Detection scheme . . . 57

3.22 Experiment control and block diagram . . . 59

4.1 Co- and counter- propagating geometry . . . 61

4.2 Co-propagating Rabi Flop and Raman Spectroscopy . . . 64

4.3 Co-propagating Raman Spectroscopy of F=1 . . . 65

4.4 Scalar, vector and tensor total light shift schematic . . . 66

4.5 Doppler-insensitve Raman Spectroscopy of F=1 at different magnetic fields . . . 67

4.6 Transitioning from Lin⊥Lin to circular polarization . . . 67

4.7 Preparing the cloud in $|1,0\rangle$ . . . 69

4.8 Clearing of states . . . 69

4.9 Co-propagating Rabi flops at multiple fall times . . . 70

4.10 Ramsey's method: scanning the frequency of both pulses . . . 71

4.11 Ramsey's method: scanning the phase between the pulses . . . 72

4.12 Velocity-insensitive spin echo interferometry . . . 73

4.13 Counter-propagating Raman spectroscopy and Rabi flopping with two velocity classes . . . 75

4.14 Single velocity selection . . . 76

4.15 Atom interferometry with two velocity classes and circularly polarized light . . . 77

4.16 Single velocity class atom interferometry . . . 78

4.17 Comparison of velocity selection techniques . . . 79

4.18 Velocity selection sensitivity comparison . . . 80

4.19 Response of MEMS electronics . . . 81

4.20 Atom interferometer correlation with MEMS accelerometer . . . 82

4.21 Big tilt trial . . . 83

5.1 Experiment strategy . . . 86

5.2 Experiment run pattern . . . 86

5.3 Raw data from one run of the primary experiment . . . 89

5.4 Sample of primary experiment data 90

5.5 Determining a_{ball} 92

5.6 Source mass magnetism test 95

5.7 Size limit for size parameter L 100

5.8 Contour plot showing the size-limited regime versus pressure-limited regime for ϕ_{bg} 101

5.9 Contour plot showing ϕ_{bg} and the screening regimes of λ_1, λ_2 102

5.10 Chameleon constraints on Λ versus M from this thesis, $n = 1$ model 103

5.11 Constraints on Chameleon gravity 104

6.1 Delay time trials 109

C.1 Constrained symmetron parameter space 116

Chapter 1

Introduction

"Cosmologists are often in error, but never in doubt."

and

"It is important to do everything with passion, it embellishes life enormously."

Lev Landau

Motivation and Objectives

In this thesis, I describe an experiment to measure the force between a neutral atom and a test mass. The motivation is to place constraints on theories of modified gravity that aim to explain the accelerating expansion of the universe and the uneven distribution of light and matter within it - dark energy.

A new scalar field provides a natural explanation, but that should produce a new "fifth" force; experiments ranging from the laboratory to the solar-system find no such force. This apparent contradiction can be understood if the properties of the scalar field vary with the local mass density so that the force becomes weak in regions of high mass density. The field would then go undetected in terrestrial and solar system experiments [1, 2] using macroscopic test masses, while still allowing the pressure associated with the field to drive the accelerating expansion of

the universe. It is now known [3] that individual atoms are small and light enough that they do not suppress this force and can therefore be used to detect the field. To accomplish this, I design and build an atom interferometer and use it to search for small accelerations of rubidium atoms in the scalar field gradient near a test mass.

I present 5 chapters detailing my work with my advisor Prof. E. A. Hinds FRS; I first need to motivate how an atom interferometer is sensitive to accelerations, presented in chapter 2. I also briefly discuss the supposed scalar fields and how they can be measured. Following this, I begin to present the results of my thesis. In chapter 3, I describe the experimental setup. I demonstrate my ability to make an acceleration-sensitive interferometer by starting with spectroscopy using co-propagating Raman beams in chapter 4. In chapter 5, I present the primary experiment and my result. I conclude with chapter 6 and comment on how the experiment could be improved.

The author worked alone on the topics presented in this thesis; the use of 'I' in this thesis expresses this. All optical components used in the figures of this work were supplied by the GW optics component library [4].

Atom interferometry

In this thesis I use atom interferometry where the internal energy states are coupled to the external momentum states through a Raman transition [5]. Atom interferometry with internal energy states was a consequence of high-resolution spectroscopy insomuch that it was discovered from a search for an optimal combination of sub-Doppler [6] and Ramsey [7] techniques. Traditionally, the external motion of atoms was successfully treated by classical physics; the exchange of momentum during emission and absorption of photons by atoms and molecules is a coupling between the internal and external degrees of freedoms that has required a quantum mechanical treatment to understand [8, 9]. I address the interferometric technique explicitly in chapter 2 and demonstrate the steps leading to my experimental realization in chapter 4.

After the first experimental realization of a cold atom gravimeter using atom interferometry in

the 1990s [5], this high-sensitivity technique was usefully applied to measurements of the fine structure constant [10], the gravitational constant G [11,12], and higher order terms associated with general relativity [13,14]. The experiment in this thesis is an addition to this list of precise, fundamental tests.

Aside from fundamental physics applications, atom interferometry has demonstrated measurements of rotations and acceleration with high precision and accuracy, which can lead the way to a new generation of gyroscopes, gravity gradiometers and absolute gravimeters [15–17]. Once incorporated into navigation suites, these devices could make dead-reckoning navigation viable. This technology is currently being commercialized. The author acknowledges generous funding from both the European Union through the Marie Sklodowska Curie Early Stage Researcher program, the Action-Initial Training Network: Frontiers in Quantum Technology (FP7/2007-2013), and the Dstl.

A brief introduction to dark energy

The direct evidence for the existence of dark energy [18] is observational. There are three points of observational evidence that have led to the conclusion there is a dark energy. (i) Luminosity distance and constraints from supernovae: In 1998, two groups pointed out the accelerating expansion of the universe based on the observation of luminosity distances of redshifted Type Ia supernovae [19, 20]. The use of the luminosity distance as a standard was born out of the need to measure distances in an expanding universe; one way of defining distance is through the luminosity of a stellar object. Type Ia supernovae are observed when white dwarf stars exceed the Chandrasekhar mass limit and explode. It is believed that these supernovae form in the same way irrespective of their location in the universe, so they should have some common absolute magnitude *independent* of redshift; this has led to their treatment as an ideal standard for luminosity. After examining low and high redshift supernovae in the late 1990s, an anomaly was found; to explain the observed redshifts, the universe had to be dominated by an energy density other than matter [18]. In 1998, Perlmutter *et al.* of the supernova cosmology project

(SCP) found that about 70% of the energy density in the present universe consists of dark energy [19]. In 2004 Riess *et al.* [21] found that the universe exhibited a transition from deceleration to acceleration at the $> 99\%$ confidence level using data from the Hubble Space Telescope.

(ii) Age of the universe and the cosmological constant: Comparing the age of the universe and the age of the oldest stellar population presents evidence for a dark energy. First, the age of the oldest stellar objects has been constrained [22–24] to 12.7 ± 0.7 Gyr, implying the age of the universe need satisfy the lower bound: $> 11 - 12$ Gyr. Assuming a ΛCDM model, the standard model of cosmology where the equation of state of dark energy is assumed constant, WMAP3 data produces a best fit value for the age of universe of $13.73^{+0.13}_{-0.17}$ Gyr [25]. Calculating the age of the universe from the Friedmann equation [18] with the cosmological constant absent gives $2/(3H_0)$, where H_0 is the present Hubble parameter. This parameter is constrained to be $H_0^{-1} = 9.776h^{-1}$ Gyr for $0.64 < h < 0.80$ from the observations of the Hubble Space Telescope Key project [26]. While this Hubble parameter is consistent with the conclusions of the cosmic microwave background or CMB [25] and redshift studies of large scale structures or galaxy clustering [27, 28], it produces an age of the universe in the range $8 - 10$ Gyr, which fails to satisfy the stellar age bound; a flat universe without a cosmological constant suffers from an age hierarchy problem! This problem can be solved in a flat universe model by the addition of a cosmological constant [18]. The essential idea is that the age of the universe increases as the proportion of energy density in the universe from matter *decreases*. If one takes 70% of the energy density in the present universe to consist of dark energy [19] and a choice of $h = 0.72$ [18], one obtains an age of the universe of 13.1 Gyr, entirely consistent with the lower bound set by the oldest stellar populations. The presence of a cosmological constant and a dark energy can solve the universe age crisis.

(iii) The CMB and large scale structure constraints: The observations of the CMB [25] and large scale structure [27, 28] independently support a dark energy dominated universe. The CMB anisotropies exhibit a nearly scale-invariant spectra of primordial perturbations; this agrees with the predictions of inflationary cosmology. Large scale structure redshift surveys find that a dark energy just like that required by the CMB and supernova data is required to

explain their findings. These datasets rule out a flat universe without a cosmological constant and support a dark energy.

This cosmological constant, Λ, was introduced by Einstein in 1917 as a simple solution to achieve a static universe. Later, in 1929, with Hubble's discovery of the expanding universe, Einstein dropped the term as it was no longer required. However, the cosmological constant arises naturally as an energy density of the vacuum in particle physics. If it originates from the vacuum energy density, the energy scale of Λ should be much larger than that of the present Hubble constant H_0. This is the cosmological constant problem [29] and was well known before the discovery of the accelerating expansion of the universe in 1998. There have been a number of theoretical attempts to solve this problem; a short and incomplete list of attempts, with an eye towards the focus of this thesis, include: changing gravity [30], quantum gravity [31], higher-dimensional gravity [32], super gravity [33], and space-time foam [34]. In this thesis, I test two theories from one particular class of scalar field model of dark energy. Scalar fields occur naturally in particle physics, including string theory; these can act as dark energy candidates. I focus on a class of model called Quintessence [18] that is described by a scalar field minimally coupled to gravity but that can lead to the present inflation. Astrophysical bounds discussed above imply such that the simplest theories with scalars must have matter couplings irrelevant on cosmological scales. Further, the ΛCDM model may not be correct. If a scalar field is responsible for dark energy, the equation of state for dark energy can be dynamical instead of a constant. It is then critical to distinguish between the cosmological constant and dynamical dark energy models in order to understand the origin of this energy density. The link between cosmological scalar theories and astrophysical bounds can be broken by the introduction of what are called screening mechanisms.

These screening mechanisms employ non-linear dynamics to decouple solar system scale tests from cosmological scale tests of gravity. The key is in order of magnitude comparison of density: there are 29 orders of magnitude that separate terrestrial and cosmological densities. Further, there are 20 orders of magnitude separating their distance scales! As a result, the scalar field properties can vary significantly in different environments. The classic example of a screening mechanism is the chameleon mechanism [1] where the mass of the scalar is an increasing function

of the ambient density, allowing it to have a sub-micron Compton wavelength in the solar system but remain light on cosmological scales. A closely related model was discovered, the symmetron mechanism [35], which maintains a light mass on all scales. It screens by driving the coupling to matter to zero when the ambient density exceeds a certain threshold.

Burrage *et al.* [3] proposed a method of measuring a force coming from the gradient of these theoretical scalar fields; their realization was that individual atoms are small and light enough that they are not entirely screened and can therefore be used to detect the presence of a field. In chapter 2, I present a schematic for the measurement I perform and how it is sensitive to the scalar fields. I outline how an acceleration measurement constrains the two primary parameters of the field theories. In chapter 5, I present my result that is in agreement with Newtonian gravity. I apply this result to the chameleon field theory, which allows me to directly constrain the two parameters of the theory. I compare to other measurements, in the parameter space I've considered. I briefly comment on the symmetron at the end of chapter 5 and provide constraints that I place on that theory in appendix C.

Chapter 2

Atom interferometer theory

In this chapter, I provide a theoretical description of the atom interferometer I operate in this thesis. Following this, I discuss the polarization selection rules, the light shift, and spontaneous emission. I conclude with a brief discussion of the scalar field theories that I probe with this experiment.

2.1 Principle of the atom interferometer

In Fig. 2.1, I illustrate the principle of the ^{87}Rb atom interferometer I use in this thesis. I label the two $5S_{1/2}$ hyperfine ground states of ^{87}Rb as $|g\rangle$ for $F = 1$ and $|e\rangle$ for $F = 2$. The atom starts in the state $|g\rangle$ at a position z_1, where I apply a $\pi/2$ optical Raman pulse that splits the atomic wavefunction into an equal superposition of $|g\rangle$ and $|e\rangle$. This Raman transition is driven by counter-propagating light beams with frequencies ω_1 and ω_2; the absorption of a photon at frequency ω_1 together with a stimulated emission at frequency ω_2 drives the transition to state $|e\rangle$. This process transfers momentum $\hbar k_{\text{eff}} = \frac{\hbar}{c}(\omega_1 + \omega_2)$ to the wavefunction component in state $|e\rangle$, but there is no momentum transferred from the light to the component that remains in state $|g\rangle$. After propagating freely for a time T, the atom arrives with the $|g\rangle$ component at position z_2 and the $|e\rangle$ component at position z_3. At this point I apply a Raman π pulse that swaps the internal states and exchanges their momenta. After waiting for another free

propagation time T, the two parts of the wavefunction overlap at position z_4. Then, a second $\pi/2$ pulse closes the interferometer to produce interference fringes in the populations of $|g\rangle$ and $|e\rangle$. These fringes are sensitive to the acceleration of the atom along the direction of the Raman beams, and in this thesis I use that sensitivity to look for a non-Newtonian attraction between an atom and a test mass.

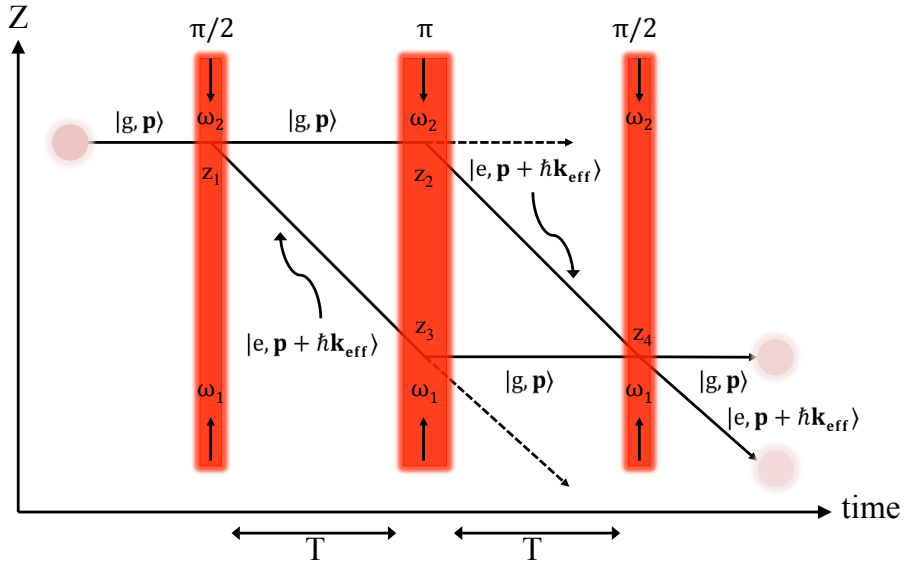

Figure 2.1: Principle of the interferometer. The interferometer evolves in time and space from left to right and top to bottom.

This scheme was first developed by Kasevich and Chu [5]. Critically, all the atoms participate in the interferometer regardless of their initial momentum p, so it is not necessary to resolve the recoil splitting that makes the interferometer sensitive to acceleration. Despite this, it is useful to make the atom cloud cold in order to minimize the Doppler broadening of the Raman transition.

In Fig. 2.2, I show the two hyperfine ground states with energies $\hbar\omega_g$ and $\hbar\omega_e$ which are separated by 6.8 GHz. The upper state, which I denote $|i\rangle$, represents the electronically excited $5P_{3/2}$ states. The laser light fields $\mathcal{E}_1$ and $\mathcal{E}_2$ are traveling waves propagating along the $\hat{z}$ direction,

$$\begin{aligned} \mathcal{E}_1 &= E_1 \cos\left(k_1 z - \omega_1 t + \varphi_1\right) \\ \mathcal{E}_2 &= E_2 \cos\left(k_2 z - \omega_2 t + \varphi_2\right). \end{aligned} \tag{2.1}$$

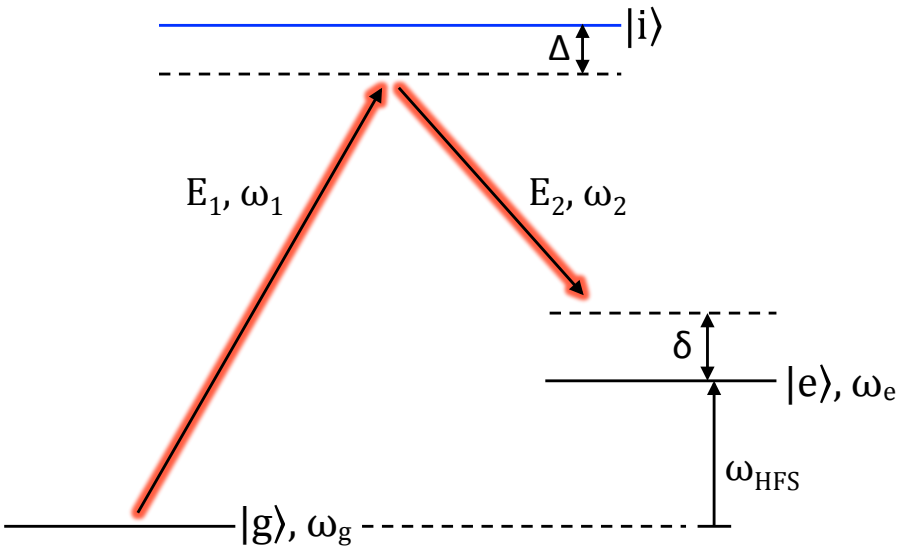

Figure 2.2: Energy level scheme for Raman transitions.

For now, I will write $k_1 z + \varphi_1 = \phi_1$ and $k_2 z + \varphi_2 = \phi_2$. I define the two Rabi frequencies as

$$\begin{aligned} \Omega_1 &= \frac{1}{\hbar}\langle i|\mathbf{d}|g\rangle \cdot \mathbf{E}_1 \\ \Omega_2 &= \frac{1}{\hbar}\langle i|\mathbf{d}|e\rangle \cdot \mathbf{E}_2. \end{aligned} \tag{2.2}$$

The light fields are at optical frequencies. In this thesis I have a detuning $\Delta \approx -1$ GHz and a δ in the kHz range. The Rabi frequencies are less than 1 MHz; thus a frequency hierarchy is established: $\omega_{1,2} \gg (\omega_e - \omega_g) \gg \Delta \gg \delta,\ \Omega_{1,2}$. With this hierarchy in place, the rotating wave and adiabatic approximations [36] allow me to eliminate the intermediate state $|i\rangle$ and consider only the two level system of $|g\rangle$ and $|e\rangle$, where transitions between the states are being driven by an effective Rabi frequency

$$\Omega = \frac{\Omega_1 \Omega_2}{2\Delta} \tag{2.3}$$

as discussed by Kasevich and Chu [37].

I write the state of the two level system in an interaction picture as

$$|\psi\rangle = a_g e^{-i\omega_g t}|\psi_g\rangle + a_e e^{-i(\omega_e+\delta)t}|\psi_e\rangle \tag{2.4}$$

with the initial state vector at time t

$$\begin{pmatrix} a_e(t) \\ a_g(t) \end{pmatrix}, \tag{2.5}$$

and let the Raman light be applied for a time τ. The state vector at a time $t+\tau$ is [7]

$$\begin{pmatrix} a_e(t+\tau) \\ a_g(t+\tau) \end{pmatrix} = e^{i\tau\delta/2}\cdot \\ \begin{pmatrix} \cos(a\tau/2) - i\frac{\delta}{a}\sin(a\tau/2) & -i\frac{\Omega}{a}e^{i\phi}\sin(a\tau/2) \\ -i\frac{\Omega}{a}e^{-i\phi}\sin(a\tau/2) & \cos(a\tau/2) + i\frac{\delta}{a}\sin(a\tau/2) \end{pmatrix} \begin{pmatrix} a_e(t) \\ a_g(t) \end{pmatrix}, \tag{2.6}$$

where $a = \sqrt{\Omega^2+\delta^2}$ and $\phi = \phi_2 - \phi_1$. For simplicity, I assume that the Raman transition is tuned to be exactly resonant, so $\delta = 0$. I then have

$$\begin{pmatrix} a_e(t+\tau) \\ a_g(t+\tau) \end{pmatrix} = \begin{pmatrix} \cos(\mathcal{A}/2) & -ie^{i\phi}\sin(\mathcal{A}/2) \\ -ie^{-i\phi}\sin(\mathcal{A}/2) & \cos(\mathcal{A}/2) \end{pmatrix} \begin{pmatrix} a_e(t) \\ a_g(t) \end{pmatrix}, \tag{2.7}$$

where $\mathcal{A} = \Omega\tau$ is known as the pulse area. The first pulse of the interferometer has duration $\tau/2$ and pulse area $\mathcal{A} = \pi/2$. So,

$$\mathcal{Q}_1 = \frac{1}{\sqrt{2}} \begin{pmatrix} 1 & -ie^{i\phi(z_1)} \\ -ie^{-i\phi(z_1)} & 1 \end{pmatrix}. \tag{2.8}$$

Here, $\phi(z_1)$ indicates the phase difference ϕ evaluated at the position z_1 of the atom. Following this is a period of free flight time of duration T with pulse area $\mathcal{A} = 0$:

$$\mathcal{Q}_2 = \begin{pmatrix} 1 & 0 \\ 0 & 1 \end{pmatrix}. \tag{2.9}$$

The second Raman pulse has a duration of τ and a pulse area $\mathcal{A} = \pi$, giving me

$$\mathcal{Q}_3 = \begin{pmatrix} 0 & -ie^{i\phi(z_2)} \\ -ie^{-i\phi(z_3)} & 0 \end{pmatrix} \tag{2.10}$$

where the component of the wavefunction in state $|g\rangle$ interacts with the second laser pulse at position z_2 but the component in state $|e\rangle$ interacts at position z_3, see Fig. 2.1. A second free flight time gives

$$\mathcal{Q}_4 = \mathcal{Q}_2. \tag{2.11}$$

The final $\pi/2$ pulse gives

$$\mathcal{Q}_5 = \frac{1}{\sqrt{2}} \begin{pmatrix} 1 & -ie^{i\phi(z_4)} \\ -ie^{-i\phi(z_4)} & 1 \end{pmatrix}. \tag{2.12}$$

If I start with the atom in state $|g\rangle$, the final state vector is described by

$$\begin{pmatrix} a_e \\ a_g \end{pmatrix} = \mathcal{Q}_5\mathcal{Q}_4\mathcal{Q}_3\mathcal{Q}_2\mathcal{Q}_1 \begin{pmatrix} 0 \\ 1 \end{pmatrix}. \tag{2.13}$$

Evaluation produces

$$\begin{pmatrix} |a_e|^2 \\ |a_g|^2 \end{pmatrix} = \begin{pmatrix} \sin^2(\Phi/2) \\ \cos^2(\Phi/2) \end{pmatrix}, \tag{2.14}$$

where $\Phi = \phi(z_1) - \phi(z_2) - \phi(z_3) + \phi(z_4)$. Recall that

$$\phi(z) = \phi_2(z) - \phi_1(z) = (k_2 z + \varphi_2) - (k_1 z + \varphi_1) = z(k_2 - k_1) + (\varphi_2 - \varphi_1). \tag{2.15}$$

Using the same value $\varphi_2 - \varphi_1$ throughout and writing $k_{\text{eff}} = k_2 - k_1$, then $\Phi = k_{\text{eff}}(z_1 - z_2 - z_3 + z_4)$. In the absence of acceleration, $z_1 - z_3 = z_2 - z_4$, and so $\Phi = 0$. If an atom has a constant acceleration a_z along the $\hat{z}$ direction, the additional differences are

$$\begin{aligned} z_1 - z_3 &= -\frac{1}{2}a_z T^2 \text{ and} \\ z_4 - z_2 &= \frac{1}{2}a_z(2T)^2 - \frac{1}{2}a_z T^2 = \frac{3}{2}a_z T^2, \end{aligned} \tag{2.16}$$

where I have neglected the small time 2τ taken up by the laser pulses. This gives $\Phi = k_{\text{eff}} a_z T^2$. A simple way to scan through the fringe pattern is to change the phase difference $\phi_2 - \phi_1$ on one of the laser pulses. For example, if the first and second pulses have $\phi_2 - \phi_1 = 0$ but the

third pulse has $\phi_2 - \phi_1 = \theta$, then the fringe pattern in state $|g\rangle$ is described by

$$|a_g|^2 = \cos^2\left(\frac{1}{2}\left[k_{\text{eff}} a_z T^2 + \theta\right]\right) \tag{2.17}$$

and I can access any part of the pattern by adjusting θ.

Polarization selection rules

A small magnetic field (on the order of 1 G) is applied parallel to $\hat{z}$, the direction of propagation of the light beams that drive the Raman transitions. This is done to ensure that the magnetic substates m_F are not appreciably mixed by any stray magnetic field along $\hat{x}$ or $\hat{y}$. The Raman light is delivered from the laser system on a polarization-maintaining fiber, with frequency ω_1 being polarized linearly along $\hat{x}$ and ω_2 being linearly polarized along $\hat{y}$. The two beams emerge from the fiber, co-propagating with this polarization which I call Lin⊥Lin.

To consider the polarization selection rules, I note that the two dipole operators that couple to these two light beams can form tensors of rank 2, 1, or 0. I will call them $T^{(k)}$, where $k = 2, 1, 0$. The Raman transition matrix elements have the form $\langle F = 2,\ m_2|T^{(k)}_q|F = 1,\ m_1\rangle$. By the Wigner-Eckart theorem, this is proportional to $\langle F = 2||T^{(k)}||F = 1\rangle$, which vanishes when $k = 0$. By uncoupling the nuclear spin, I obtain $\langle F = 2||T^{(k)}||F = 1\rangle \propto \langle J = 1/2||T^{(k)}||J = 1/2\rangle$, which vanishes when $k = 2$. The only allowed Raman transition is then the one described by the vector operator $T^{(1)}$. Since the two light fields have Lin⊥Lin polarization, the transition is driven by the vector combination $(d_1\hat{x}) \times (d_2\hat{y}) = d_1 d_2 \hat{z}$, described by $T^{(1)}_0$. This drives the $\Delta m_f = 0$ transitions $\langle F = 2,\ m_F|T^{(1)}_0|F = 1,\ m_F\rangle$.

I introduce a quarter-wave plate, allowing me to convert the polarizations of the co-propagating beams to right-hand circularly polarized light at frequency ω_1 and left-hand circularly polarized light at frequency ω_2, which I write as RHCP and LHCP. Absorption from one beam together with emission into another changes m_F by ± 2, corresponding to the operator $T^{(2)}_{\pm 2}$, which is forbidden from driving transitions as previously established. In the experiment, I retro-reflect the laser beams through a second quarter-wave plate to form counter-propagating beams with

RHCP-LHCP and LHCP-RHCP, (details in chapter 4). This now drives $\Delta m_F = 0$ transitions with the operator having the allowed vector character $T_0^{(1)}$.

In summary, the allowed transitions that I drive use either co-propagating beams with Lin⊥Lin polarization (section 4.1) or counter-propagating beams with RHCP-LHCP and LHCP-RHCP (section 4.2, driving $\sigma_+\sigma_+$ and $\sigma_-\sigma_-$ transitions). The former are not useful for measuring acceleration by interferometry because the transition imparts a negligible momentum to the atom, $\frac{\hbar}{c}(\omega_1 - \omega_2)$, so the primary experiment I present in chapter 5 uses the latter, where the recoil momentum is $\frac{\hbar}{c}(\omega_1 + \omega_2)$.

The light shift

The electric dipole interaction of the atom with the laser light drives the Raman transitions, as discussed in the last two sections. This same interaction is also responsible for an AC Stark shift, usually referred to as the light shift, which perturbs the energies of the hyperfine levels and affects the detuning of δ.

The light shift of level $|g\rangle$ is given by standard second-order perturbation theory as

$$\Delta_g = \sum_i \Big(\frac{\Omega_1^2}{4(\omega_1 - \omega_{ig})} + \frac{\Omega_2^2}{4(\omega_2 - \omega_{ig})} \Big), \tag{2.18}$$

where ω_{ig} means $\omega_i - \omega_g$. The sum is taken over all the hyperfine levels of the upper $5P_{3/2}$ manifold; I ignore the $5P_{1/2}$ upper levels because they are ~ 7 THz away. With 100 W/m^2 of circularly polarized light in each laser frequency, in a) of Fig. 2.3 I show the shift Δ_g in kHz for the state $|F = 1,\ m_F = 0\rangle$ as a function of the detuning of ω_1 from the interval $5S_{1/2}(F = 1) \rightarrow 5P_{3/2}(F' = 3)$ (as ω_1 is varied, I also change ω_2 to keep the transition resonant). I observe resonant light shifts that come from the coupling to the upper levels $F' = 2$ and $F' = 1$. There is no coupling to $F' = 3$ because it is dipole-forbidden. There is also no coupling to $F' = 0$ because the light is circularly polarized in this calculation and $F' = 0$ has no $m_{F'} = \pm 1$ states. I use circularly polarized light for this calculation because it the polarization I will use in the primary experiment in chapter 5.

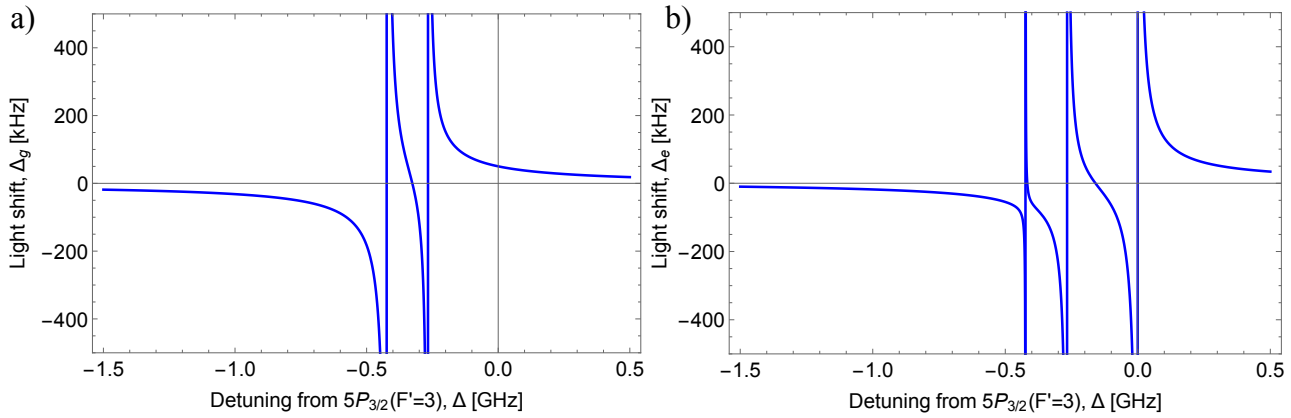

Figure 2.3: Light shifts in kHz versus detuning of ω_1 from the interval $g \leftrightarrow 5P_{3/2}(F' = 3)$. The Raman beams have 100 W/m^2 each of circularly polarized light. a) Shift of the state $|F = 1, m_f = 0\rangle$. b) Shift of the state $|F = 2, m_f = 0\rangle$.

The light shift of level $|e\rangle$ is

$$\Delta_e = \sum_i \left(\frac{\Omega_1^2}{4(\omega_1 - \omega_{ie})} + \frac{\Omega_2^2}{4(\omega_2 - \omega_{ie})} \right), \tag{2.19}$$

where ω_{ie} means $\omega_i - \omega_e$. This is plotted in b) of Fig. 2.3 versus the detuning ω_2 from the interval $5S_{1/2}(F = 2) - 5P_{3/2}(F' = 3)$, where I observe resonances in the light shift from $F' = 1, 2, 3$. The light shift of the hyperfine interval $\Delta_{eg} = \Delta_e - \Delta_g$ goes to zero near the $F' = 1$ and $F' = 3$ resonances, shown in a) of Fig. 2.4, but these frequencies are not useful for driving the two photon Raman transitions because the one photon scattering rate is high. With laser beams of equal intensity, there are no useful zeros of Δ_{eg}. A useful zero appears at a detuning of approximately -2 GHz when the beam of frequency ω_1 is half the intensity of the beam of frequency ω_2, shown in b) of Fig. 2.4.

In Fig. 2.5, I show the intensity ratio as a function of the frequency at which the light shift of the hyperfine interval goes to zero. Close to the maximum of this curve, the intensity ratio for vanishing light shift is least sensitive to variations in the detuning. At the maximum, the detuning is -1.13 GHz and the corresponding intensity ratio is 0.583. I operate the interferometer under that condition. The light shift is then calculated to be 1.6 Hz/(W/m^2) if the intensity ratio changes by 1% of itself.

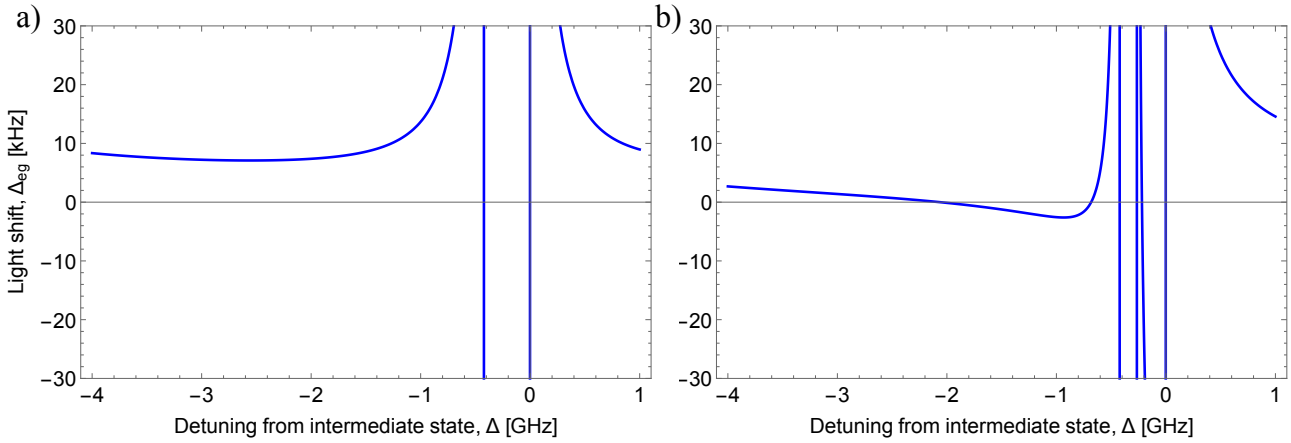

Figure 2.4: Light shift Δ_{eg} of the hyperfine interval versus detuning of ω_1 from the interval $g \leftrightarrow 5P_{3/2}(F' = 3)$. a) Both beams have 100 W/m^2 and b) 50 W/m^2 in ω_1 and 100 W/m^2 at ω_2. In b) I observe a useful zero at a detuning of approximately -2 GHz.

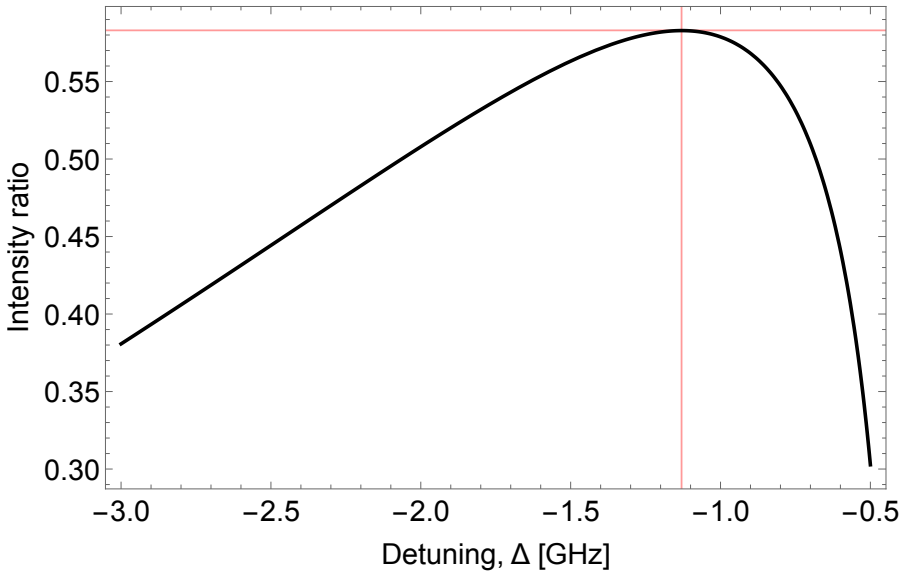

Figure 2.5: Intensity ratio as a function of the frequency at which the light shift of the hyperfine interval is zero. The red lines denote the maximum intensity ratio of .583 at -1.13 GHz.

Spontaneous scattering

The Raman pulses induce only a small population in the excited states $|i\rangle$, but still this is not entirely negligible; there is some probability that the atom will scatter a photon by spontaneous emission during a π pulse. Such a scattering randomizes the phase of the interferometer and results in a loss of visibility of the fringes. I plot the probability that an atom in the state $|F = 2,\ m_F = 0\rangle$ or $|F = 1,\ m_F = 0\rangle$ will scatter a photon spontaneously during a π pulse in Fig. 2.6. This probability is proportional to the intensity of the light and the duration of

the pulse, but the same product determines the pulse area $\mathcal{A}$; it is sufficient to specify that the pulse is a π pulse. The plot shows how this probability depends upon the detuning. This is calculated with the intensity ratio being re-evaluated to give zero light shift at each detuning. The scatter is about 2% over the range of detunings considered. In total, the three pulses of the interferometer give a pulse area of 2π, so for my detuning of -1.13 GHz I expect a net spontaneous scattering probability of approximately 5%.

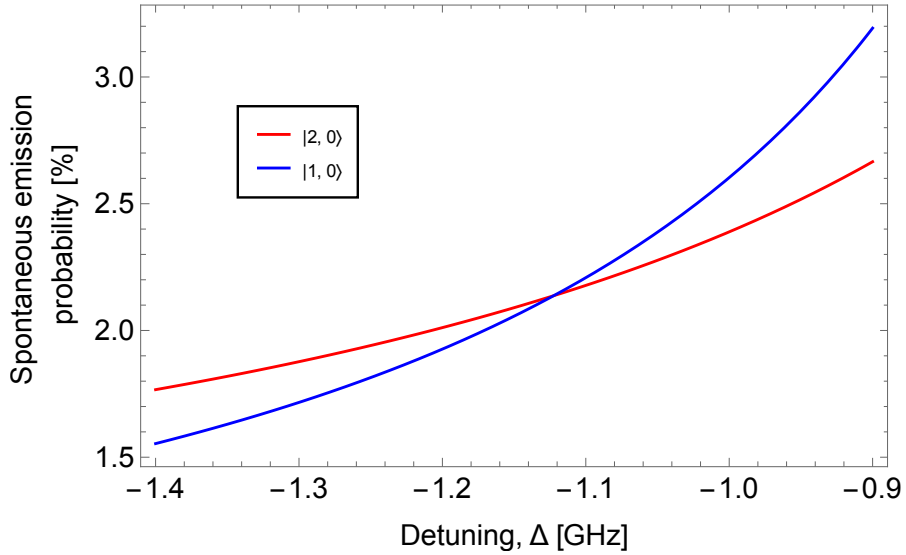

Figure 2.6: Probability of spontaneous scattering by an atom during the time of a π pulse. This is plotted versus the detuning from the excited state with the intensity ratio of the two light beams optimized at each frequency to give zero light shift. I show $|F = 2,\ m_f = 0\rangle$ in red and $|F = 1,\ m_f = 0\rangle$ in blue.

This calculation and those leading to Figs. 2.3, 2.4, 2.5, and 2.6 were done using a program written by Prof. E. A. Hinds FRS.

2.2 Description of the proposed acceleration

In order to explain the growing expansion rate of the universe, cosmologists have proposed a "dark energy". This might simply be a non-zero cosmological constant, but it could also be a result of negative pressure caused by a light scalar field. In order to avoid conflicting with fifth force experiments on Earth, it is proposed that the new field ϕ be sensitive to the density of the surrounding matter. This gives rise to the name "chameleon".

While the field ϕ is fully described by relativistic quantum field theory, the non-relativistic steady-state is simple enough:

$$\nabla^2\phi = -\frac{\Lambda^5}{\phi^2} + \frac{\rho}{M}, \tag{2.20}$$

where ρ is the local matter density, Λ sets the strength of the field self interaction, M determines the coupling between the field and matter, and where $c = \hbar = 1$ (the units are in GeV, see appendix B). A small test particle placed in a gradient of the scalar field ϕ would be subjected to a force

$$\vec{F} \propto \vec{\nabla}\phi. \tag{2.21}$$

Such a gradient is found outside a dense spherical object [3]. The acceleration of a test object (labelled 2) towards the center of a source object (labelled 1) from equation (2.21) is given by

$$a_\chi = \frac{1}{M}\frac{\partial\phi}{\partial r} = 2\lambda_1\lambda_2\Big(\frac{M_{Pl}}{M}\Big)^2\,\frac{Gm_1}{r^2}, \tag{2.22}$$

where $M_{Pl} = \sqrt{\frac{1}{8\pi G}}$ is the reduced Planck mass, m_1 is the mass of the source mass, and G is the Newtonian gravitational constant. The coefficients λ_1 and λ_2, sometimes called screening factors, describe how the field is screened by each object. These screening factors are given by

$$\lambda_i = \begin{cases} 1, \;\; \rho_i R_i^2 < 3M\phi_{\rm bg} \\ \frac{3M\phi_{\rm bg}}{\rho_i R_i^2}, \;\; \rho_i R_i^2 > 3M\phi_{\rm bg}, \end{cases} \tag{2.23}$$

where ρ_i and R_i are the density and radius respectively of object i and $\phi_{\rm bg}$ is the vacuum expectation value of ϕ in the absence of the source and test masses. When $\rho_i R_i^2 > 3M\phi_{\rm bg}$, the field is suppressed inside the object bar a thin shell near to the surface. In the case when $\rho_i R_i^2 < 3M\phi_{\rm bg}$, the field is unsuppressed even at the center of the object, so $\lambda_i \to 1$. For $\lambda_2 = 1$, the force on the test object takes the form $-\frac{m_2}{M}\vec{\nabla}\phi$; one can think about $\frac{m_2}{M}\phi$ as a potential energy for the interaction. Notably, this force should resemble gravity in that it is a $1/r^2$ attraction - which leads to these scalar field theories being classified as screened modified gravity.

This leaves $\phi_{\rm bg}$ to be evaluated. Consider a spherical vacuum vessel of radius L, with solid walls

and at UHV pressures ($\leq 10^{-9}$ mbar): the field ϕ rises from zero near the dense walls to some value $\phi_{\rm bg}$ at the center. If the chamber is sufficiently large, $\phi_{\rm bg}$ reaches some equilibrium value $\phi_{\rm eq} = \sqrt{\Lambda^5 M/\rho_{\rm vac}}$ determined by the gas density $\rho_{\rm vac}$. For small vessels, $\phi_{\rm bg} = 0.69\sqrt[3]{\Lambda^5 L^2}$ [3]. This expression is valid for $\phi_{\rm bg} < \phi_{\rm eq}$. If this condition is not satisfied, $\phi_{\rm bg} = \phi_{\rm eq}$.

The basic idea of the experiment

It is in this way that measuring an acceleration a_χ constrains Λ and M. Based on equation (2.22), I designed an experiment similar to what was proposed in Burrage *et al.* [3], see Fig. 2.7. First, I create a vacuum can with dimensions sufficiently large to satisfy the conditions necessary for the scalar field to reach the vacuum value $\phi_{\rm bg} = 0.69\sqrt[3]{\Lambda^5 L^2}$, namely that the can maintain a sufficiently large open space L in good vacuum, see dark red curve in Fig. 2.7. When perturbed by a cm scale source mass, the field creates a large gradient across the center of the chamber, see the dashed light blue curve. I place an ensemble of atoms at this point and use atom interferometry to measure their acceleration towards the ball, see the inset in Fig. 2.7. I move the source mass between two positions on opposite sides of the atom cloud. Through subtraction, this allows me to distinguish the attraction toward the source mass from other external forces. In describing this experiment, I present three chapters: first, the construction of the apparatus in chapter 3. In chapter 4, I setup the interferometer. In chapter 5, I perform the experiment discussed here and constrain the possible values of Λ and M, which are the two free parameters of the theory.

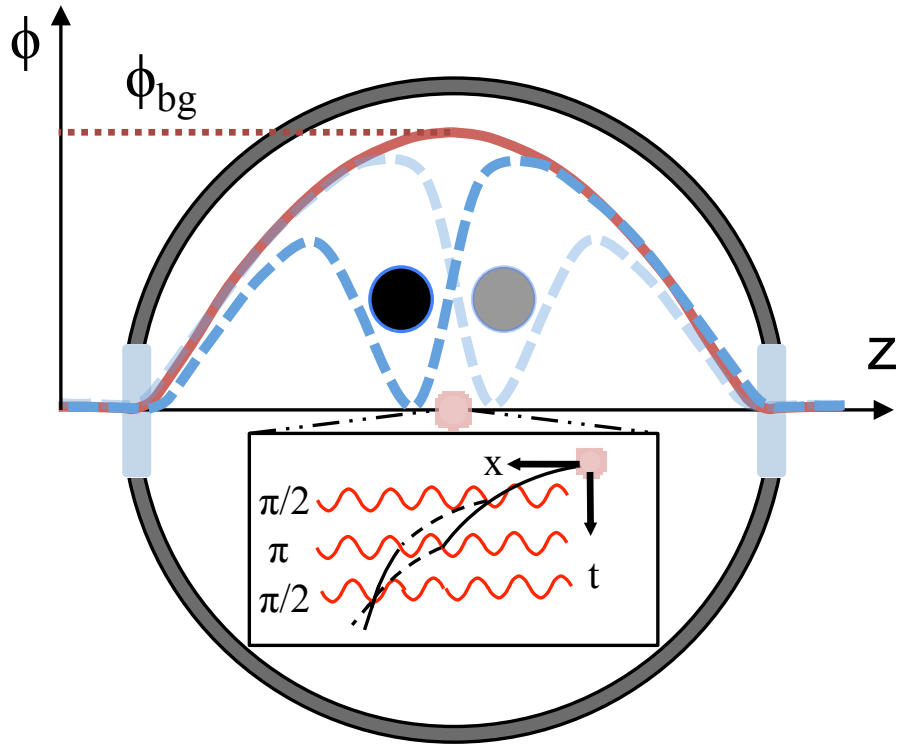

Figure 2.7: Experiment schematic. Dark red curve: unperturbed scalar field inside the vacuum chamber. Dashed blue curves: perturbed scalar field, depending on the position of the source mass. The atoms are at the center of the chamber. The source mass can take a series of positions that are equal but opposite. Inset: I measure the acceleration using an atom interferometer.

Chapter 3

The apparatus

In this chapter, I describe the experimental apparatus. First, I describe the vacuum system including the pumping arrangements and the electromagnets inside the vacuum can. Next, I discuss the lasers and describe the two parallel systems in operation: one at 780.2 nm that provides light for cooling and trapping and another, frequency-doubled, starting at 1560.4 nm for the interferometer. Shorter sections follow, describing the 2D/3D MOT optics, the interferometer optics, the CCD camera, the photodetector, and the MEMS accelerometer that I use, initially, for vibration measurements. I move on to discussions about the source mass and the installation geometry, with some focus on initial light scatter tests. Last, I describe the control system, timing, sequencing, and pattern generation for the experiment.

3.1 The vacuum system

The vacuum system for this experiment, displayed in Fig. 3.1, is composed of two smaller vacuum systems separated by a differential pumping section and a gate valve. The first system is for the 2D MOT, comprising a long, uncoated glass cell (25mm × 25 mm × 120 mm), two natural abundance electrochemical rubidium dispensers (SAES, RB/NF/4.8/17 FT10+ 10), a 2 l/s ion pump (Agilent), an all-metal angle valve, a 2 mm diameter aperture made from a copper conflat gasket, and a metal gate valve to separate it from the main chamber. The optics deliver

over 100 mW of combined cooling and repump power to the 2D MOT. The main vacuum system contains the 3D MOT capture region, the source mass, the interferometer region, and the 3D MOT electromagnets. The lower section of this chamber contains a combination Pirani/hot cathode gauge (Leybold, ITR-200), a combination diode ion pump/non-evaporable getter with μmetal shielding around the magnets (SAES, NEXTorr D-300), and a viton-sealed angle valve (MDC, good to 1×10^{-11} mbar). There are also two flanges on this chamber for electrical connections to the electromagnets. In the following subsections, I describe key parts and concepts of the vacuum system.

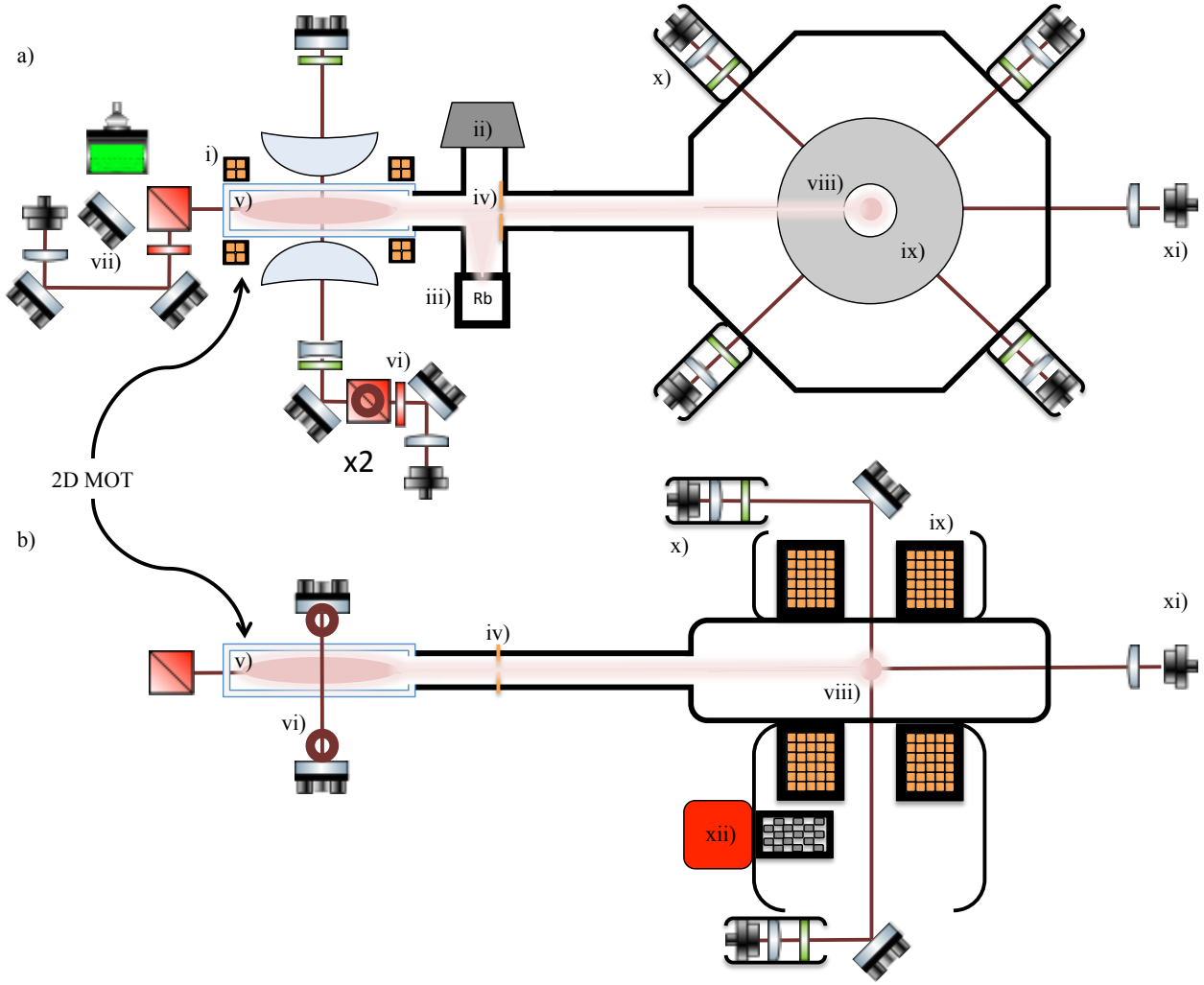

Figure 3.1: Schematic representation of the vacuum system and surrounding optical elements. a) A top down view. i) 2D MOT electromagnets, ii)2 l/s ion pump, iii) rubidium dispensers, iv) 2 mm diameter copper aperture, v) glass cell, vi) 2D MOT power splitting optics, vii) 2D MOT CCTV camera for monitoring, viii) Rb-87 MOT of $\approx 10^{10}$ atoms, ix) 3D MOT electromagnets, x) 3D MOT beam collimation tubes, xi) photodiode for detection. b)A side view of the same vacuum system. xii) SAES NEXTorr D-300 combination ion pump and NEG. The source mass has been left out of the schematic here but see Fig. 3.17 for where it fits in.

Rubidium dispensers

I use natural abundance rubidium dispensers from SAES as the source of rubidium-87 (^{87}Rb) vapor in my system, see iii) in a) of Fig 3.1. Atom interferometry with Raman transitions is more favorable with ^{87}Rb due to the magnitude of the hyperfine splitting and fewer Zeeman sublevels. While ^{87}Rb is only 28% of the vapor, a single dispenser provides sufficient vapor pressure to keep the 2D MOT loaded; the differential pumping aperture, see iv) in a) of Fig. 3.1, ensures the main chamber can maintain a low pressure of 2×10^{-10} mbar versus the 2D MOT cell at 2×10^{-7} mbar. The dispensers consist of an anhydrous rubidium salt of chromic acid, with the formula Rb_2CrO_4. The reducing agent is the ST 101 getter material, made of zirconium and aluminum (84% and 16%, respectively). This is critical to the pure dispensing of alkali metal vapor, as the ST 101 irreversibly sorbs almost all the chemically active gases produced during the reduction reaction [38]. The dispensers I installed have 4.8 mg of natural abundance rubidium each. The two dispensers are heat-sunk and electrically connected a DN16 flange that contains four copper wire feedthroughs that are rated to 12 A each. After activation, I dispense rubidium vapor at 2.5 A, continuous operation, which gives a pressure of approximately 2×10^{-7} mbar.

Differential pumping

There is 750 mm of separation from the center of the 2D MOT to the center of the 3D MOT. I aim to understand the flow of background gas from the 2D MOT cell (background loading with rubidium vapor) into the main vacuum chamber. The limiting conductance is the orifice iv) in a) and b) of Fig. 3.1, which has a radius of $r = 1$ mm. The gas is in the regime of molecular flow, where the conductance is [39]

$$C_{\text{or}} = \pi r^2 \sqrt{\frac{k_B T}{2\pi m}} = .21 \text{ l/s}, \tag{3.1}$$

where k_B is Boltzmann's constant, T is the mean temperature of the gas and m is the mass of a ^{87}Rb atom. This conductance is reduced by the tubing connecting the 2D MOT cell to

the main chamber; the tube has a length of $l = 240$ mm and a diameter of $d = 16$ mm. The conductance of a long tube is

$$C_{\text{long tube}} = \frac{d^3}{3l}\sqrt{\frac{k_B T}{2\pi m}} = .38 \text{ l/s}, \tag{3.2}$$

but for my application the ratio $l/d \approx 8$. When this ratio is below 50 equation (3.2) requires significant correction. I correct for the short length of the tube; the entrance of the duct can be considered not unlike a circuit element with resistance $Z_1 = 1/C_1$ in series with the long duct calculated above, of resistance $Z_2 = 1/C_2$, making the net conductance

$$\frac{1}{C_{\text{short tube}}} = \frac{1}{C_{\text{long tube}}} + \frac{1}{C_{\text{long tube aperture}}} \rightarrow C_{\text{short tube}} \approx 7 \times 10^{-4} \text{ l/s}. \tag{3.3}$$

Combining these two, I expect a net conductance of .14 l/s between the 2D MOT and the main chamber. The pumping speed in the main chamber is about a thousand times higher than this conductance. With the 2D MOT ion pump off during experimental operation, I expect a ratio of order 10^3, corresponding to a partial pressure of rubidium in the main chamber of order 2×10^{-10} mbar. This is consistent with the unobservable pressure increase when the rubidium dispenser is turned on.

3.1.1 3D MOT Chamber

Here I describe the 3D MOT chamber and the interior layout of the vacuum can. See Section 3.6 for information about the source mass and movement in vacuum.

UHV MOT electromagnets

In designing the 3D MOT electromagnets, I struck a balance between: (i) small electromagnets in terms of physical size and number of windings, which offer low inductance and fast switching and (ii) large electromagnets, which can leave a large open volume for the scalar field ϕ_0 to develop. To accomplish this, I had to install the 3D MOT electromagnets inside the vacuum

chamber. This added an additional concern; I had to minimize the power dissipated to ensure that resistive heating would not significantly increase out-gassing.

The Biot-Savart law describes the magnetic field on the cylindrical symmetry axis $\hat{z}$ of a single circular loop of radius r carrying a current I,

$$d\vec{\mathbf{B}} = \frac{\mu_0}{4\pi}\frac{I d\vec{\mathbf{s}} \times \hat{\mathbf{r}}}{r^2} \rightarrow B_z = \frac{\mu_0 I}{2}\frac{r^2}{(r^2+(z-z_0)^2)^{3/2}}, \tag{3.4}$$

where z_0 is the axial position. Each MOT electromagnet is a sum of circular loops

$$B_{z,\text{coil}} = \sum_{i=1}^{n_z}\sum_{j=1}^{n_r}\left(B_z\right)_{i,j}, \tag{3.5}$$

where i, j label the axial positions and radii of the nth loops, respectively. I convert this to the magnetic field gradient,

$$G_{z,\text{coil}} = \sum_{i=1}^{n_z}\sum_{j=1}^{n_r}\left(\frac{\partial B_z}{\partial z}\right)_{i,j}. \tag{3.6}$$

I can now consider physical and geometric constraints. I opted to use polyamide-imide enamel insulated copper wire with a rectangular cross-section of 2.7 mm × 4 mm. The copper wire, without insulation, has a cross section of 2.54 mm × 3.8 mm. The maximum diameter is constrained to 160 mm by the requirement of fitting within the chamber wall boundary. The minimum radius is set at 55 mm by the need for optical access as well as source mass manipulation. This limits the electromagnet to 9 turns in the radial direction, from the outer wall moving inwards. The spacing between the MOT electromagnets was chosen to be 11 cm to roughly optimize the field gradient value and shape. This left an open space defined by a sphere of radius $r = 65$ mm in which scalar fields could rise to a significant value. Fig. 3.2 shows the power dissipation as a function of the number of axial turns for an electromagnet that produces the required field gradient, for the maximum number of radial turns constrained by geometry. With 9 radial turns, the minimum power required for this field gradient is when there are 13 axial layers, dissipating only 11 W. The geometry of the chamber is convenient for in vacuum MOT electromagnets, as evidenced by b), c), and e) of Fig. 3.2; The field passes through zero near the center of the chamber. The field gradient, while it does suffer a dip near the center of

the chamber due to deviation from anti-Helmholtz configuration, see d) of Fig 3.2, reaches the designed field gradient. Over the trapping volume of ± .01 m, I can see the fluctuation is under 30 G/m; this is not problematic for a MOT. These MOT electromagnets will make a trap.

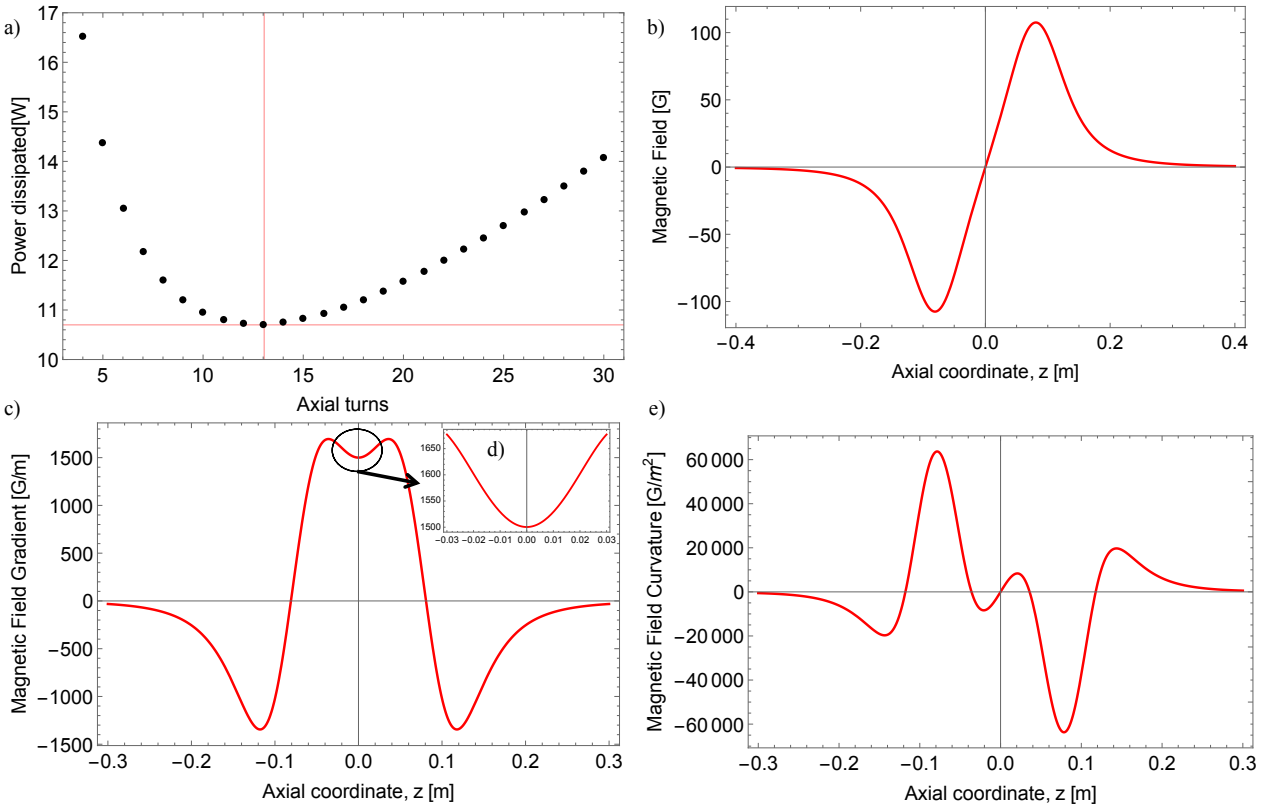

Figure 3.2: In-vacuum 3D MOT Electromagnet profile. a) Power dissipation for 1500 G/m as a function of axial turns for maximum radial turns, the red lines show the minimum at 13 axial turns and 11 W. b) Magnetic field versus deviation from the center of the chamber. The electromagnets are oriented in anti-Helmholtz configuration along z and share the midpoint of their separation distance with the center of the chamber. c) The magnetic field gradient as a function of distance from the center of the chamber. d) A closer look at the gradient near the center. e) The magnetic field curvature versus distance from the center of the chamber.

The MOT electromagnets were tested before installation, see b) in Fig. 3.3. They are 200 mΩ each with 9 radial and 13 axial turns for a total of 117 turns. The electromagnets have an inductance of 30±3 μH each. To ensure good thermal conductance from the electromagnet to the vacuum chamber and the environment, I needed a solution similar to groove grabbers (Kimball Physics, electron gun mounting) but with a larger contact surface, see a) in 3.3. During continuous operation at 11 W, a time constant of $\tau = 90$ min was measured for the electromagnets. The asymptote was 85 C. I was particularly interested in their out-gassing characteristics. A similar vacuum can to the main chamber was brought down to 10^{-8} mbar with an electromagnet

installed. During the same heating test previously mentioned, the vacuum quality degraded by a few 10^{-10} mbar; in the main chamber, this effect is only observed after 7 hours of operation, as the experiment vacuum can is a larger heat sink and the electromagnets are presumed cleaner. During interferometer operation, 10 W was used and continuous operation is rarely needed in practice.

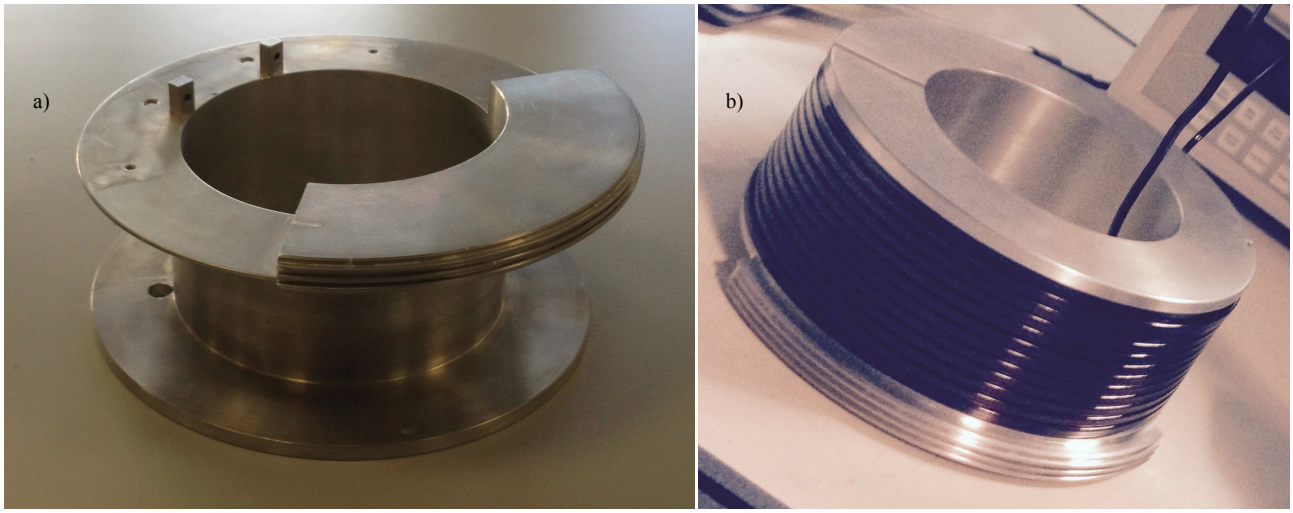

Figure 3.3: In-vacuum 3D MOT electromagnet. a) The aluminum former of the electromagnet. Also on display is one of two cooling flanges which slot directly into the grooves on the main vacuum can. b) A wound electromagnet at the conclusion of testing the profile. Note the slot in the former for eddy current suppression.

3.2 The Laser system

Here I describe the two independently referenced laser systems, Fig. 3.4 and Fig. 3.9. First, I start with the optics layout of the laser system that I assembled for cooling, trapping, and detecting the atoms. This system comprises three agile frequency-stabilized external-cavity diode lasers (ECDL) and their attendant amplifiers, all lasing on the D2 line of ^{87}Rb at 780.24 nm. This is followed by descriptions of the spectroscopy and beat note lock loops. I conclude the section by describing the unified laser system bought from μQuans, a set of four telecom C-band ECDLs lasing at 1560.48 nm. These lasers, after amplification through fiber amplifiers, are frequency-doubled via PPLN (periodically-poled Lithium-Niobate) waveguides to 780.24 nm. This is a closed commercial device; I provide information on how I used it and discuss

public knowledge on the internal workings of the device. The results of chapters 4 and 5 are a testament to the capability of the system.

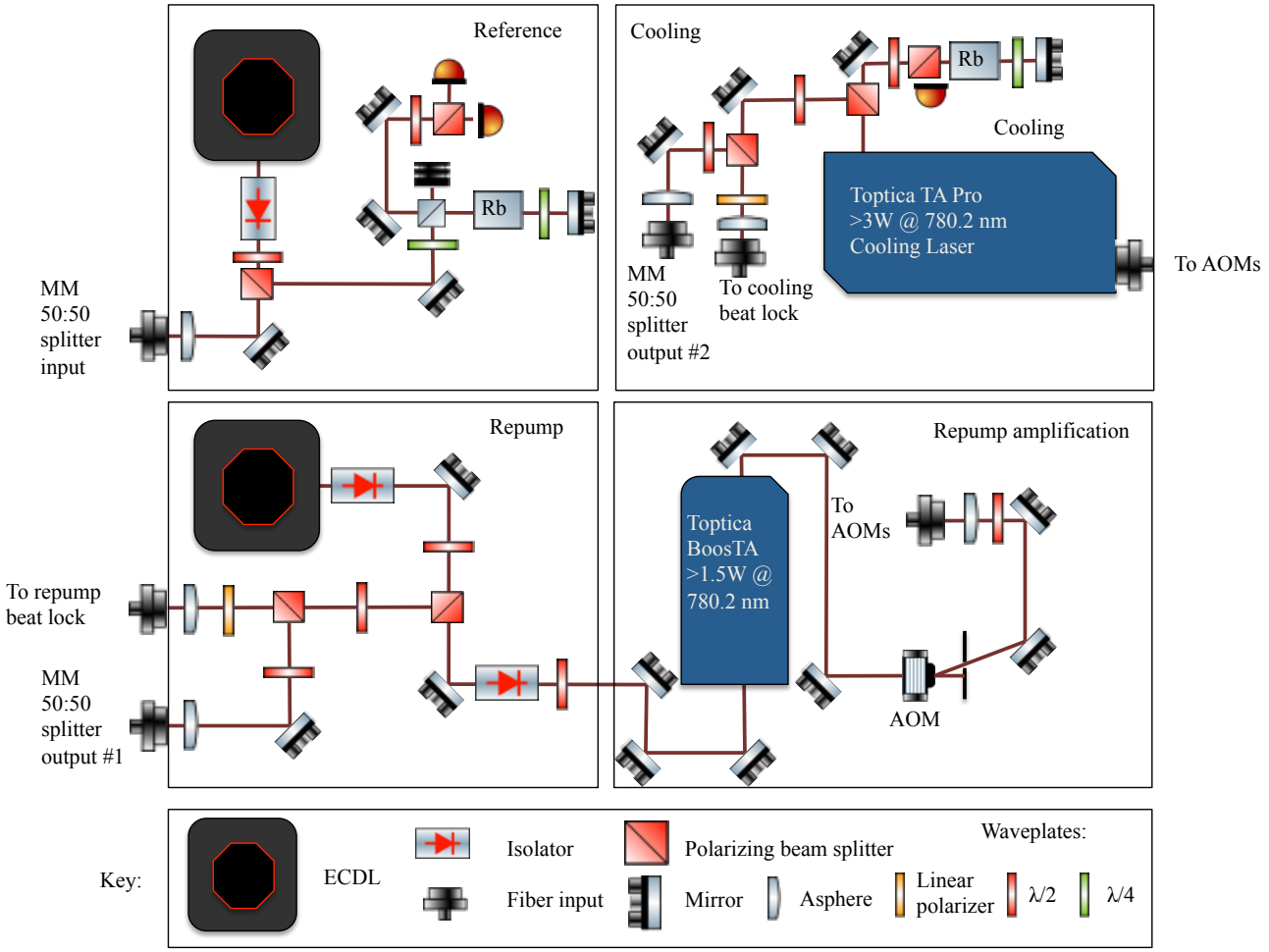

Figure 3.4: Laser system for cooling, trapping, and detection. The three lasers and their amplifiers on the table, with spectroscopy and beat note setups displayed. Note the single pass AOM after the repump tapered amplifier. The outputs labelled "To AOMs" are the inputs to Fig. 3.5.

3.2.1 The MOT laser system

The lasers for the 2D/3D MOT and detection, see Fig. 3.4, consist of three Littrow-configuration ECDLs and two tapered amplifiers. First, a stable frequency reference is required; mine is a homebuilt 3rd generation CCM Littrow-configured ECDL, known as the Sussex Design from Dr. M. G. Boshier [40]. This laser is frequency-stabilized using polarization spectroscopy, described in the next section. This laser has no current feed-forward and is locked by feeding back on the piezoelectric actuator primarily controlling the cavity length. The laser has been

upgraded and moved into a 4th generation box. The control electronics consist of a homebuilt piezostack controller as well as commercial temperature and current controllers (Wavelength Electronics). The maximum power output is 20 mW.

The second laser in the system, another Sussex Design, functions as the repump laser. This laser's function is to pump all atoms that fall into the $5^2S_{1/2}(F = 1)$ ground state into the (F=2) ground state via the $5^2P_{3/2}(F = 2)$ state. It is part of a homebuilt master oscillator power amplifier (MOPA) with a commerical tapered amplifier from Toptica Photonics, providing up to 1.5 W at 780 nm with maximum operating current and saturated optical input (20 mW). This laser can only provide 11 mW to the TA; it produces 15 mW at full current. This laser has no current feed-forward and is locked by feeding back on a piezoelectric actuator primarily controlling the cavity length. The laser has been upgraded and moved into a 4th generation box as well. The control electronics consist of a homebuilt piezostack controller and commercial temperature and current controllers. After the TA, the repump light is sent through a single-pass AOM (Gooch+Housego, M080-2B/F-GH2), see Fig. 3.4, before being fiber coupled and sent to the next stage of light management, see Fig.3.5.

The third laser is a commercial MOPA from Toptica Photonics. This device contains a Littrow configured ECDL coupled into a tapered amplifier (TA). The output of this device is fiber coupled using an additional device from the manufacturer, manually installed (please note this fiber coupler is not matched to the TA output profile, the coupler was intended for a different Toptica laser). With maximum operating current applied to the TA and saturated optical input power (40 mW), optical powers exceeding 3 W at 780.24 nm are available; the fiber coupling has been found to be 65% efficient. There is a side output from the ECDL (15 mW) for spectroscopy and locking. Full power output from the TA does not endanger the fiber, given the polarization-maintaining fiber is well coupled (from Schäfter+Kirchhoff, with metalized fiber tips). Please note that significant power couples to the fast axis of the fiber; it is dumped with polarization cleaning optics, see the input from the cooling laser in a) of Fig. 3.5. This laser is run using control electronics from the manufacturer. The original laser diode passed away early in 2016, after giving it's life gallantly in the service of science; the current feed-forward on this laser was turned off upon installation of a new diode and remains off. This

device provides the cooling force in the MOT.

The light management stage, see Fig. 3.5, consists of three AOMs (AA Opto-Electronics, MT110-A1-IR) for the cooling light, beam combining optics, and fiber coupler inputs. The AOMs are in double pass configuration for beam position stability and high extinction. They use an analog radio-frequency (RF) chain, see b) of Fig. 3.5. The AOMs are used for the following, starting from the left in a) of Fig. 3.5: (i) produces resonant $5^2S_{1/2}(F = 2) \rightarrow 5^2P_{3/2}(F = 3)$ light for the 2D MOT push beam, (ii) produces light 13 MHz red-detuned of the $5^2S_{1/2}(F = 2) \rightarrow 5^2P_{3/2}(F = 3)$ transition for the 2D MOT and (iii) produces light 15 MHz red-detuned of the $5^2S_{1/2}(F = 2) \rightarrow 5^2P_{3/2}(F = 3)$ transition for the 3D MOT. After AOM (ii) and (iii), repump light is combined with the cooling light before being fiber coupled.

The ^{87}Rb reference laser

The reference laser is frequency stabilized by deriving an error signal from a polarization spectrometer, see a) of Fig. 3.6, where birefringence is induced in an atomic vapor cell using a pump/probe interrogation technique [41]. This error signal is fed into a homemade lock loop (proportional and integral gain only) which controls the cavity length via a piezoelectric actuator. I use a rubidium vapor cell containing natural abundances of ^{85}Rb and ^{87}Rb. When the lock loop is open and the laser is set scanning near transitions in ^{85}Rb/^{87}Rb, a series of dispersive lines are observed, see b) Fig. 3.6; the lineshape is ideal for stabilizing the laser to the center of the transition. I lock to the cooling transition, colored gray in Fig. 3.6.

The polarization spectroscopy optical setup differs slightly [42] from a typical polarization spectrometer using alkali vapor cells; I do not spatially separate the pump and probe beam and then attempt to obtain good beam overlap in the cell. Instead, I employ a colinear method similar to saturated absorption setups, which suppresses sensitivity to beam misalignments. This method does not eliminate the Doppler-broadened absorption feature; instead, it creates the polarization dispersions within the larger absorption feature, see b) Fig. 3.6 and note the similarity to a typical saturated absorption spectrum for D2 ^{85}Rb/^{87}Rb, see c) in Fig. 3.9 for comparison.

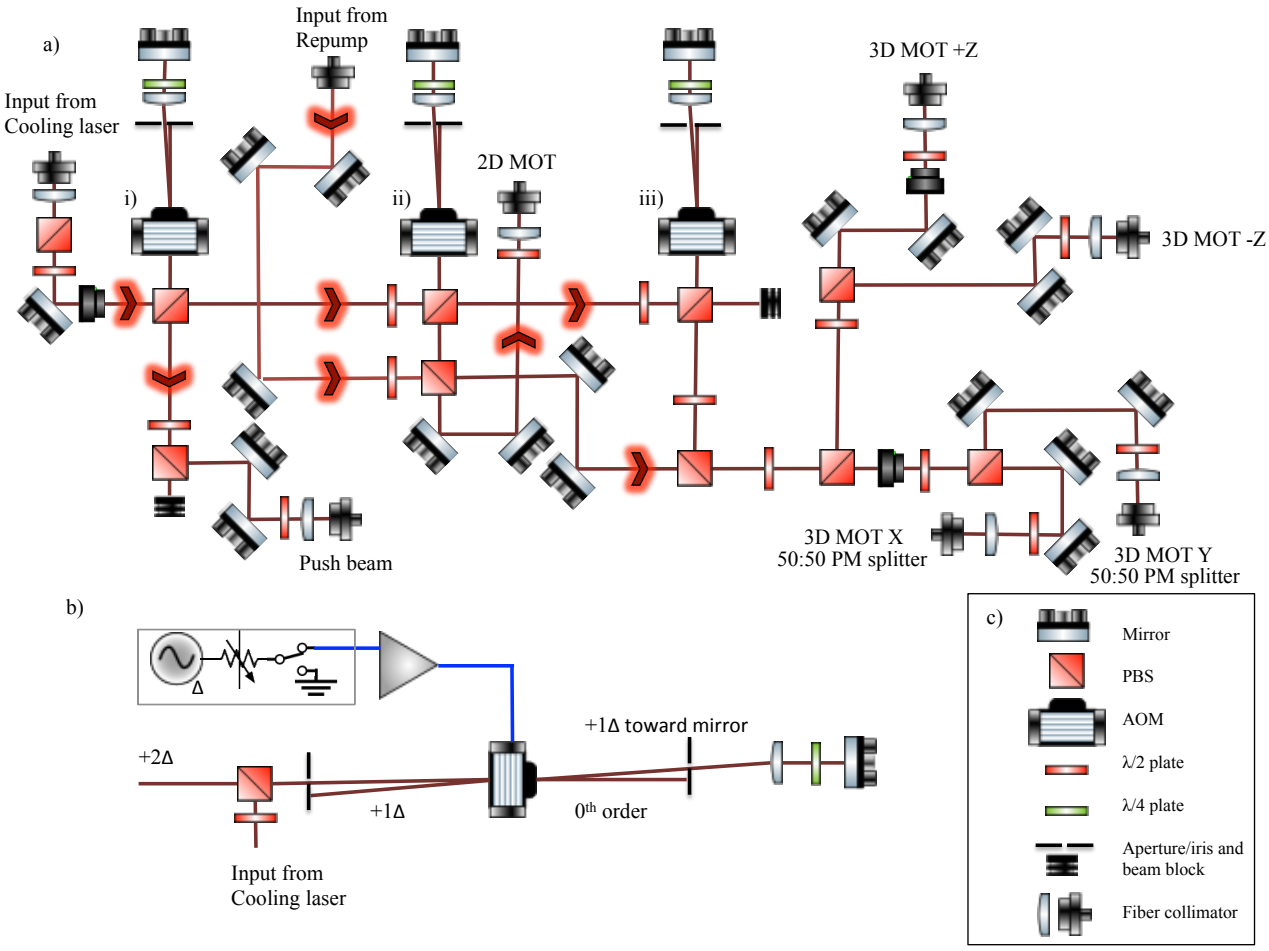

Figure 3.5: Acousto-optical modulator and fiber splitting tray. a) Layout of optics in the splitting stage. AOMs: (i) 2D MOT push beam, (ii) 2D MOT, (iii) 3D MOT. b) Schematic representation of a double-passage AOM setup. The frequency chain driving the AOMs consists of, in order of connection, a voltage-controlled oscillator (Minicircuits, ZX95-200+), a voltage-controlled attenuator (Minicircuits, ZX73-2500+), a high isolation switch (Minicircuits, ZASWA-2-50DR+), a low pass filter (Minicircuits, BLP-150+) and a power amplifier (Minicircuits, ZHL-3A+). c) A component key.

The observed zero crossings of the polarization spectrum are sensitive to magnetic fields. For this reason, the spectroscopy setup is far away (1.5 m) from the 3D MOT electromagnets and encased in a soft iron shield with only a small aperture for the light to pass through. To reduce the effects of air currents and stray light, the spectrometer is enclosed in an opaque acrylic case. It has been checked that when the electromagnets switch, no change to the error signal can be observed.

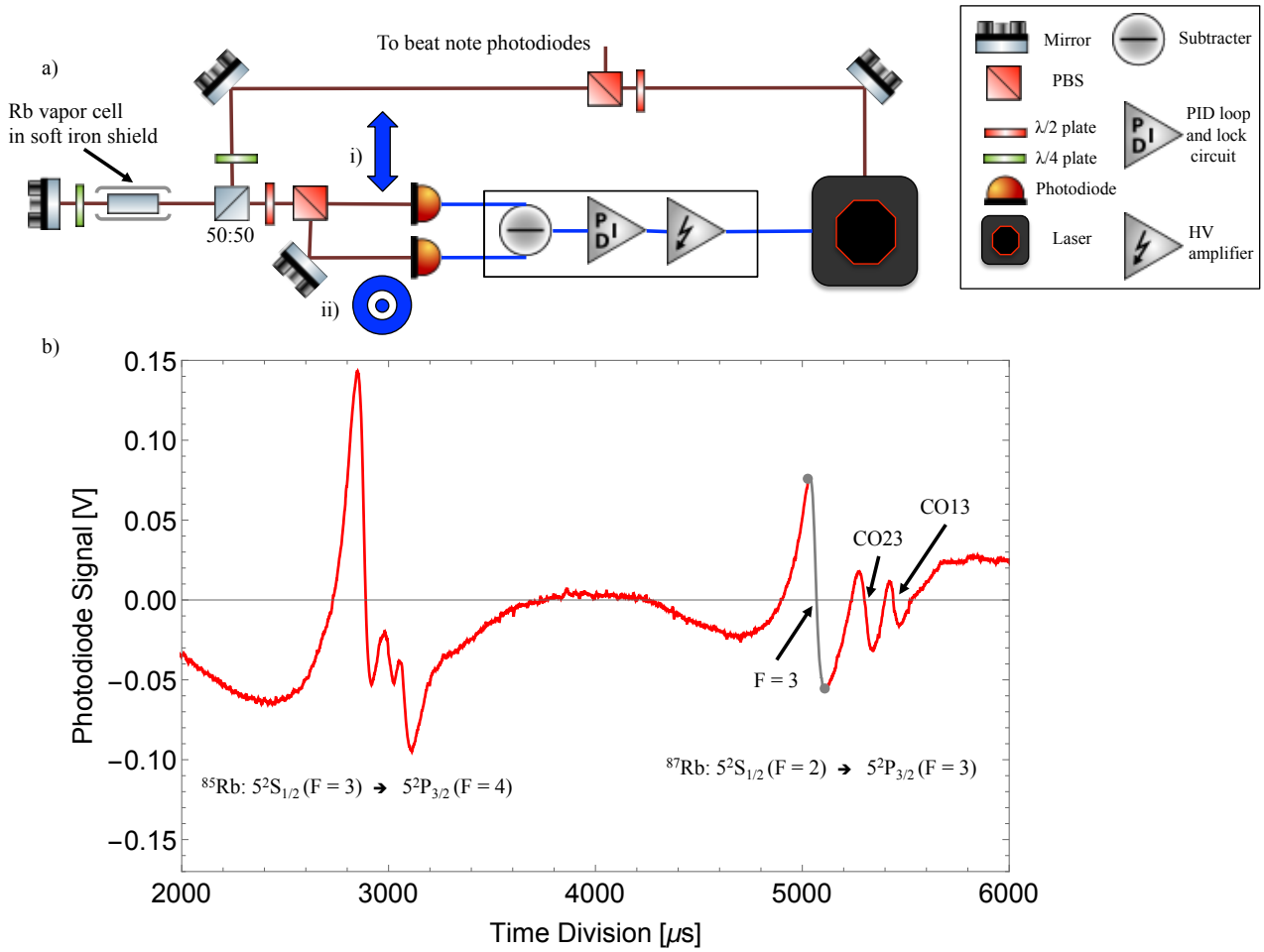

Figure 3.6: Colinear Polarization Spectrometer and the reference laser a) Schematic layout of polarization spectrometer. The PBS cube before the photodetectors splits the polarizations into i) and ii). b) A sample scan of the piezostack showing the relevant dispersion feature in gray.

The repump laser

The repump laser is frequency stabilized to the reference laser with a frequency offset beat note lock loop at 6.49 GHz. I know the frequencies of the various transitions in the D2 manifold to tens of hertz [43]; a direct microwave beat note is a suitable way to frequency stabilize the laser. A schematic of the frequency offset lock and the beat note lock loop appears in a) of Fig. 3.7. I create the beat note with 3 mW picked off from the output of the repump laser and mixed with 1 mW of light from the reference laser. The light is directed onto a fixed gain, amplified InGaAs detector (Thorlabs, PDA8GS), see the left side of a) in Fig. 3.7. While the bandwidth of this device is sufficient for the application, the sensitivity to 780 nm is low. This small signal is then inserted into two RF amplifiers chained together (Minicircuits, ZRON-

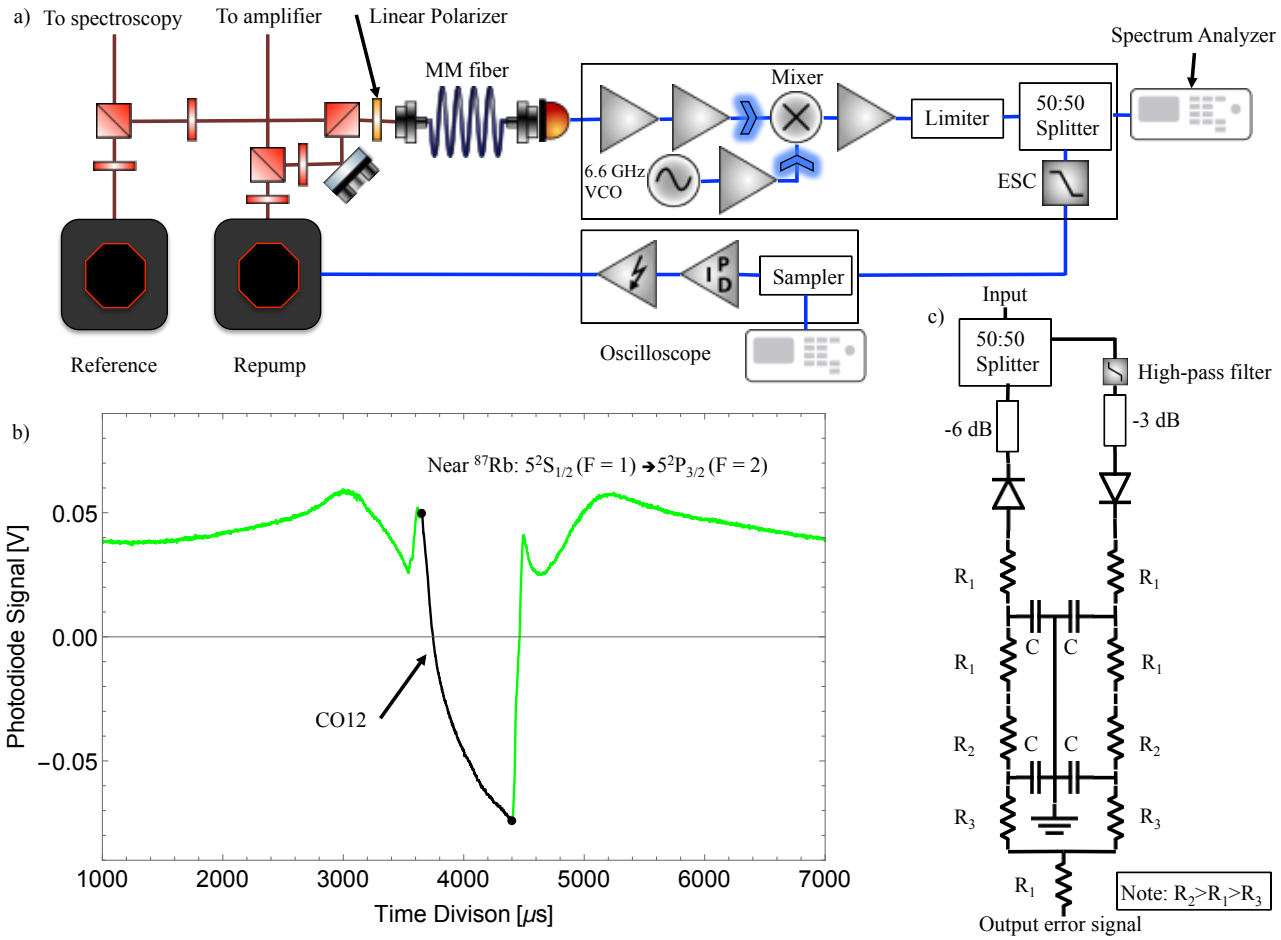

Figure 3.7: Repump laser 6.6 GHz frequency offset lock for addressing the dark hyperfine ground state. a) Schematic layout of the repump offset lock. b) Piezostack scan of the cross-over, lock point in black. c) The error signal board passive component layout [44].

8G+ and then ZVA-183-S+) before entering a mixer (ZMX-7GR). A frequency quadrupled voltage controlled oscillator (Minicircuits, ZX95-6640C-S+) amplified by a single RF amplifier (Minicircuits, ZRON-8G) feeds the other input of the mixer. The output of the mixer feeds into an amplifier (Minicircuits, ZFL-1000GR) before entering a cautionary limiter (Minicircuits, VLM-52-S+) and a splitter (Minicircuits, ZFRSC-42-S+). One splitter output goes to a 1 GHz spectrum analyzer, the other goes to the error signal card (ESC) [44], see c) of Fig. 3.7. When the piezostack of the repump laser is scanned, the dispersion signal shown in b) of Fig. 3.7 is observed.

This dispersion signal is the crossover transition $5^2S_{1/2}(F = 1) \rightarrow 5^2P_{3/2}(F = 1 \rightarrow F = 2)$. This crossover transition is 80 MHz away from the repump transition $5^2S_{1/2}(F = 1) \rightarrow 5^2P_{3/2}(F = 2)$; I use an 80 MHz AOM to shift the frequency before application to the atoms.

The cooling laser

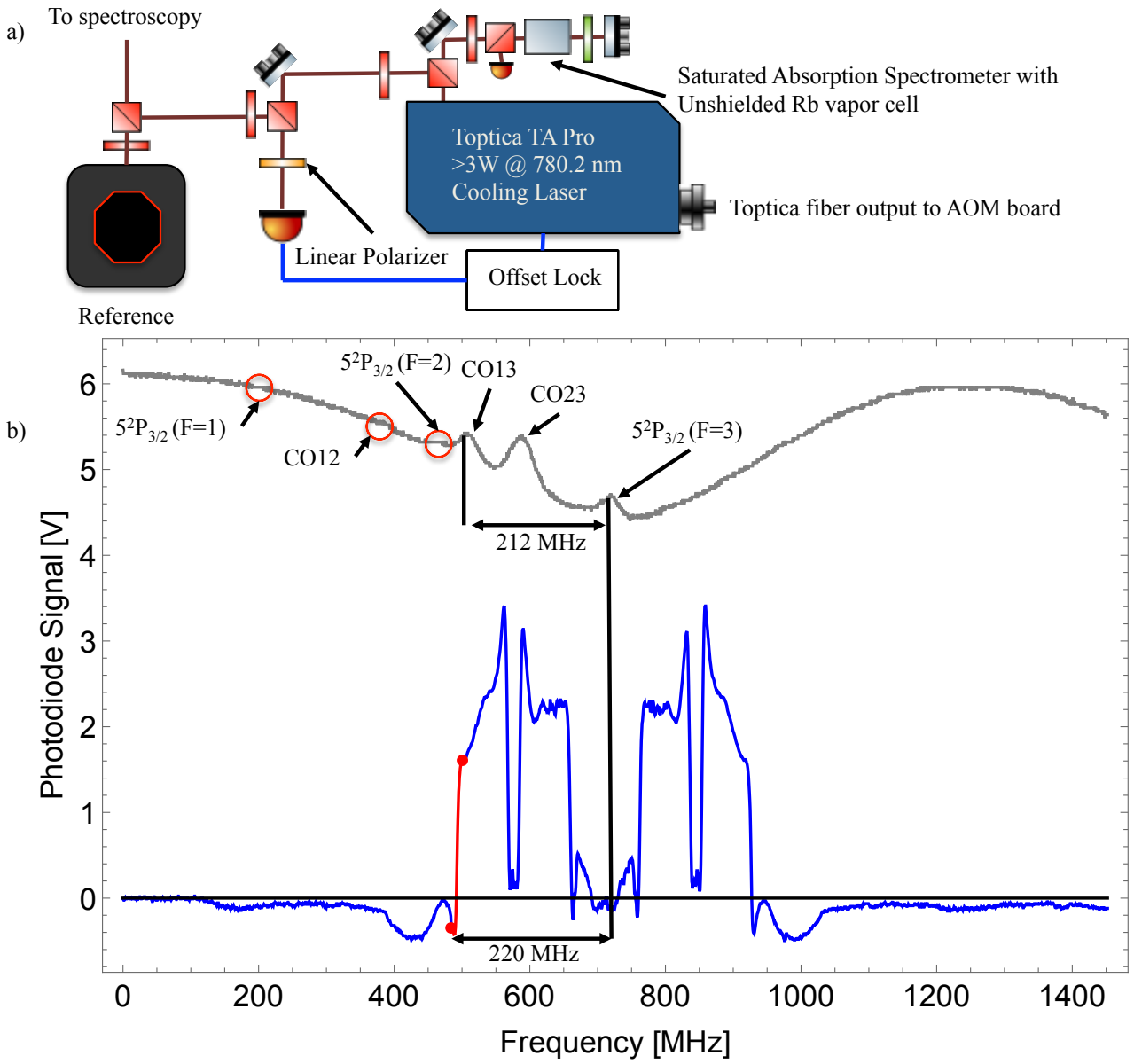

Figure 3.8: Cooling laser 220 MHz frequency offset lock for laser cooling and trapping. a) Schematic layout of the cooling offset lock and the attendant saturated absorption spectrometer for monitoring. b) Saturated absorption and error signal showing cross-over features, lock point and the relevant transition.

The cooling laser, whose function is to drive the D2 cycling transition $5^2S_{1/2}(F = 2) \rightarrow 5^2P_{3/2}(F = 3)$, is frequency stabilized with a similar frequency offset beat note lock loop with one key difference; the VCO was chosen to have a relatively linear response between tuning voltage and frequency output. Unlike the repump beat note lock, this lock requires a range of offset frequencies to allow sub-Doppler cooling. The beat note lock is operated at 220 MHz; it

was designed to be used in conjunction with a double-pass AOM, center frequency 110 MHz. The VCO (Minicircuits, ZOS-300+) allows 160 MHz of tuning.

The master oscillator has a third of the power from the ECDL picked off and sent to an auxiliary output; I use this for spectroscopy and the beat note lock, see a) of Fig. 3.8. The beam, once split, is directed into a saturated absorption spectrometer and onto a fast photodetector after overlap with the reference laser. I compare the beat note signal with saturated absorption spectrum, see b) of Fig. 3.8. The saturated absorption spectrometer produces the top of b) in Fig. 3.8 when the piezo voltage is scanned. Simultaneously, I look at the error signal from the offset lock, observing a dispersion signal symmetric about the cooling transition. Highlighted in red is the zero-crossing I use, 220 MHz below the cooling transition.

3.2.2 The Interferometer laser system

I used a Raman laser system composed of two frequency doubled, phase-locked C-band ECDLs supplied by μQuans. The μQuans Raman laser system, see a) in Fig. 3.9, consists of three 1560.4 nm ECDLs, two Erbium-doped fiber amplifiers (EDFAs), three periodically poled Lithium-Niobate frequency doubling crystals (PPLNs) and an AOM.

The output of the reference laser (at 1560.4 nm), see i) in b) of Fig. 3.9, is injected directly into the PPLN waveguide and fed into a saturated absorption spectrometer, where it is frequency stabilized to the peak of the largest crossover transition in the ^{85}Rb spectrum via lock-in amplifier, see c) in Fig. 3.9. The first interferometer laser, ii) in b) of Fig. 3.9, is frequency offset locked to the reference laser; this laser is stabilized 750 MHz red of the $5^2S_{1/2}(F = 2) \rightarrow 5^2P_{3/2}(F = 1)$ transition, see ii) in d) of Fig. 3.9. After power amplification and frequency doubling, a small amount of light is picked off for the phase lock. The second interferometer laser, see iii) in b) of Fig. 3.9, is phase locked to the first laser with a small pickoff after amplification and frequency doubling; it is frequency offset by 6.834 GHz, spanning the hyperfine splitting. The Raman laser delivers the light linearly polarized, with the slow axis containing frequency ii) and the fast axis containing frequency iii) from d) of Fig. 3.9. The power ratio of the interferometer frequencies is controlled with the EDFA settings. I found that

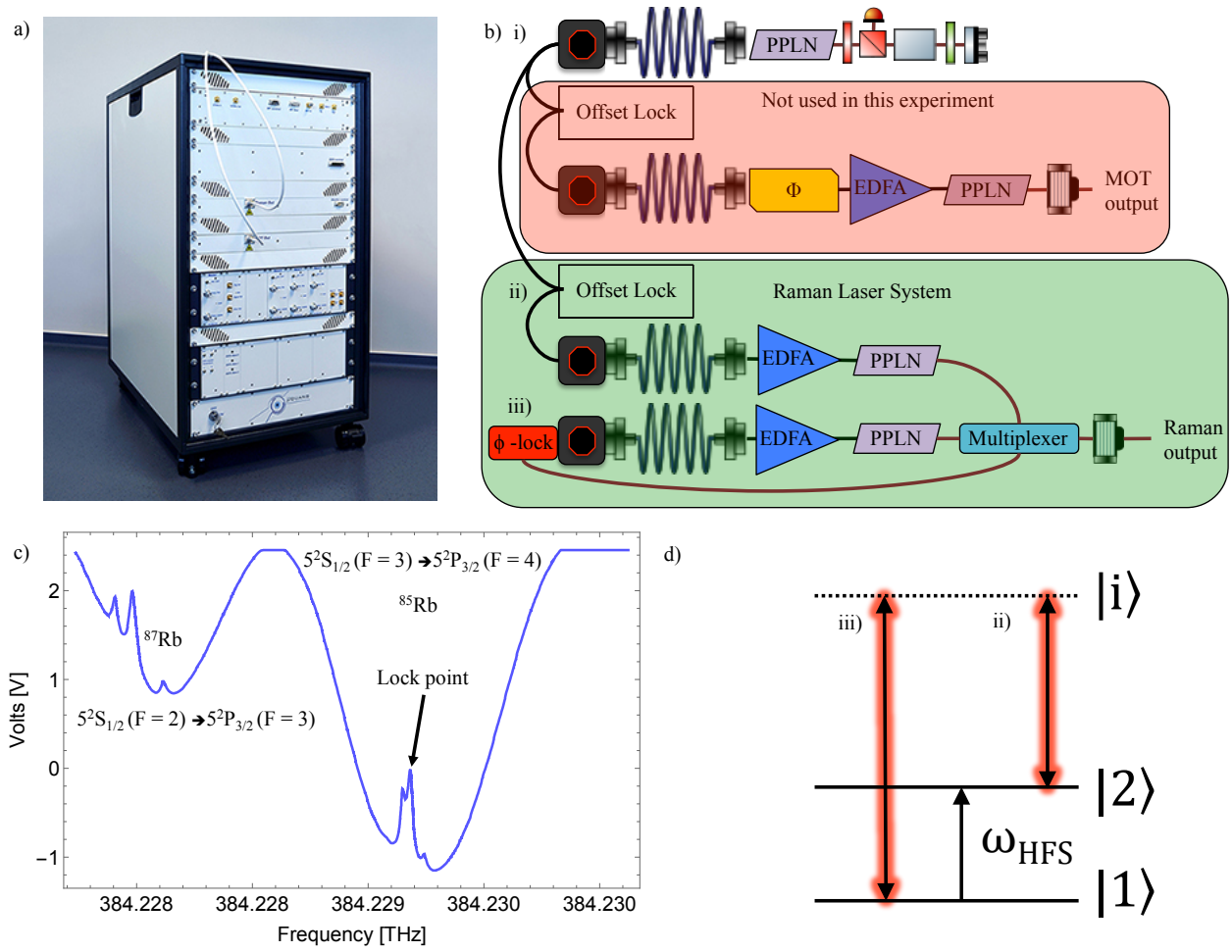

Figure 3.9: Commercial and schematic view of the commercial μQuans UKUS. a) the form factor of the device. b) Schematic of the laser setup inside the device, where i) is the reference laser, ii) is one Raman frequency and iii) the other. c) saturated absorption spectrum from the reference laser. d) Raman laser transitions and their laser label. Note, I only use three of the four lasers, the reference laser and the bottom two lasers, known as the Raman or interferometer lasers, and their attendant frequency and phase locks. I control these lasers through serial communication (for frequency and phase), TTLs and analog voltages (pulses, power and shutters).

the power ratio set by the EDFAs is not maintained across the range of AOM tuning voltages, see a) and b) of Fig. 3.10. To ensure this didn't affect the experiment, I leave the AOM on full RF power for the interferometer sequence, having previously set the intensity ratio. Laser phase noise is also a concern for the interferometer, see c) and d) of Fig. 3.10. C-band fiber amplifiers paired with doubling crystals helps reduce noise by comparison to a tapered amplifier; tapered amplifiers have amplified spontaneous emission over a range of frequencies, a pedestal, that is not suppressed when the amplifier is seeded. This leaves only the RF chain for the phase lock as the culprit for any observed phase noise larger than that listed for the phase frequency

detector. The phase noise, as a power spectral density, for the whole phase lock loop is shown in c) of Fig. 3.10. Pulse times of interest are between 20 μs (50 kHz) and 5 μs (200 kHz). The interferometer samples this power spectrum according to the transfer function [45],

$$|H_\phi(2\pi f)|^2 \approx \begin{cases} 16\sin^4(\omega T/2), \ 2\pi f \ll \Omega \\ 4\frac{\Omega}{(2\pi f)^2}\sin^2(\omega T), \ 2\pi f \gg \Omega, \end{cases} \tag{3.7}$$

where Ω is from equation (2.3). This is shown for a typical interferometer time of $2T = 32$ ms, in d) of Fig. 3.10. The data sheet for the device says, for an interferometer with $2T = 50$ ms and a π-pulse of 20 μs, a three pulse sequence produces 19.75 mrad of phase noise. For the parameters I use in chapter 5, I expect a larger phase noise due to my application of a shorter π-pulse; with $2T = 32$ ms and a π-pulse of 5 μs, a three pulse sequence produces 36.17 mrad of phase noise. The shorter pulse samples the higher frequencies in c) of Fig. 3.10, increasing the laser phase noise. To come to a phase noise, I must integrate the power spectral density convolved with the transfer function up to the frequency of the pulse. While the pulse times I am interested in have larger contributions at high frequency, the transfer function does not weight those frequencies heavily by comparison to contributions below 10 kHz, where the phase lock performs well. This noise is dwarfed by the uncertain from vibrations, shown in section 3.5. This allows me to apply short pulses without worrying that laser phase noise will dominate above vibration noise.

The device is controlled via analog voltages, 5V TTL and RS232 over Ethernet. Analog voltages control an attenuator that feeds the RF amplifier for the internal AOM, allowing for variable output power. TTLs control the pulse length and internal shutter; the device only supports square pulses (there is a low-pass filter on the amplitude control that prevents pulse shaping but also ensures that voltage jitter on the user supplied voltage input does not translate to intensity noise). The RS232 commands, over Ethernet, communicate frequency and phase information to the phase lock and offset lock of the Raman system.

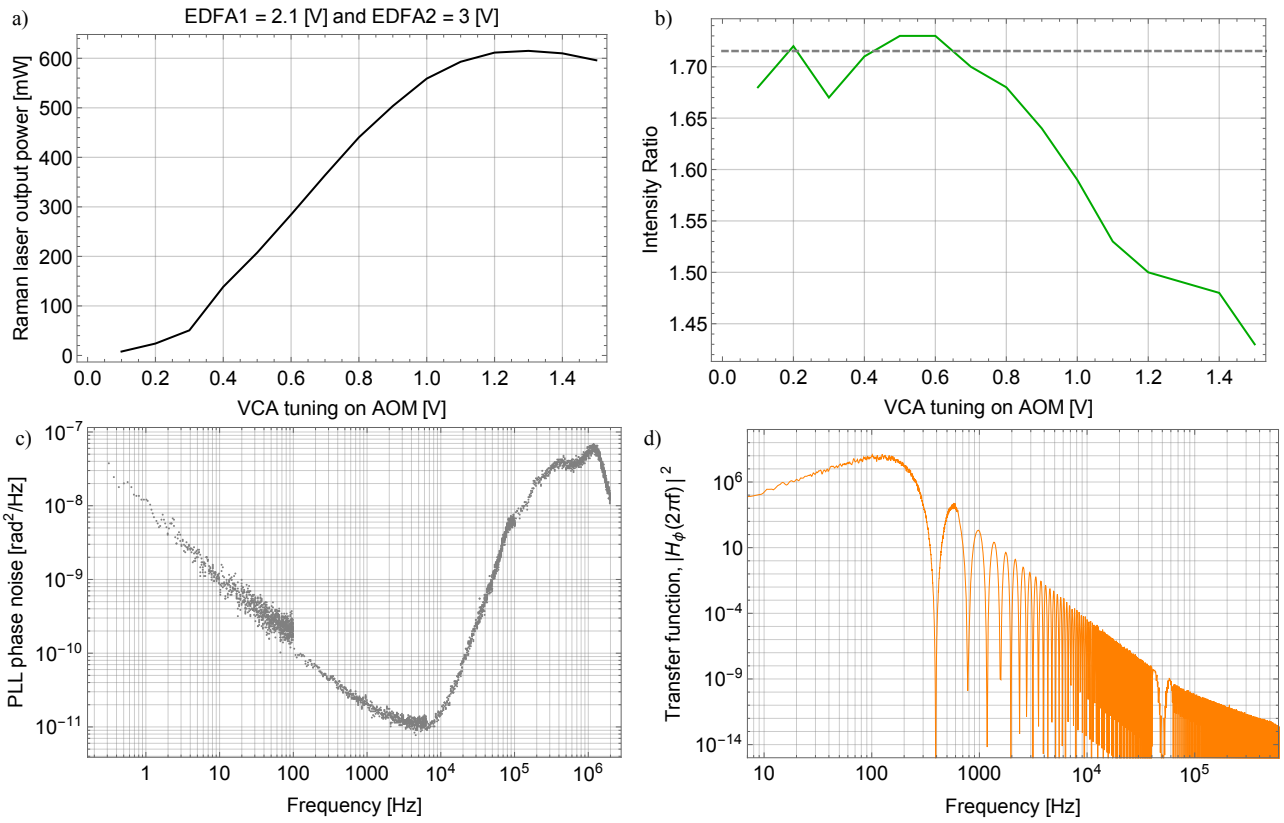

Figure 3.10: Raman laser intensity ratio and phase noise trials. a) AOM RF power as a tuning voltage on a VCA versus output laser power for an EDFA setting that nominally produces an intensity ratio that cancels the light shift. b) Tuning voltage on Raman AOM VCA versus this intensity ratio (I_1/I_2); note, at high powers there is a dip in this power ratio making these settings unusable. c) Frequency versus PLL phase noise. d) Transfer function of the interferometer accounting for the laser phase data in c). The data in c) was provided by the company μQuans and is used with their permission.

3.3 Optics, Imaging and Detection

3.3.1 2D and 3D MOT optics

2D MOT optics

The 2D MOT, i) through vii) in figure 3.1, is a cigar-shaped trap made with elliptical laser beams and two pairs of anti-Helmholtz electromagnets. The beams have an aspect ratio of about 3:1. A beam containing 90 mW of cooling and 10 mW of repump light is first made into a collimated 24 mm $1/e^2$ intensity radius beam from a 780 nm PM fiber. It then passes through polarization optics that split the power between a vertical and horizontal beam. This light is

then passed through two cylindrical lenses, plano-concave and plano-convex, and finally two zero-order quarter-wave plates (the light is right-hand circularly polarized) before entering the glass cell (see v) in figure 3.1). The light is retro-reflected back into the glass cell after passing through another set of quarter-wave plates.

3D MOT optics

I used a six beam configuration for the 3D MOT, see x) in Fig. 3.1. I implemented the AOM and laser frequency recombination such that all six MOT beams are controlled by a single double-pass AOM, see iii) in Fig. 3.5, allowing a smooth transition from 3D MOT to far-detuned molasses cooling. The light is brought into the chamber over four polarization-maintaining fibers; the X and Y beams are coupled into two 50:50 polarization-maintaining fiber splitters (Thorlabs, PMC780-50B-APC), see x) in a) of Fig. 3.1 and the right hand side of a) of 3.5. Each fiber output illuminates a 25 mm diameter, $f = 50$ mm plano-convex lens that creates a collimated $1/e^2$ intensity diameter of 12 mm. Repump light is coupled into all four fibers and comes out over all six beams; the largest intensity of repump light comes out of the vertical axes. The 3D MOT beams produce an intensity of 12 W/m^2 with the 3D MOT AOM at full RF power. Note, the beams denoted Z that are parallel to gravity are the beams that go through the electromagnets. The Z beams are left-hand circularly polarized and the XY beams are right-hand circularly polarized. The power balance is monitored after the 3D MOT beam is separated into horizontal/vertical beams and at the fiber outputs. A horizontal power imbalance of 1 mW between the pairs of counter-propagating beams is enough to ruin the molasses.

3.3.2 Interferometer beam collimator and optics

The Raman axis, the axis sensitive to acceleration, is horizontal. The atomic cloud falls through the beam; this, in combination with the vacuum window size, limits the interferometer time $2T < 50$ ms. The beam collimator (Schäfter+Kirchhoff, 60FC-T-4-M200-37) is AR coated, has

a lens of $f = 200$ mm, and gives a beam waist of $w = 20.9$ mm at 780.nm, see part a) of Fig. 3.11. I tested the device to ensure that I understood the collimator and to check for any defect in the fiber or the collimator; curves x) and y) in the figure are the horizontal and vertical Gaussian intensity profiles of the beam and give a beam waist of $w = 20.9$ mm. I use two apertures on the input side of the chamber to remove the tails of the beam, one just after the beam collimator and another after the steering mirror but before the $\lambda/4$; another aperture is located on the retro-reflection side to ensure all the beam passes through the 25 mm PBS. The first two irises reduce the beam diameter to 22 mm. I use a 50 mm diameter zero-order quarter waveplate to set the input polarization to circularly polarized. After passing in and out of the vacuum chamber through two AR-coated vacuum windows, the beam travels a distance $d = 400$ mm to the aperture in front of an identical zero-order quarter waveplate. This returns the light to linear polarization so I can dump one frequency into a beam stop. This gives me the ability to allow only one set of beams to be resonant. The PBS, with a polarization extinction ratio (PER) of 1:3000, dumps frequency iii) of d) in Fig. 3.9 into a beamstop. The retro-reflection mirror is a $\lambda/20$ flatness, protected silver mirror (Edmunds, 48017) with a navigation grade MEMS accelerometer (Honeywell, QA750) epoxied flat to the back.

3.3.3 CCD camera and optics

I use the free expansion of the atom cloud to measure the temperature of the MOT and molasses; this requires a CCD camera. I opted for a device (Allied Vision, Pike 505B) which works well at 780 nm. Each pixel is 3.45 μm square and the SONY CCD chip is 9.3 mm $\times$ 8.7 mm. The camera is mated with a 2X - 40X variable focus lens system. I fix the pixel to length conversion by taking calibration shots of a ruler placed at the same distance as the camera is to the atoms. A typical snap of a cold cloud, see b) in Fig. 3.11, using our camera software takes 106 ms total. First, a 3 ms exposure is taken of the atom cloud. After a wait time of 100 ms, another 3 ms exposure is taken of the background; this background is subtracted from the image of the atom cloud, producing an image like b) in Fig. 3.11. The CCD camera is not orthogonal to any axis of the 3D MOT. The camera is located 150 mm away from the cloud; It is 13 deg below the

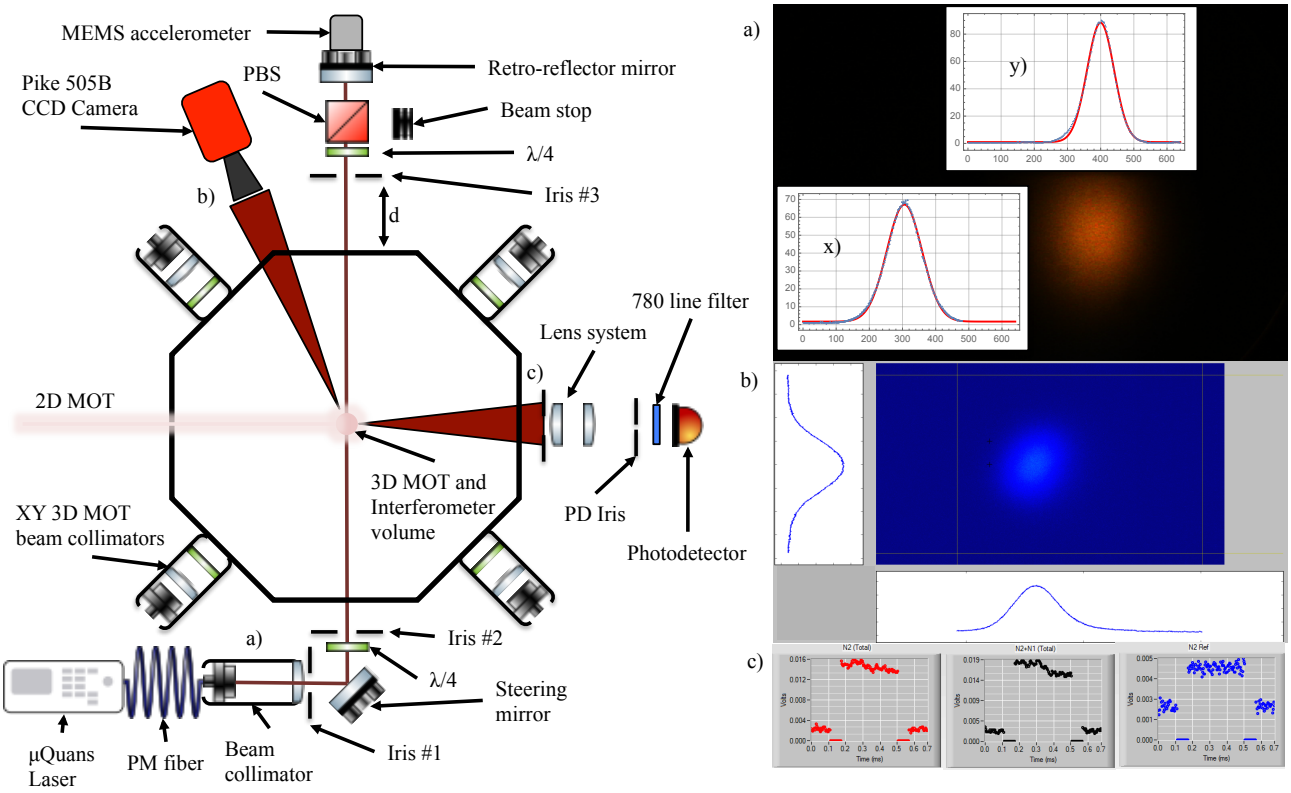

Figure 3.11: Interferometer and detection optics. On the left, labeled interferometer and detection optics discussed in the text: a) A CCD camera snap of the beam produced by the beam collimator. Both x) and y) show the beam is Gaussian with the expected $1/e^2$ intensity diameter of $w = 20.9$ mm. b) CCD camera for imaging the MOT and molasses. This is a snap from the CCD during a molasses time-of-flight trial, showing one snap in a series describing a slowly expanding cloud. c) Photodetector optics for atom number measurements. The early acquisition program in action. The acquisition program shows the voltages measured, see Fig. 3.21 for details.

plane of the XY MOT beams and 22.5 deg off the X MOT axis. Temperature measurements with this CCD camera position samples the temperature of all the 3D MOT axes. I call these axes X and Y, but the Y axis has a greater projection along the MOT electromagnet axis than the X axis.

3.3.4 Photodetector, noise limits and optics

I use a low-noise silicon photodiode with an integrated ultra-low-noise amplifier (Femto, LCA-S-400K-SI) to detect the atom cloud. This device has an active diameter of 3 mm. Fluorescence is collected perpendicular to the Raman axis. First, there is a 50 mm diameter iris to reduce background light from the detection beams, followed by a pair of 50 mm diameter achromatic

doublets with focal lengths $f = 150$ mm and $f = 75$ mm for a magnification of -2. After the lens pair, I placed another iris for fine control of the background light. This is followed by a laser line band pass filter and the photodetector. The photodiode measures through an AR-coated vacuum window with a clear aperture of 32 mm. I collect 1% of the light emitted during fluorescence. The maximum conversion gain around 780 nm is 5.3×10^6 V/W.

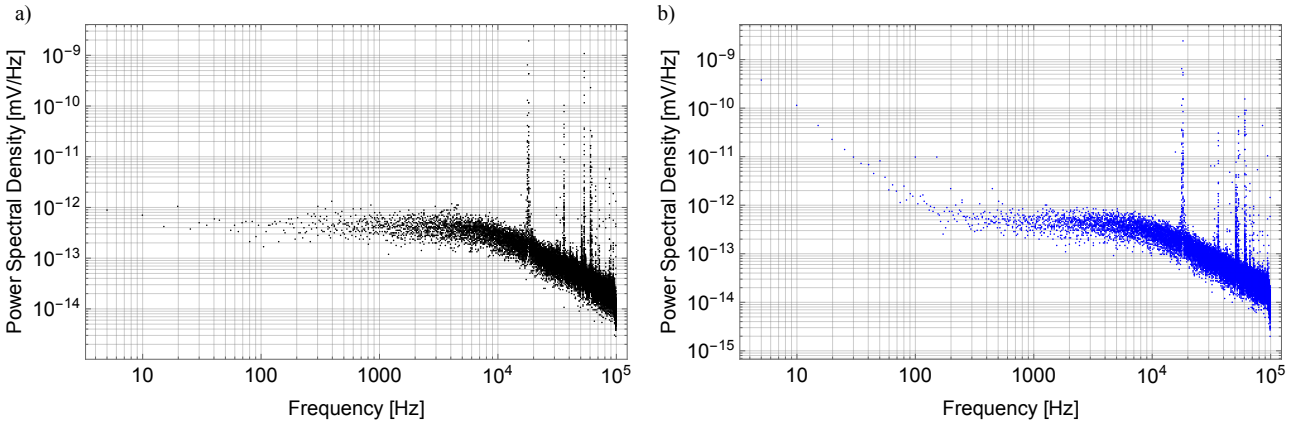

Figure 3.12: Femto photodetector noise figures. a) Power spectrum up to 100 kHz; the only major features are peaks from the op amps in the amplifier, starting around 20 kHz. Note the roll off. This is from an integrator with $\tau = 10.8$ μs, installed before the acquisition card. b) Power spectrum up to 100 kHz with the detection light on and uncontrolled light scatter. Note the increase in noise below 100 Hz.

I performed a series of trials with the photodetector to measure the noise when no light is falling on the photodetector versus when the system measures atoms. I want to see that the noise I measure is consistent with the data sheet. First, I completely cover the photodetector to allow no light to reach it and take a 2 second dataset sampled at 200 kHz; the output noise with no light on the detector is listed as 1.6 $\mathrm{mV_{RMS}}$ over the entire bandwidth. I measured the voltage output, obtaining 1.602 $\mathrm{mV_{RMS}}$, consistent with the data sheet. I am most interested in an equivalent power of light falling on the device so I can compare to atom fluorescence through a solid angle: the measured result comes to 302 pW over 400 kHz. I want to compare to a measurement at 1 kHz; I expect to measure around 15 $\mathrm{pW}/\sqrt{\mathrm{kHz}}$, based on information from the data sheet, and obtain 11 $\mathrm{pW}/\sqrt{\mathrm{kHz}}$, slightly better than expected. The power spectrum of the data, on display as a) in Fig. 3.12, shows no features other than the spikes from the op-amps of the photodiode amplifier.

A measurement with cold atoms, see b) in Fig. 3.12, gave 40 $\mathrm{pW}/\sqrt{\mathrm{kHz}}$, which included noise

from the detection light, background light, and light scatter. Upon further investigation, it was discovered that scattered light into the photodetector was the culprit; it is apparent in the power spectrum as one moves toward DC from 100 Hz. This is primarily from scattered light based on the fact that the background light contributed to 2/3 of the total signal; this led to the use of the second photodiode aperture which gave a 2:1 ratio between signal and background light, see d) in Fig. 3.15, with an SNR of 10.

3.4 The 3D MOT and Sisyphus cooling

Every 3D MOT starts as roughly 20% of the hot rubidium vapor in the 2D MOT cell, see iii) and v) of a) and v) of b) in Fig. 3.1. The 2D MOT is pushed through the 2 mm diameter pinhole, iv) of a) and b) in Fig. 3.1, into the 3D MOT region. Once in the 3D MOT chamber, the slow beam of ^{87}Rb traverses the volume described by the three pairs of overlapping laser beams. Their trajectory takes them near to the center of the chamber and the minimum of magnetic field. A round 3D MOT begins to form, but all is not well; when the magnetic field is switched off, but the MOT light still on, the cloud is flung away from the center of the chamber at considerable speed. After checking for misalignment and power imbalance, I concluded the cloud is not at the minimum of the magnetic field. I needed shim electromagnets to shift the minimum of the magnetic field. Following this, I could then perform temperature and number measurements. Here, I will briefly describe the MOT electromagnet switch and the shim electromagnet drivers, see Fig. 3.13. Following the electronics, I show how I used the shim drivers to shift the center of the magnetic field, leading to the production of cold atoms.

3.4.1 Shim electromagnets and field control

To obtain cold atoms (< 10 μK) of ^{87}Rb, I need the minimum of the magnetic field and the center of the atom cloud to overlap; this minimum magnetic field needs to be $\leq$ 150 mG in magnitude. This kind of fine magnetic field control requires current drivers for the shim

electromagnets; I will also discuss the switch for the MOT electromagnet briefly, see a) of Fig. 3.13.

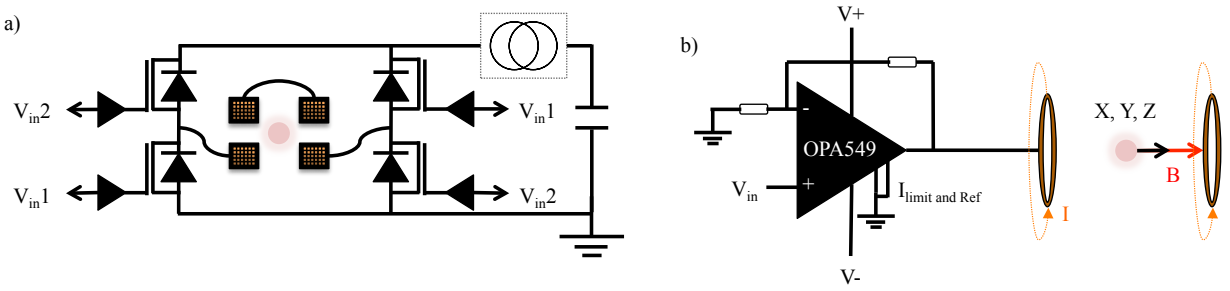

Figure 3.13: Electronics for controlling the magnetic field. a) H-bridge for fast switching of the 3D MOT electromagnet. A single current source (Delta Elektronika, SM 7.5-80) was used to power both electromagnets. b) OPA549 current driver for shim electromagnet operation. Additional electronics allowed for the switching of the current direction and for current limited operation.

A one-chip circuit based on the OPA549 was devised to operate the shim electromagnets with a simple linear voltage control, see b) of Fig. 3.13. I was then able to profile the magnetic field inside the chamber with parameter scan trials. I scanned the X,Y and Z shim electromagnets, one at a time and in that order, fixed the reading that gave the most compact cloud size as imaged by the CCD camera, and reiterated, see Fig. 3.14. I plot *sigma*, the cloud size from the 2D Gaussian fit. This method is placing the center of the quadrupole at the center of the MOT beams using the shim magnets. This left a cloud in the middle of the chamber upon release, after controlling for beam alignment and power imbalance.

I used an H-bridge for the 3D MOT switch, see a) Fig. 3.13, that enables a voltage to be applied across the electromagnets in opposite directions. The idea was to be able to tune the switching time to a minimum. In testing I found that the switch could shut a magnet off in a $1/e^2$ time of 1.5 ms. Installed in the vacuum can and using the atoms as the judge of an appropriate switching time, I found that 3 ms was less lossy and gave a lower temperature.

3.4.2 Temperature and number measurements

I measure the temperature using the time-of-flight technique, where a cloud is dropped and allowed to expand freely for a time T. This expansion is monitored on a CCD camera. I use

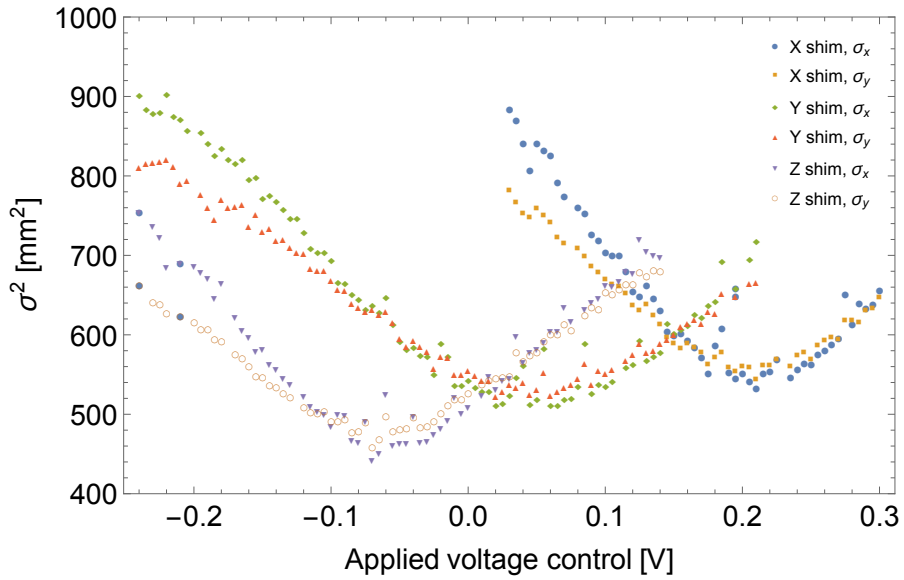

Figure 3.14: Shim field trials. Starting with the X shim electromagnets, I scan the voltage of applied to the driver to realize a small shift in the magnetic field for each shot. I find the minimum for the X shim scan and set the value. I iterate over Y shim and Z shim and repeat all three one more time. Note, as I set the shim values, the next scan leads to a more compact cloud; scan order X, Y, and then Z.

a 2D Gaussian fit to give the size of the cloud, σ, see a) and b) of Fig. 3.15. The method of Fig. 3.14 produces an oval-shaped cloud of atoms, see b) in Fig. 3.11 as well as a) and c) in 3.15. To obtain the temperature, I plot the ballistic expansion time t, squared, against the cloud diameter from the 2D Gaussian fit σ, squared, and fit a line to

$$\sigma^2 = \sigma_0^2 + \frac{k_B T}{m} t^2, \tag{3.8}$$

where σ_0^2 is the initial cloud size, k_B is Boltzmann's constant, T is the temperature, and m is the mass of the ^{87}Rb atom. For the MOT, I obtain a geometric mean temperature of 170 μK. This temperature is not cold enough to perform atom interferometry in our geometry for more than a few ms, so I opt for cooling the atoms further via the Sisyphus mechanism [46], also known as molasses or polarization-gradient cooling. I know the recoil temperature, the theoretical limit of sub-Doppler cooling, is 348.7 nK [43] but that in practice, with Sisyphus cooling, Foot says the best one hope for is about an order of magnitude higher [47].

I release the cloud by switching the 3D MOT electromagnets; this takes 3 ms during which time the MOT light is left on. After this, the detuning of the light is ramped over 500 μs from

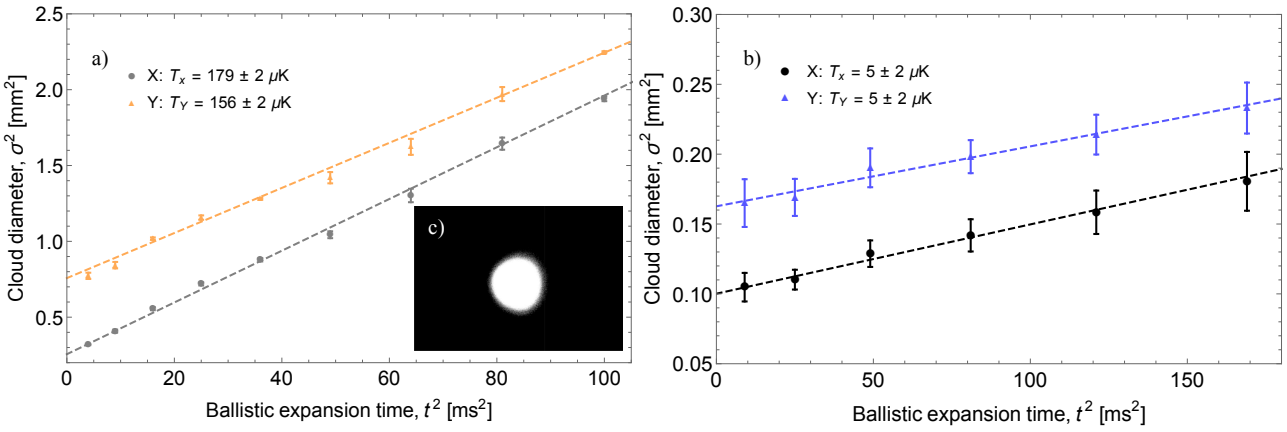

Figure 3.15: TOF temperature measurements for the 3D MOT and Sisyphus cooling. a) The 3D MOT is oval shaped and too hot for atom interferometry for more than a few ms. b) Cold atoms after the conclusion of Sisyphus cooling. c) A 3D MOT forming in the main chamber.

-15 MHz to -150 MHz by the cooling laser offset lock. At the conclusion of the frequency ramp, the intensity is ramped to extinction over 500 μs via the VCA in the RF chain leading to the AOM. These clouds have temperatures consistent with Foot's assertion [47], see b) in Fig. 3.15; I obtain clouds with a geometric mean temperature of 5 μK, cold enough to not disperse while performing interferometry with tens of ms interrogation time.

I measure the particle number in two ways: (i) I use the CCD to estimate the particle number during MOT and Sisyphus cooling trials and (ii) I use the Femto photodetector, see c) in Fig. 3.11, to measure the particle number. The photodetector has a gain from the trans-impedance amplifier of 10^7 V/A and the efficiency at 780 nm is .53 A/W. A single atom, driven on resonance, delivers 2.75 fW incident on the detector; this is smaller than expected from geometry (11 fW per atom) because the solid angle is clipped by changing the limiting aperture from the window to the second iris in front of the photodetector. This is for background removal. For $V = 100$ mV of signal, typical of a number measurement after Sisyphus cooling, I obtain

$$\text{Atom number} = \frac{V}{10^7 \text{ V/A} \times .53 \text{ A/W} \times (2.75 \times 10^{-15}) \text{ W/atom}} \approx 7 \times 10^6 \text{ atoms.} \quad (3.9)$$

3.5 The Honeywell QA-750 MEMS Accelerometer and vibration isolation

Here I discuss the micro-electro-mechanical system (MEMS) navigation-grade accelerometer (Honeywell, QA750). This device is used to track table tilting, vibrations and other accelerations. I perform a series of trials to test the electronics, understand noise sources, and probe the vibration spectrum near the experiment platform, see all of Fig. 3.16. The vacuum can rests on an 310 mm thick, stainless steel optical table (Thorlabs, Nexus series) and four 700 mm tall active vertical and horizontal vibration isolating support legs (Thorlabs, PTS603), see i) of a) in Fig. 3.16. To reach the height of the vacuum windows, the Raman interferometer retro-reflection mirror and the MEMS accelerometer, epoxied flat to the back, must rest on a platform, see ii) in a) of Fig. 3.16. This stand is 240 mm from the table top to the center of the mirror. The outer casing and base are both aluminum. Inside, the stand is filled with sand up to the last 3 cm, where a steel rod protrudes into the stand to lock the top platform in place. The top platform is constructed out of two aluminum plates sandwiching a 5 mm layer of damping foam (α-gel), held tight with nylon screws, see iii) in a) of Fig. 3.16. The mirror and accelerometer are held in a 50 mm diameter mirror mount (Thorlabs, POLARIS-K2F1) epoxied to a ceramic pedestal held firmly via three point contact atop a 1 mm layer of paper, see iv) of a) in Fig. 3.16. The paper and ceramic serve to dampen the transmission of high frequency vibrations from the aluminum stand and table to the retro-reflection mirror, and so the MEMS accelerometer.

3.5.1 Electronics

The MEMS accelerometer is connected to the electronics on the vibration isolation platform through cables that are not stretched taut; this minimizes vibration transfer through the cabling. The Honeywell QA750 MEMS accelerometer used in this experiment outputs a current proportional to the acceleration with a calibration from the manufacturer listing 1.349122×10^{-3} A/g, where g is taken as 9.80665 m s^{-2}. Across this output I connected a 10 kΩ resistor

(measured, 9.9195 ± .0003 kΩ), in parallel with two capacitors in series (measured, each 330 nF). The accelerometer is listed on the datasheet to have bandwidth exceeding 300 Hz, up to 500 Hz; my particular device goes to 430 Hz. I add the capacitors to create a roll off. This creates a time constant $\tau = 1.726$ ms with a 3 dB point at 579 Hz, just past the bandwidth of the accelerometer; this is to suppress any noise not coming from the accelerometer. The ground of the accelerometer case is that of the table top, 2) in a) of Fig. 3.16. This is not the ground of the voltage measurement, 1) in a) of Fig. 3.16.

Understanding the correlation between the sign of the voltage and the direction of the acceleration is the first step in determining whether any force I detect is attractive or repulsive. When the MEMS accelerometer has the non-connectorized side face down on the table (the side epoxied to the back of the retro-reflector), the device delivers a positive voltage, see vi) in b) of Fig. 3.16. The accelerometer is used in the orientation shown in vii) of b) in Fig. 3.16, where the angle θ is exaggerated for display. The table has a slight tilt, and while it does oscillate about some mean tilt angle, it never changes sign.

3.5.2 Vibration isolation

With the accelerometer in the orientation shown in iv) of a) and vii) of b) in Fig. 3.16, I measure the vibration spectrum in m^2s^{-4}/Hz up to 500 Hz under various conditions at midday during a weekday, typical hours for experimental trials, see c) of Fig. 3.16. The flat orange line across the frequency bands is white noise equivalent to 5 nm s^{-2} when integrated over the frequency bands; I present it for reference. The gray spectrum is the pick-up over the electronics and cabling, which appears as a false acceleration of 2.2 μm s^{-2}. Major contributors to this are the frequency band below 1 Hz and the peak at 50 Hz; when powered and part of the power supply ground, the harmonics of 50 Hz are suppressed. With the accelerometer on and the optical table grounded around midday, the accelerometer measures vibrations totaling 1.6 mm s^{-2}. The accelerometer was placed atop the isolation platform and the optical table was floated; this produced the red spectrum, vibrations totaling 712 μm s^{-2}. The atom interferometer geometry provides a filtering effect dependent upon the interferometer time T. For $T = 16$ ms,

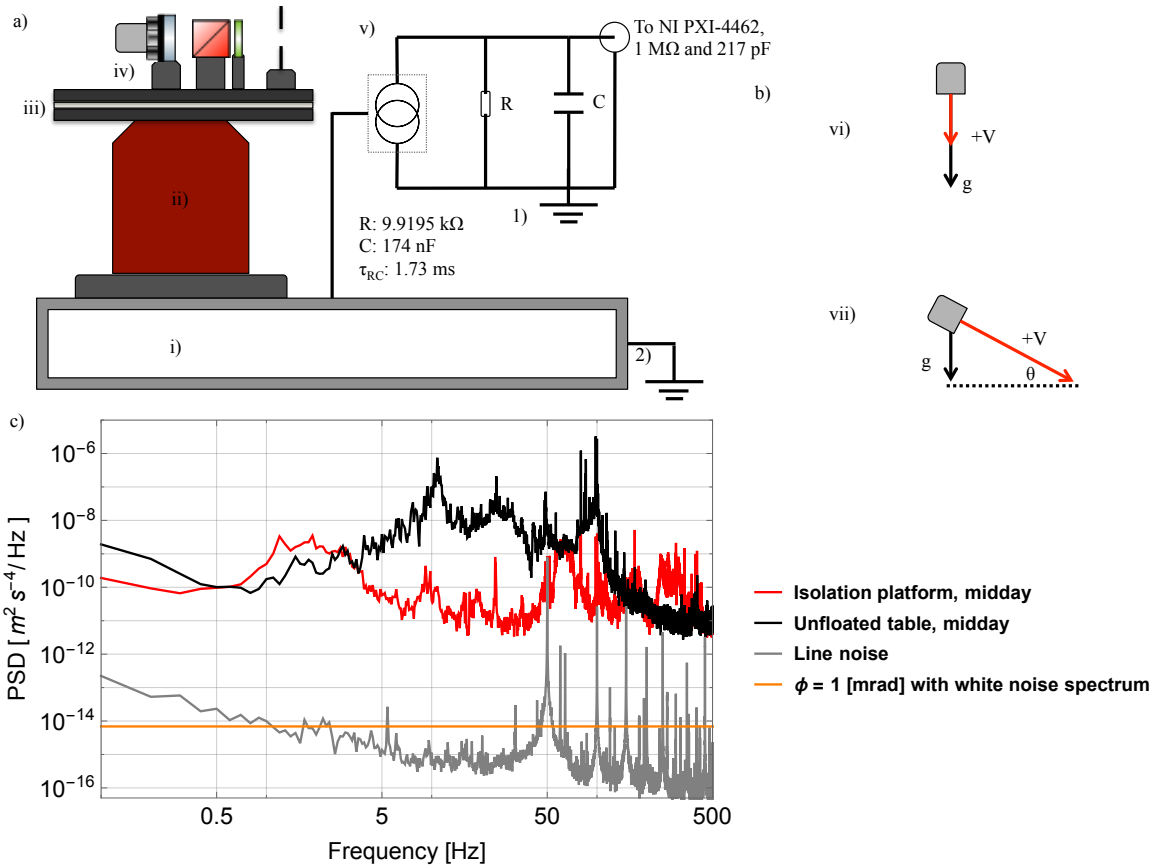

Figure 3.16: QA750 MEMS vibration trials. a) Schematic layout of the MEMS accelerometer and the Raman retro-reflection mirror on the vibration isolation platform. From the floor up: i) Optical table, ii) stand, iii) sandwich of two aluminum plates and a wedge of damping foam, iv) the accelerometer, the mirror and the ceramic pedestal, and v) the circuit diagram of turning the accelerometer current into a voltage. b) Correlation of the sign of the voltage and the direction of acceleration is critical. Determining which way it goes: vi) with gravity and vii) in the orientation (exaggerated) of iv). c) Vibration spectrum over 500 Hz in the setup of a) for various conditions.

this covers a bandwidth of about 63 Hz; the atoms will be sensitive to vibrations totaling 90 μm s^{-2}.

3.6 The source mass

This section describes the source mass installation and geometry. A UHV rotary feed-through is installed in the larger flange containing the MOT window, see i) of a) in Fig. 3.17. This comes with a stepper motor and controller that interface through a Windows computer with a GUI. This rotates a rod inside the vacuum, which extends down into a small ball bearing

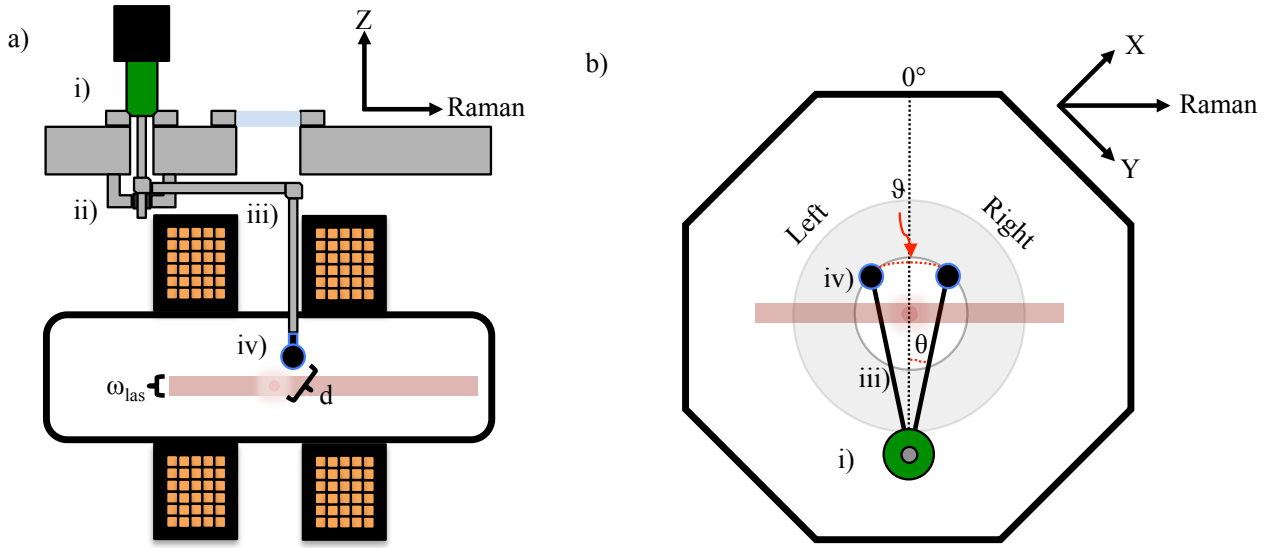

Figure 3.17: Source mass geometry. a) The vacuum feed-through for moving the source mass, side view: i) The UHV compatible rotary feed-through and stepper motor, ii) the ball bearing and stability support, iii) the two rods that bring the source mass into close proximity of the atoms and iv) the source mass, covered in a layer of MH2200 optical coating. b) Vacuum feed-through for moving the source mass, top view: i) the rotary feed-through is positioned just outside the edge of the top 3D MOT electromagnet former. iii) the rod extends into the chamber to allow the source mass access to the interferometer region. iv) The source mass has a range of usable angles, see a) in Fig. 3.19. The orientation convention adopted is the following: when the source mass is past 0 degrees towards +30 degrees, the orientation is referred to as "left" and if the orientation is towards -30 degrees it is "right".

specially lubricated for UHV use, see ii) in a) of Fig. 3.17, held in place by an aluminum brace. An aluminum arm extends out into the chamber, see iii) of a) and b) of Fig. 3.17, where it is attached to an aluminum rod holding the source mass. The source mass, a sphere of aluminum of radius 19 mm, see iv) of a) and b) in Fig. 3.17, sits above the plane of the XY MOT beams and the Raman beam. It is covered in a coat of Alion MH2200 optical absorber coating. This is a black coating that has a high absorption in infrared with very low out-gassing, $< 10^{-12}$ (mbar liter)/(s cm^2), comparable to stainless steel.

The Raman beam is reduced to 22 mm diameter beam using two irises. The nearest approach of the source mass to the axis of the Raman beam is at d = 25 mm, see a) in Fig. 3.18, placing the source mass in the shadow of the aperture. The Cartesian coordinates of the ball are determined by

$$d = \{x, y, z\} = \{R\cos(\theta) - x_0,\ y_0,\ R\sin(\theta)\}, \tag{3.10}$$

where I set the origin of Cartesian coordinates to be the center of the cloud, $\{x, y, z\} = \{0, 0, 0\}$. I need to know the positioning of the source mass relative to the atoms. The vertical axis of rotation and a vertical axis through the center of the ball are separated by $R = 72.79$ mm, the extension rod iii) in b) of Fig. 3.17. The vertical axis of rotation and a vertical axis through center of the cloud are separated by $x_0 = 55.00$ mm. The vertical separation, y_0, between the horizontal plane through the center of the ball and the horizontal plane through the center of the atom cloud is 12.7(2) mm. The XY plane is horizontal. The Raman axis is ±45 degrees off the Y and X axes, also the MOT axes, respectively. The Z axis is parallel with gravity. The axis of rotation and the vertical through the center of the cloud both lie on the X axis, separated by x_0. Using equation (3.10), I can calculate the distance d of the center of the atom cloud to the center of the source mass as a function of angle, see Fig. 3.18. The full angle available to move the source mass is $\vartheta = 50$ degrees, shown in b) of Fig. 3.18.

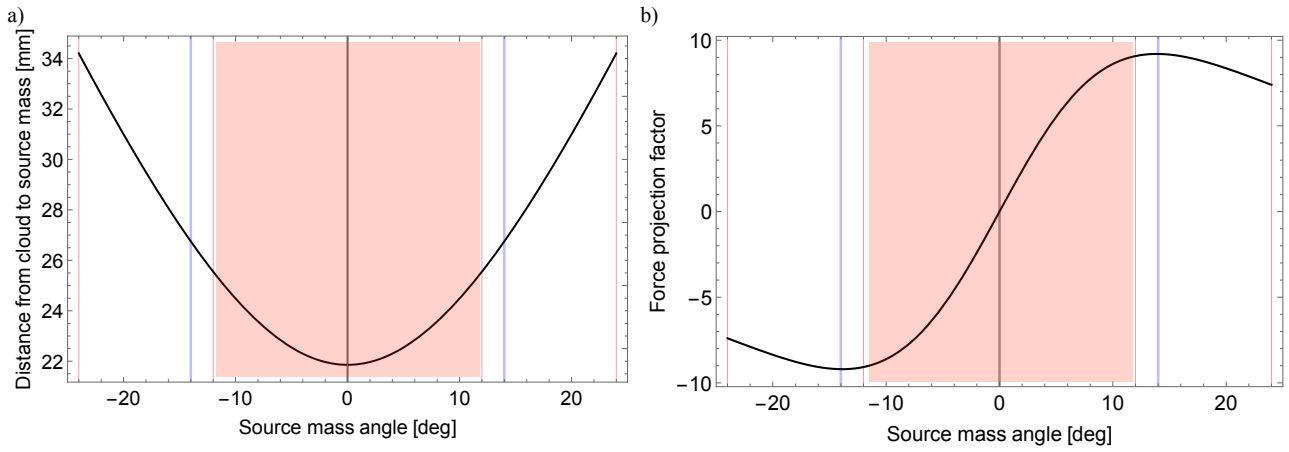

Figure 3.18: Source mass angles and the force projection factor.

Barriers to further movement of the source mass, see thin red lines in Fig. 3.18, prevent the source mass from hitting the electromagnet former. These barriers are designed into the ball bearing mount, see ii) in a) of Fig. 3.17. The red region around 0 degrees, while accessible to the source mass, blocks the top 3D MOT beam. Further, from -5 to 5 degrees, the source mass clips the solid angle of the photodetector, making this region of space thoroughly unusable. The thin blue lines at ±14 degrees are the angles used in the experiment.

Based on geometry I can define a force projection factor, scaled to one, as a function of the angle the source mass has with respect to the atomic cloud, see b) in Fig. 3.18. This factor

helped in the design of the experiment and can help inform the design of future experiments. This factor uses geometry to parameterize how sensitive the atoms are to a $1/r^2$-style force,

$$F \sim \frac{1}{d^2}; \tag{3.11}$$

the projection onto the Raman axis is

$$F_z = \frac{1}{d^2}\frac{z}{|d|} = \frac{z}{\sqrt[3]{x^2+y^2+z^2}}, \tag{3.12}$$

This force projection, scaled to numbers of order 1, is plotted as a function of the source mass angle θ, see Fig. 3.18, in angles read from the stepper motor assembly. The thin red thin lines and shaded areas are restricted regions. The blue lines for ± 14 degrees are shown to be near the maximum extent of the force projection factor's range, around a projection factor of ± 9.2; these are the positions I used for the source mass to create the largest possible $1/r^2$-style force. In the theoretical work supporting this experiment, the atom ensemble was considered at the surface of the source mass [3]; the acceleration calculated was the acceleration along the line joining the center of the source mass and that of the atom cloud. This force needs modification by the factors above: (i) the separation is larger than the radius of the mass, so a reduction factor of $(\frac{r_{\text{ball}}}{d})^2$ is required, where $r_{\text{ball}} = 19$ mm and d is the distance from the atom cloud to the source mass center, as shown in a) of Fig. 3.17. (ii) The interferometer only measures the component along the Raman axis. To account for this, I require a reduction factor of $\cos(\theta)$. The total force reduction factor has a value ± 0.332. A point of improvement to future experiments would be to enhance the factor or improve the experiment in other ways to counteract this.

3.6.1 Light scatter tests

In this experiment, I am concerned with three light scatter problems: (i) First, I want to ensure that no leakage light from the 3D MOT setup makes its way into the chamber. (ii) Second, I want to ensure that the source mass does not scatter Raman light through the interferometer

volume. (iii) And finally, I want to control the background light during detection. In this section, I address (i) and (ii). I leave (iii) for discussion about the primary experiment in Chapter 5.

A few μW of resonant or near resonant leakage light from the 3D MOT beams can provide enough photons to optically pump the atoms, creating a false signal. The cooling light going into the 6 3D MOT beams is controlled by a single double-pass AOM; when the RF switch is triggered and the VCA tuned to allow no RF power through, all light through the AOM shines on a beam block. Only a few μW travel down the beam line leading to the 6 fiber couples, see iii) in a) of Fig. 3.5, from the cooing laser and is 220 MHz red-detuned; it is not coupled into the fibers and can not be measured at the output of any fibers. The repump laser is controlled by a single pass AOM located two fiber couples before the experiment, see Fig. 3.4; triggering the RF switch and tuning the VCA on the repump AOM passes no light into the first fiber couple. No light passes in the next stage, and none onto the experiment. After these checks were complete, a cold cloud could be dropped for $>$ 40 ms undisturbed; the distribution of atoms in the F=2 ground state, after Sisyphus cooling, remained unaltered for this time.

Scattered Raman light can be parameterized by an electric field ϵ. This field could cross scatter back through the main Raman beam axis, denoted by a field E; at worst, this could change the phase by $\delta\phi = \epsilon/E$, leading to the measurement of a false acceleration. I want to keep this false acceleration below the 10 nm s^{-2} level. To do this, I need to control this phase shift to $\delta\phi = \epsilon/E \leq 4 \times 10^{-5}$. It is critical that this light scatter be kept to a minimum; when the source mass is moved, I want to ensure the light scatter through the atom cloud is less than 2×10^{-9} of the peak Raman intensity. To do this I performed light scatter trials on a 1:2 scale system.

By geometry, I have eliminated the possibility of blocking the Raman beam with the source mass. By clipping the beam with an iris, the Gaussian tail is prevented from diffracting around the edge of the window and the source mass. Despite this, light is still diffracted into angles that will land on the source mass. To test this, a scale model was created, see a) of Fig. 3.19. A 780 nm test laser (Thorlabs, S1FC780) was coupled to a fiber collimator (Schäfter+Kirchhoff,

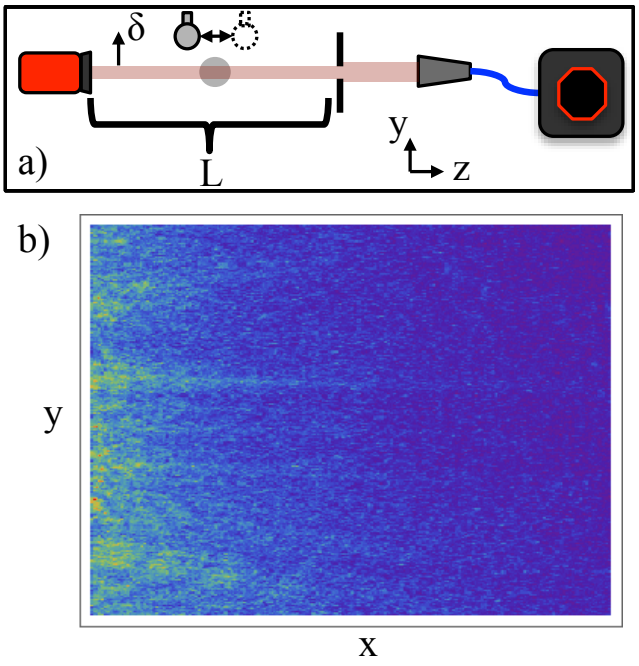

Figure 3.19: Light scatter near the source mass. a) The scale test setup. I used a low power 780 nm fiber laser and a beam collimator as a test Raman beam. I passed this beam through an iris and used a CCD camera to examine the diffraction around the edge of iris, paying particular attention to the region occupied by the source mass. b) Long exposure (.5 s) snapshot of the scatter past the iris edge.

60FC-Q780-4-M100-37), passed through an iris and onto a CCD camera (Allied Vision, Merlin F-033C) at various positions along the light beam path, including through optics detailed in iv) of a) in Fig. 3.16. The CCD camera used no optics and was modified to prevent scatter around the CCD chip and electronics for this measurement; reflective surfaces were covered with black vinyl tape and coated metal foil. A 1:2 scale source mass of polished steel was used. This setup was constructed in a box shielded from background light. I applied low powers (150 μW), producing images like b) of 3.19 for an exposure time of .5 s, where the CCD camera was scanned across the iris edge and into the shadow created by the iris. The beam waist was 10.5 mm. This shows scattered photon count across the CCD chip, where the chip is set downstream, behind the source mass by a distance L parallel to the aperture edge. In a typical π-pulse, 1.5×10^5 photons scatter off the source mass. To put a bound on the phase shift from scattered light, I take the worst case scenario in which all the light scattered from the ball goes through a solid angle subtending the entire interferometer volume and that these photons are as effective as driving transitions as the photons that are not scattered. This gives a power ratio

of the peak beam intensity versus the worst case scatter through the interferometer region as $\epsilon/E \rightarrow 8 \times 10^{-10}$; this is a factor 2 below the required intensity to create a systematic of order 10 nm s^{-2}, as the worst case scenario. Regardless, I took caution before installation; the source mass, of machined aluminum, was coated in a layer of the NIR absorbing, UHV-compatible paint MH2200.

3.7 Computer control system, sequencing and pattern generation

In the following subsections I describe the hardware that enabled this experiment to function and the work that went in to ensuring precise timing. I then describe the pattern generation and acquisition software.

PXI case and cards

National Instruments PXI instrumentation is used in this experiment. A small chassis (NI, PXI-1072) contained three output cards and one input card. First, the PXI-6723 (13-Bit, 32-Channel, 800 kS/s) provides analog outputs to the experiment. Next, the PXI-6541 (50 MHz, 32-Channel) high-speed digital card controls digital communication to the MOT laser system and AOMs. Last, the PXIe-6341 (16 AI (16-Bit, 500 kS/s), 2 AO, 24 DIO) controls digital communication to the Raman laser system. The PXI-4462 (204.8 kS/s, 4-Input) is used to log the MEMS and photodetector voltages.

Variable time based functionality through an FPGA

The timing sequence for the experiment involves slow processes like loading the MOT and fast processes like the Raman pulses. I opt to use a variable frequency clock, where clock pulses are generated dynamically, changing when the card outputs need to change timebase. I use the Opal

Kelly XEM3001 FPGA module (400,000-gate Xilinx Spartan-3 FPGA, XC3S400-4PQ208C) for this purpose.

In brief, a hardware server sends the FPGA a list of variable timebase segments to be used in a run. The segments specify the clock frequency and the number of clock pulses needed for the segment. The FPGA generates the clock frequency from dividing down the master clock (300 MHz).

Cicero and Atticus - pattern generation and timing

I make use of Cicero Word Generator and Atticus Hardware Server software [48] for pattern generation and hardware communication. Cicero, designed to use National Instruments output hardware, is compatible with any output hardware that uses the NIDaqMx driver library. The hardware layer consumes substantial memory for generation of the output buffers; a large amount of memory located on the computer communicating with the output cards is critical to ensure smooth running. The user interface allows for separating an experiment into individual time blocks, with individual timing, supporting analog output, digital output, GPIB and RS232 communication. See an experimental run on Cicero in Fig. 3.22. I show a schematic version of the run pattern shown in Fig. 3.22 in Fig. 3.20.

Labview CVI

The acquisition software was designed in Labview CVI. The program acquires two voltages, the voltage from the MEMS accelerometer and the voltage from the photodetector. For all experiments presented, the detection is clocked at 200 kHz and triggered by the FPGA. I briefly describe how these signals are acquired below.

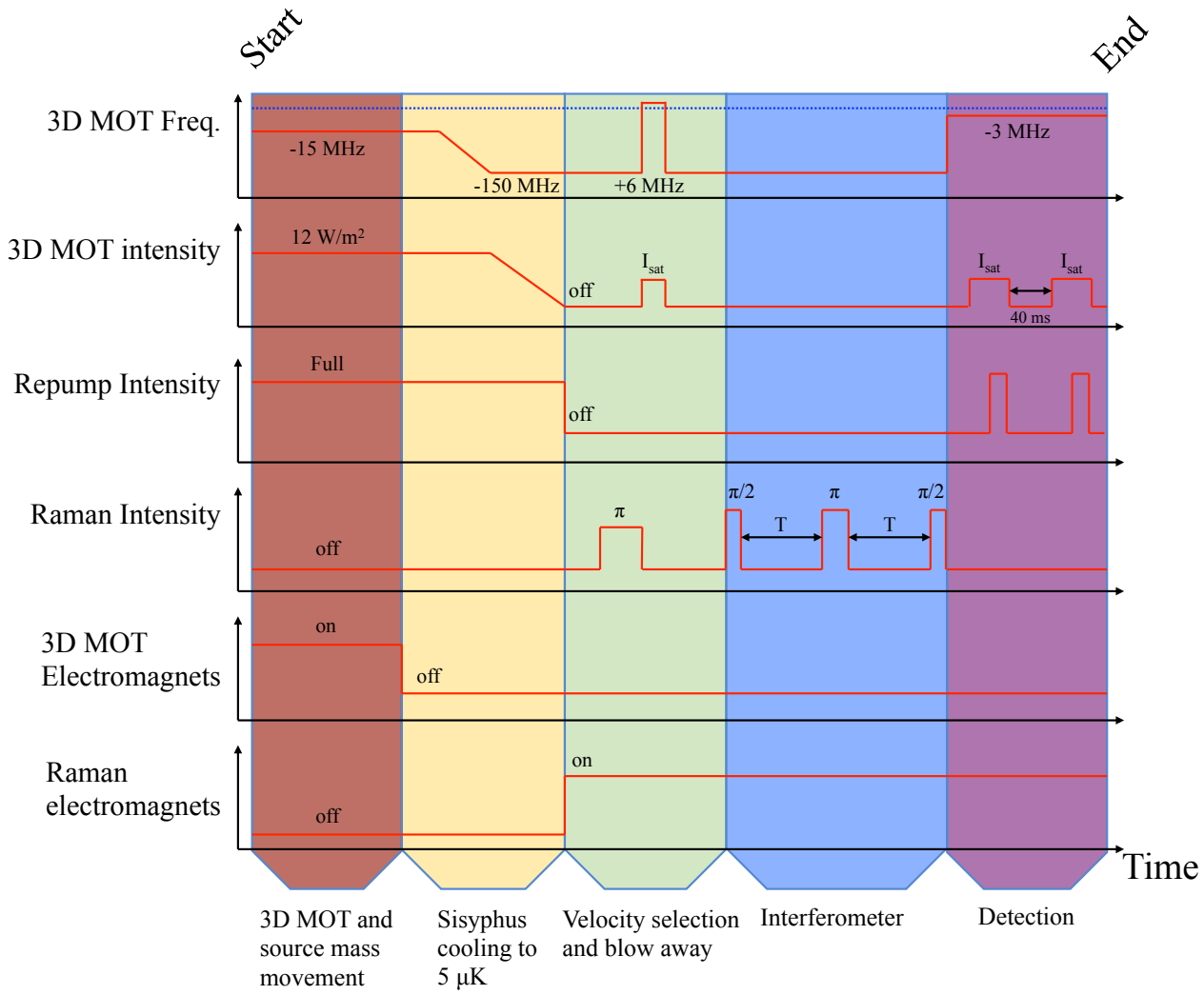

Figure 3.20: Schematic experiment run pattern. Here I display the most dynamic channels: the 3D MOT frequency (controlled by the VCO in the offset lock of the cooling laser) and intensity (tuning applied RF power to the 3D MOT AOM), the repump intensity (tuning applied RF power to the AOM), the Raman light intensity (tuning applied RF power to the AOM in the μQuans laser), and the electromagnet switches for the 3D MOT and Raman axis electromagnets. I discuss velocity selection and blow away sequencing in sections 4.1.2 and 4.2.1.

MEMS voltage

The MEMS voltage acquired by the NI PXI-4462 card is positive. In a typical experiment, the voltage is acquired every 5 μs over the interferometer time 2T. The mean of this is given as an output. The triangularly weighted mean is another output . Here, the weighting increases linearly to 1, starting at 0 over the interval $0 < t < T$, the decreases to 0 over $T < t < 2T$ [49].

Photodetector voltage

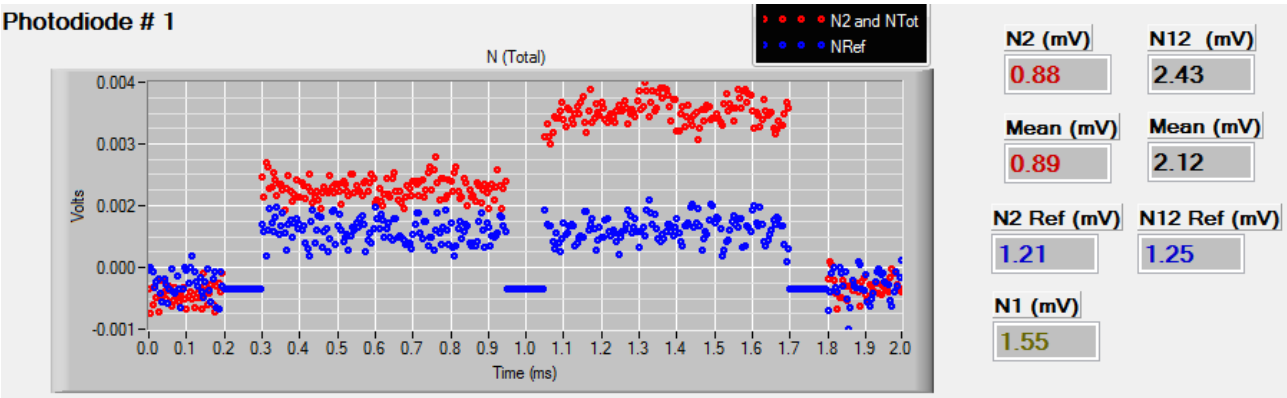

Figure 3.21: Detection scheme. A snapshot of the photodetector acquisition taking place during a typical interferometer run. The atomic signal is in red and the background light is in blue. See Fig. 3.20 for the detection sequence in the pattern.

The photodetector voltage, also acquired by the NI PXI-4462 card, is a positive voltage, see Fig. 3.21. The detection sequence is broken into two sections, atomic signal acquisition (red) and background determination (blue). The background, superimposed on the atomic signal acquisition for comparison, occurs 40 ms after the interferometer output is measured. The background determination uses the same detection sequence as the atomic signal acquisition, the only difference being that I have waiting until all the atoms have left the measurement volume. The sequences are identical and obtain voltage values corresponding to N_2, N_{tot}, $N_{2,\text{bg}}$ and $N_{\text{tot,bg}}$, the atom number in $|2,0\rangle$, the total number of atoms in $|2,0\rangle$ and $|1,0\rangle$, the background light of the $|2,0\rangle$ atom number measurement and the background of the total atom number measurement, respectively. First, the cooling light is turned on for 750 μs, measuring N_2. Next, the repump is turned on for a 750 μs measurement of N_{tot}. I make small cuts to remove the rise time and fall time associated with changing the light intensity. I can then take these voltages

and produce a mean value which can be used to construct the probability

$$\mathcal{P} = \frac{N_2 - N_{2,\mathrm{bg}}}{N_{\mathrm{tot}} - N_{\mathrm{tot,bg}}}. \tag{3.13}$$

These four mean voltages are exported, as well as the probability $\mathcal{P}$.

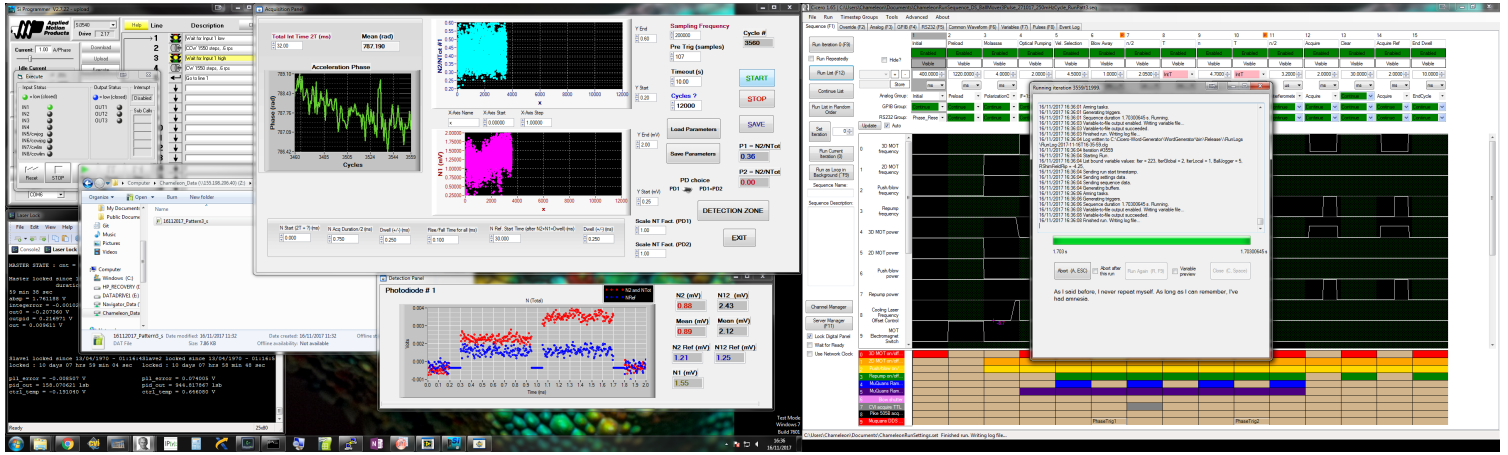

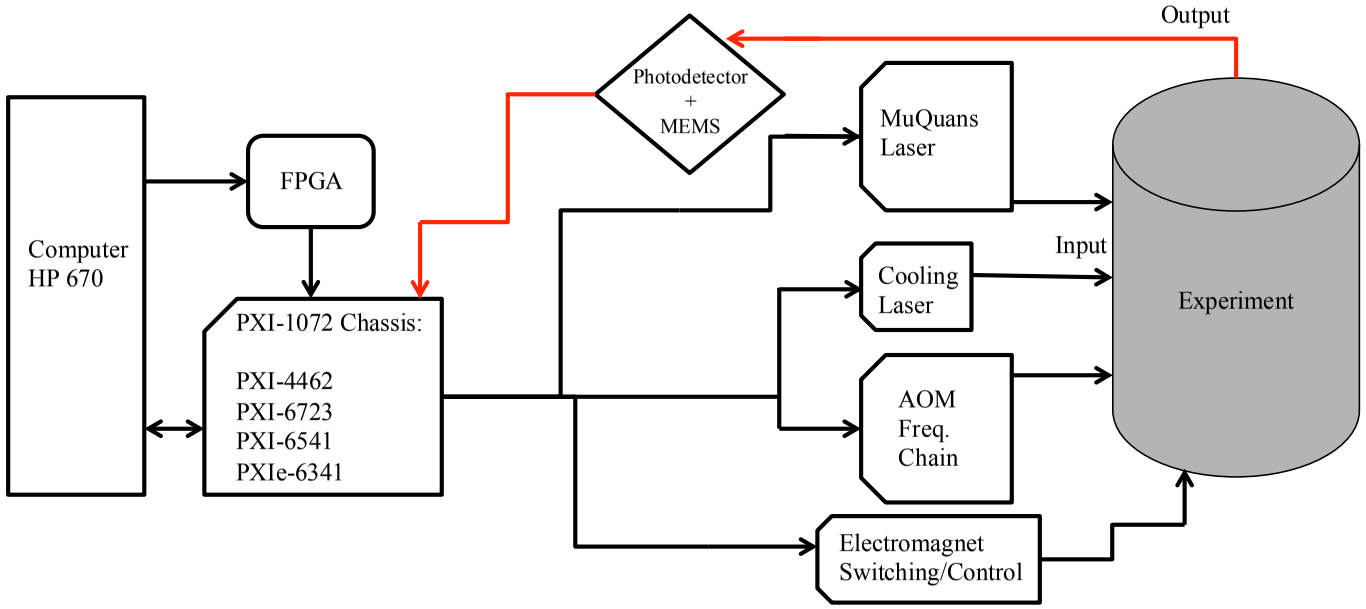

Figure 3.22: Experiment control and block diagram. Top: The experiment control computer doing work on 16 Nov, 2017 with a range of software in view. From left to right, the stepper motor control GUI and the Raman laser lock monitor. Behind these windows are terminals monitoring the hardware server and commands sent to it. Moving right, the Labview CVI acquisition program is busy taking data. Below it is a recent photodetector acquisition. Further right is Cicero, having just successfully output the next pattern. Bottom: Block diagram of the experiment. Starting with a Windows machine, the pattern generator sends clock information to the FPGA and the pattern to the PXI chassis. The FPGA then starts the sequence, sending a dynamic clock signal to all the cards. These cards output to various systems; the MOT lasers, AOMs, electromagnets, and the Raman laser. A short time later, output from the photodetector and MEMS is acquired and sent to the computer.

Chapter 4

Setting up the interferometer

With the apparatus on the table, my goal turned to setting up the interferometer. First, using a co-propagating beam configuration, see a) in Fig. 4.1, I checked that I understood the Rabi frequency, the separation of magnetic sub-levels and the light shift. Following this, I began Ramsey interferometry to check the quality of my state selection and the timing between pulses. I add in a third pulse to realize spin echo experiments. These tests were useful in that they allowed me to use a simpler system to check my understanding without the additional concern of vibrations or the initial velocity distribution of the atoms.

In the section following, I retro-reflect the Raman beam to begin counter-propagating studies. I make a velocity selection from the cold cloud and perform 3 pulse, acceleration-sensitive interferometry using configuration b) in Fig. 4.1. The method pursued has both pairs of light beams resonant, driving two atom interferometers simultaneously. I use these data to check the accuracy of my laser phase commands. Using this method of two simultaneous interferometers does not produce high fringe contrast in my experiment. I resolve to move on to configuration c) in Fig. 4.1. I realize Kasevich-Chu style atom interferometry and focus the rest of the section on investigating the correlation with the MEMS accelerometer, concluding with a calibration of the MEMS accelerometer to the atom interferometer. All data presented are representative, single scans. If averaging is used, it is explicitly mentioned.

Co-propagating versus counter-propagating and conventions

In the two sections below, I use three optical geometries on the way to acceleration-sensitive atom interferometry, see Fig. 4.1. In the first section, I use co-propagating Raman light with the two frequencies in perpendicular Linear polarizations, see a) in Fig. 4.1. I block the retro-reflection for tests in this configuration. After discussing Raman spectroscopy, I confirm that changing the incoming polarization from perpendicular linear to circularly polarized no longer drives the Raman transition, in agreement with the selection rules discussed in chapter 2.

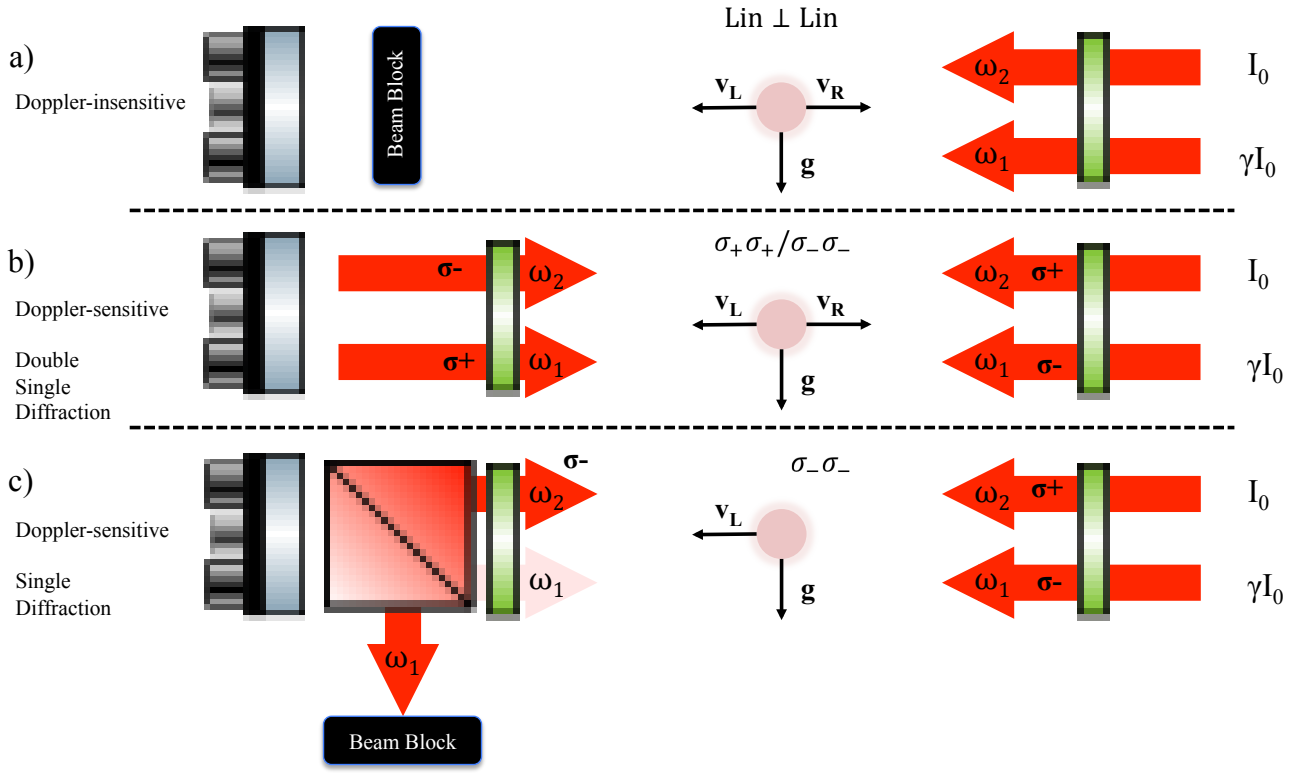

Figure 4.1: Co- and counter- propagating geometry. a) Co-propagating method: this configuration is important as it allows for testing without the addition of acceleration noise. b) First counter-propagating method: both $\sigma_+\sigma_+$ and $\sigma_-\sigma_-$ transitions are allowed which can open two interferometers simultaneously. c) Second counter-propagating method: I dump a single frequency before the retro-reflector using polarization optics. This allows me to choose $\sigma_+\sigma_+$ or $\sigma_-\sigma_-$. This is the setup for the primary experiment, where I have selected $\sigma_-\sigma_-$ transitions. The factor γ=.583 for the detuning I have chosen.

In the section following, I start studies using counter-propagating beams using b) of Fig. 4.1; with the incoming beam circularly polarized, I retro-reflect the beam through a $\lambda/4$-plate, which flops the polarizations of the frequencies. This allows me to drive $\sigma_+\sigma_+$ and $\sigma_-\sigma_-$ transitions as well as conferring velocity sensitivity. I make an acceleration-sensitive atom interferometer

in this setting and show that utilizing two simultaneous interferometers does not confer the best acceleration sensitivity in my experiment. Finally, I add a polarizing beam-splitter after the second $\lambda/4$-plate, see c) in Fig. 4.1, which allows me to select one frequency and extinguish it. By this method, I can drive $\sigma_+\sigma_+$ or $\sigma_-\sigma_-$ transitions. I choose to drive $\sigma_-\sigma_-$ transitions and proceed to investigate correlations with my MEMS accelerometer.

4.1 Studies with Co-propagating Raman beams

4.1.1 Rabi flops and Raman Spectroscopy

At the end of Sisyphus cooling, the cold atom cloud is left distributed across the 8 Zeeman sub-levels of the F=1 and F=2 ground states. The quality of the cooling and repump AOM extinction and the inhomogeneity in the applied magnetic field determine the exact distribution of atoms across these states. I begin the studies of co-propagating transitions by performing a simple manifold selection; I load all the atoms into the Zeeman sub-levels of the F=1 ground state. I do this by turning off the repump light for the last 2 ms of the Sisyphus cooling. To begin driving the Raman transition from F=1 to F=2, parameters had to be given to the μQuans laser; the detuning, power ratio, and overall output power. In accordance with the magic ratio calculation in chapter 2, the offset lock of the two lasers was set to a detuning -1.13 GHz from the cycling transition, $5^2S_{1/2}(F = 2) \rightarrow 5^2P_{3/2}(F = 3)$. To cancel the AC Stark shift, this detuning requires an intensity ratio of .583 between ii) and iii) of b) and d) in Fig. 3.9. This was done by setting a fixed RF power for AOM at the output ii) and iii) in b) of Fig. 3.9 and varying the power ratios of EDFA 1 and EDFA 2. I found that scanning the RF power applied to the AOM, for fixed EDFA ratios, did not maintain the intensity ratio, see a) and b) of Fig. 3.10. To ensure I used a stable intensity ratio, I would choose a fixed RF power for the AOM and change the amplifier settings. For my first test to drive the $|1, 0\rangle \rightarrow |2, 0\rangle$ transition, I selected an output power corresponding to a π-pulse time of 23.4 μs or a Rabi frequency of 20.4 kHz. A small magnetic field was applied to lift the degeneracy of the Zeeman sub-levels. The frequency of the phase lock between Raman laser 1 and 2 was scanned around 6.834 GHz,

the hyperfine splitting, and I monitored the transition probability $\mathcal{P}$ of atoms being in the F=2 manifold at these frequencies. In this chapter, all frequencies are referenced to the hyperfine splitting (HFS) and are denoted by the shorthand "Difference Frequency from HFS." I applied a square pulse of 23 μs and scanned the 200 kHz around the hyperfine splitting, see Fig. 4.2. I expected to observe a sinc function with a maximum probability near to .33 of the atoms present, with the assumption that I had filled all three Zeeman sub-levels equally. I fit a sinc function to the data in Fig. 4.2, the red line, [7]:

$$\mathcal{P} = \frac{1}{3}\frac{\Omega^2}{\left(\Omega^2 + (2\pi\delta f)^2\right)} \sin^2\left[\frac{\tau}{2}\sqrt{\Omega^2 + (2\pi\delta f)^2}\right], \tag{4.1}$$

where $\mathcal{P}$ is the transition probability, Ω is the Rabi frequency, δf is the difference frequency from the hyperfine splitting and τ is the pulse time. The fit tells me I applied a square pulse in time of $23.2 \pm .3$ μs and that the center of the peak is -2 kHz off the hyperfine frequency. The peak of the sinc went to $\mathcal{P} = .32$ of the total population present. This implies my assumption that the states are loaded equally may be correct, but I press on to confirm my suspicions that the rest of the atoms are distributed amongst the two magnetically sensitive states, $|1,1\rangle$ and $|1,-1\rangle$. Immediately following this, I looked for Rabi oscillations where I scan the pulse time, see inset in Fig. 4.2, confirming the π-time was indeed 23 μs.

An investigation of the entire F=1 manifold is warranted to study the distribution of the atoms across internal states, polarization quality of the light and control of the magnetic field. A small magnetic field induces a shift between the three Zeeman sub-levels of F=1. Scanning the frequency difference between the Raman lasers, I expect the Lin$\perp$Lin polarization to drive the transitions to $|1,1\rangle \rightarrow |2,1\rangle$ and $|1,-1\rangle \rightarrow |2,-1\rangle$. A scan of 2 MHz around the $m_F = 0$ transition reveals the transitions, see a) in Fig. 4.3.

The $m_F = \pm 1$ peaks are approximately equidistant $\delta f \approx \pm 670$ from the $m_F = 0$ transition. The Breit-Rabi formula is

$$E_{|J=1/2 m_j I m_I\rangle} = -\frac{\Delta E_{HFS}}{2(2I+1)} + g_I \mu_B m B \pm \frac{\Delta E_{\mathrm{HFS}}}{2}\left(1 + \frac{4mx}{2I+1} + x^2\right)^{1/2}, \tag{4.2}$$

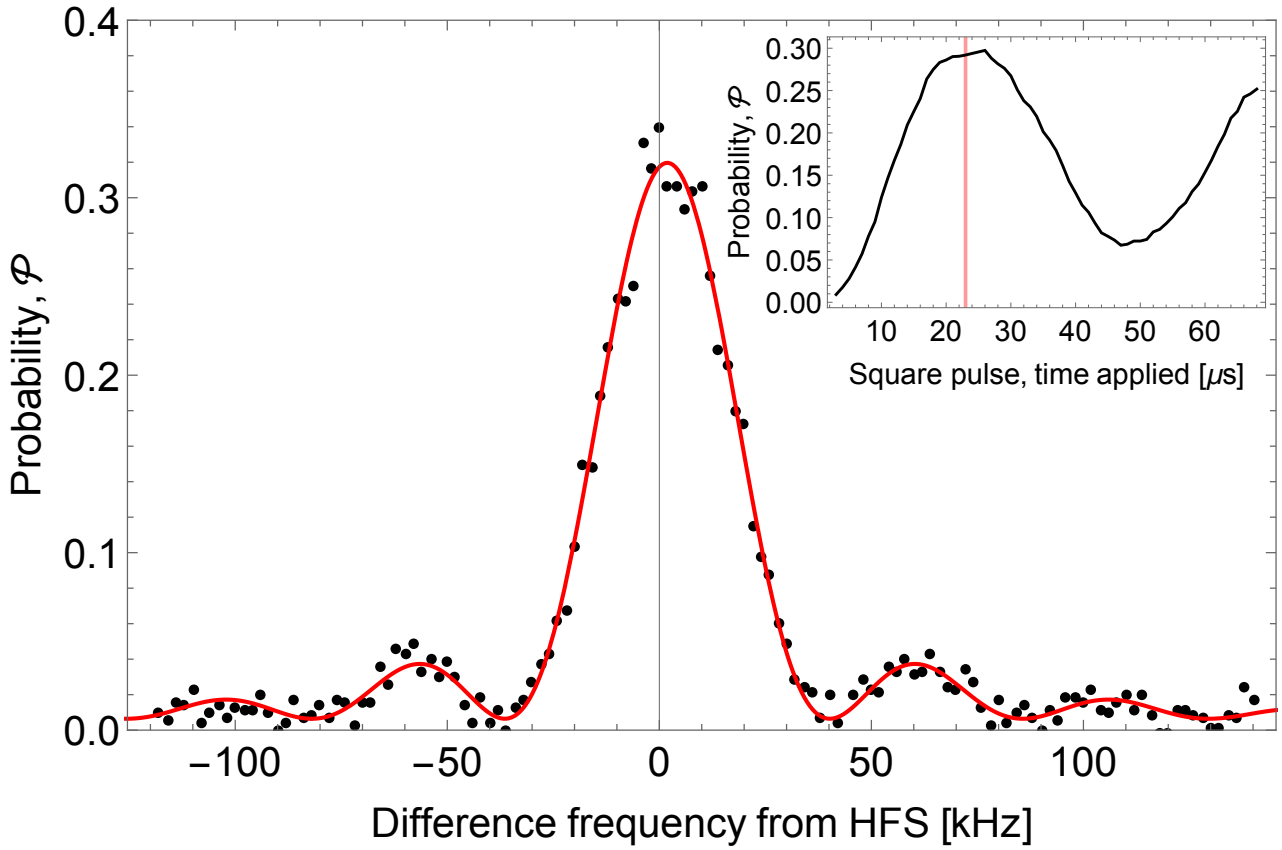

Figure 4.2: Co-propagating Rabi Flop and Raman Spectroscopy. A 23 μs square pulse drives the atoms in $|1,0\rangle$ to $|2,0\rangle$. The red line is a fit to equation (4.1). Inset: Rabi flopping by scanning the pulse time at the center frequency of the peak, confirming the π-time (demarcated by vertical red line).

where $m = m_I \pm m_J$, $x = \frac{(g_J - g_I)\mu_B B}{\Delta E_{HFS}}$, g_I is the nuclear g-factor, and μ_B is the Bohr magneton [43]. This equation gives the Zeeman shift of the energy levels. Knowing the frequency of the $m_F = \pm 1$ transitions allows me to calculate that the magnetic field at the position of the cloud is 480 mG. Closer inspection of i) and iii) in b) of Fig. 4.3 indicate that the applied magnetic field is homogeneous at the position sampled by the cold cloud; the line widths of all three pulses are the same, where I would expect the the magnetically sensitive sub-levels to have suffered inhomogeneous broadening in the presence of large gradients. The $m_F = \pm 1$ transitions are not exactly equidistant from the $m_F = 0$ transition in Fig. 4.3, but off by some 30 kHz; from Equation (4.2), I expect them to be off by only 33 Hz. This led to a study of what this shift might be, see Fig. 4.4.

I consider the scalar, vector, and tensor components of the light shift. They all produce a shift to the states as shown in a), b), and c) of Fig. 4.4. Only the tensor shift could supply such

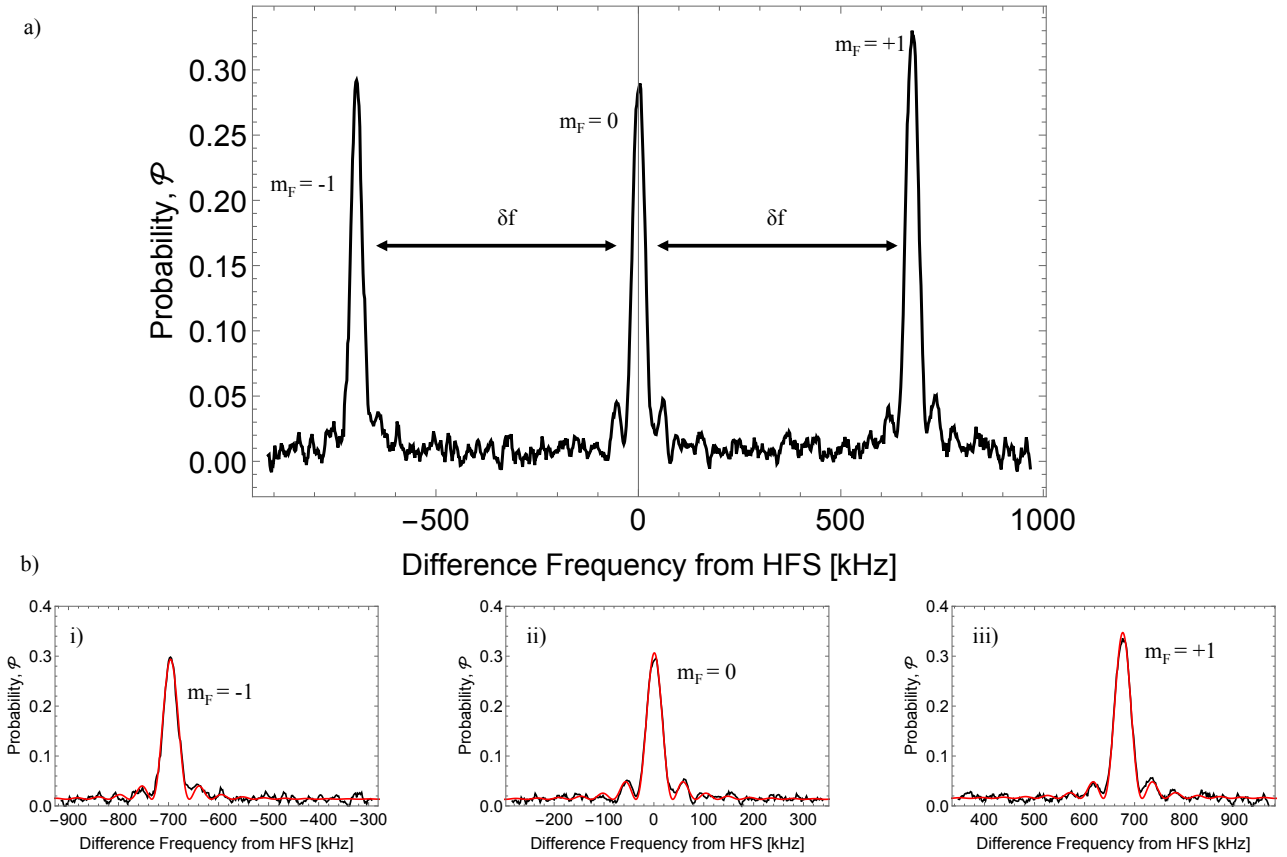

Figure 4.3: Co-propagating Raman Spectroscopy of F=1. a) The Raman spectrum showing the F=1 manifold Raman transitions approximately equidistant from the magnetically-insensitive state. The field applied is 480 mG. b) Upon closer inspection, the peaks are not quite equidistant. The red line are sinc fits to the spectrum. While I do not observe inhomogeneous broadening of the transitions, their lack of symmetry needs to be investigated.

a large asymmetry, but it would require an electric field just under 1 kV/cm, which is not possible. This led me to conclude it was a technical fault, and in fact the issue was heating of the drive electronics to the shim electromagnet and a poor sense resistor. The drive electronics were changed to those reported in the experiment section, see b) of Fig. 3.13, and the issue of non-symmetric state shifts was resolved.

I repeated the spectroscopy experiment of Fig. 4.3 with a lower applied field, producing symmetric magnetically sensitive transitions, see i), ii), and iii) in a) of Fig. 4.5. The Zeeman sub-levels of F=1 are split by $\delta f = \pm 511$ kHz in this test, corresponding to a magnetic field of 364 mG. The magnetically insensitive state, ii) in a), is -2 kHz away from the hyperfine splitting. I increased the applied magnetic field, see i), ii), and iii) of b) in Fig. 4.5. This test had two purposes: (i) to show that I had really solved the problem from the current driver and (ii)

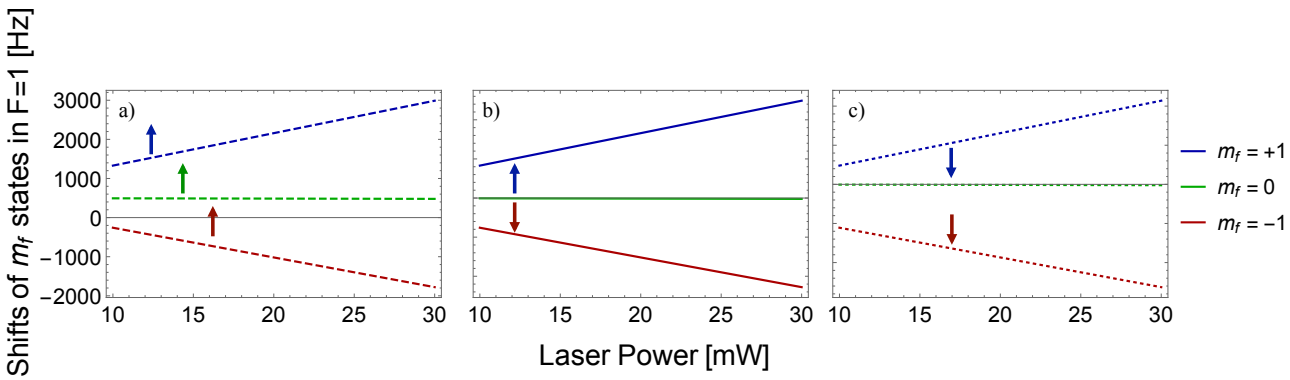

Figure 4.4: Scalar, vector and tensor shifts. a) Scalar shift: A shift of all the m_F states together, equally. This could be caused by Raman laser 1 at a sub-optimal frequency or the magic ratio being off. b) Vector shift: A shift in which the magnetically-sensitive states shift symmetrically from the unperturbed magnetically-insensitive state; since the insensitive state is actually affected to second order, a small shift is realized. This shift has a linear relationship with total beam intensity. c) Tensor shift: Moves the magnetically-sensitive states together.

to investigate how far I could split the Zeeman sub-levels. The μQuans laser offers large power outputs (in excess of 1 W), which gave me the opportunity to use very short π-pulses. Short pulse times lead to larger frequency widths that would allow me to select large momentum distributions from the cold cloud in counter-propagating configurations. This is not possible with small applied magnetic fields and so small Zeeman sub-level splitting, as a short pulse will inadvertently drive the $|1,1\rangle \rightarrow |2,1\rangle$ and $|1,-1\rangle \rightarrow |2,-1\rangle$ transitions. I found that I could apply a magnetic field up to 2 G. I show a high field test in i), ii), and iii) of b) in Fig. 4.5; the Zeeman sub-levels are split by $\delta f = \pm 2180$ kHz, or 1.551 G. Before this test, I had realigned the loading of the 2D MOT into the 3D MOT which involved tweaking the position of the 3D MOT. While this did not change the temperature of the cloud, it changed the distribution of atoms among the three Zeeman sub-levels of F=1. For the rest of this section using co-propagating Raman beams, the field is set to 1 G.

Next, I checked the polarization dependence of the transitions. In co-propagating beam configurations, the $\Delta m_f = 0$ transitions have maximum transition strength with Lin$\perp$Lin polarization and are forbidden with circular polarization. I took spectra like a) in Fig. 4.3 where I changed the waveplate angle in 5 degree steps, as shown in a) and b) of Fig. 4.6. Each turn of the waveplate toward circularly polarized light decreased the transition probability across all Zeeman sub-levels in the F=1 manifold. The peak transition probability goes like $\cos^2(\theta)$, where

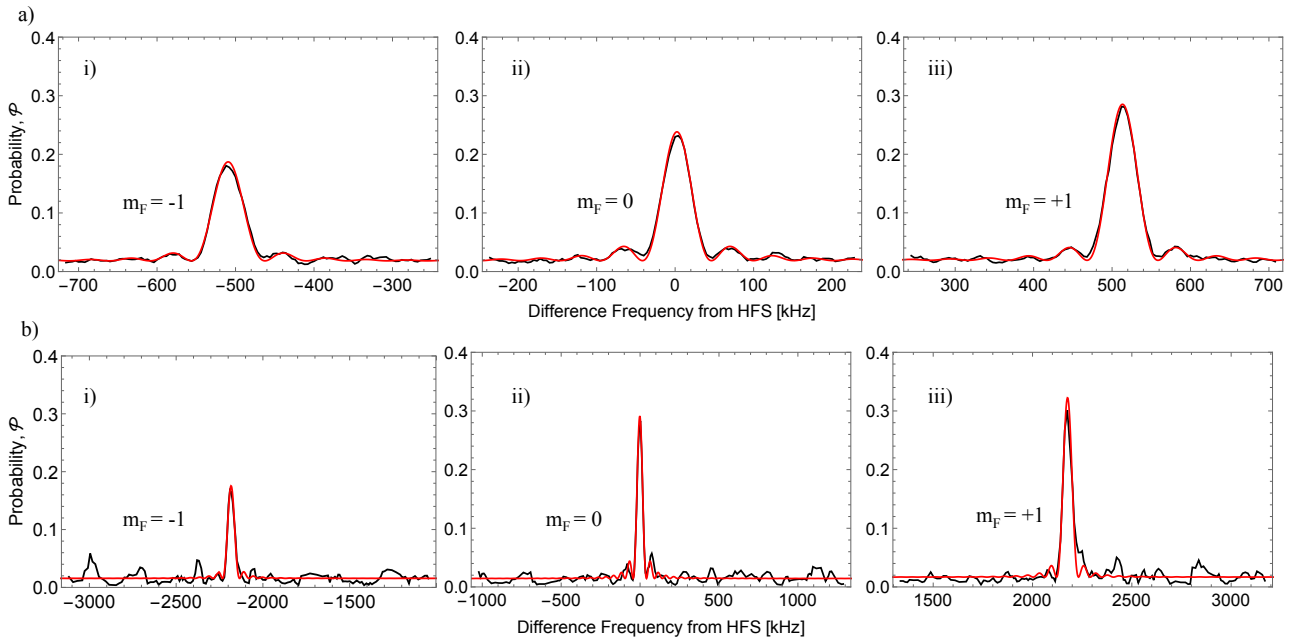

Figure 4.5: Doppler-insensitive Raman Spectroscopy of F=1 at different magnetic fields. The data is in black, fits are in red. a): i), ii), and iii): Spectroscopy following Fig. 4.3 to ensure that the magnetically sensitive states and their separation is understood. b): i),ii), and iii): Larger applied magnetic field leads to larger splitting. This series was scanned with less resolution.

θ is the waveplate angle referenced to the fast axis, shown in c) of Fig. 4.6; the rotation mount used was not aligned with the waveplate's fast axis making the wave plate angle axis arbitrary.

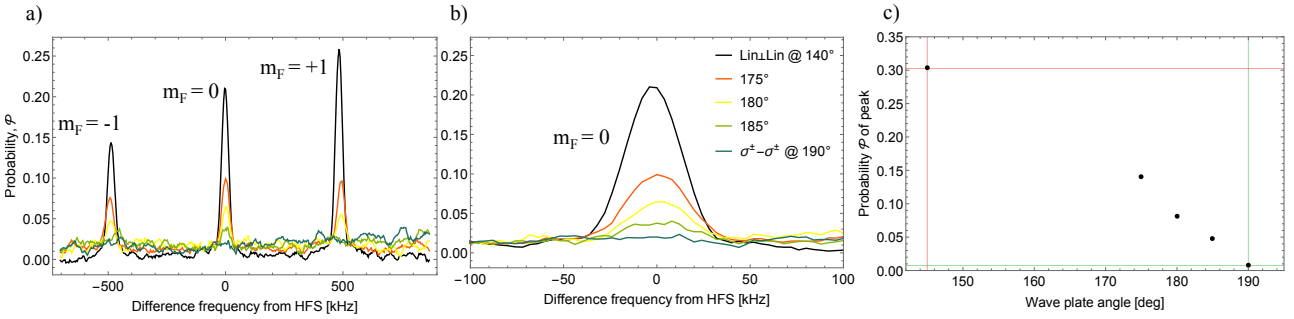

Figure 4.6: Transitioning from Lin⊥Lin to circular polarization. a) The spectra show the transition probability decreasing equally across the states as the waveplate is rotated. b) Closer inspection of $|1,0\rangle \rightarrow |2,0\rangle$ transition. c) The peak probability $\mathcal{P}$ of the magnetically-insensitive state in co-propagating configuration as a function of $\lambda/4$ waveplate angle.

In this subsection, starting with tests of the π-pulse time and power, I was able to scan the frequency difference between the Raman lasers and resolve the splitting of the Zeeman sub-levels of F=1 by my applied magnetic field. I was able to solve problems related to the Zeeman splitting, test larger applied fields, and demonstrate the polarization dependence of the transition strength.

4.1.2 Ramsey Interferometry

A natural progression from this point is to add another pulse. This is Ramsey's method [7,50]. First, I must develop a state selection scheme that is more restrictive than selecting the entire manifold, as in the previous subsection. I need to select atoms in only the $m_F = 0$ Zeeman sub-level of either F=1 or F=2; I select $|1,0\rangle$, as described next. This state selection technique also lends itself to selecting a velocity distribution of the cold cloud, which I discuss at the beginning of the next section on counter-propagating studies.

State preparation

I need to employ a state preparation scheme. I no longer allow the atom to fill the F=1 manifold but instead leave the repump light on when I extinguish the Sisyphus cooling beams. This leaves all the atoms in the F=2 manifold. I use a Raman π-pulse to move atoms from F=2, m_F=0 to F=1, m_F=0 and then blow away the rest of the atoms populating the F=2 manifold. To blow away the atoms in F=2, I apply blue-detuned (+1Γ) cooling light near the saturation intensity to the atoms over all 6 3D MOT beams for 1 ms. This heats the atoms left in F=2, causing them to leave the interferometer region well before detection. This method of state preparation is simple in execution but severe in terms of atom loss, see Fig. 4.7. I perform two checks to ensure no Zeeman sub-level other than $|1,0\rangle$ is populated. First, I perform detection, as detailed in previously in Fig. 3.21, and observe no atoms in the F=2 manifold. I then ensure the $m_F = \pm 1$ Zeeman sub-levels are clear by scanning the frequency of a second Raman π-pulse (π-time of 50 μs), see Fig. 4.8.

I want to perform interferometry at different free propagation times T. My atoms are falling through the intensity profile of the beam and I need to ensure that I can drive a Rabi flop for all times T of interest and availability. Fig. 4.9 shows damped Rabi oscillations after different fall times. At fall times past 20 ms, like in c) of Fig. 4.9, the Rabi oscillations begin to show decreased Rabi frequency. As the cloud expands the atoms sample a larger range of intensities; atoms in different parts of the cloud see increasingly different Rabi frequencies and

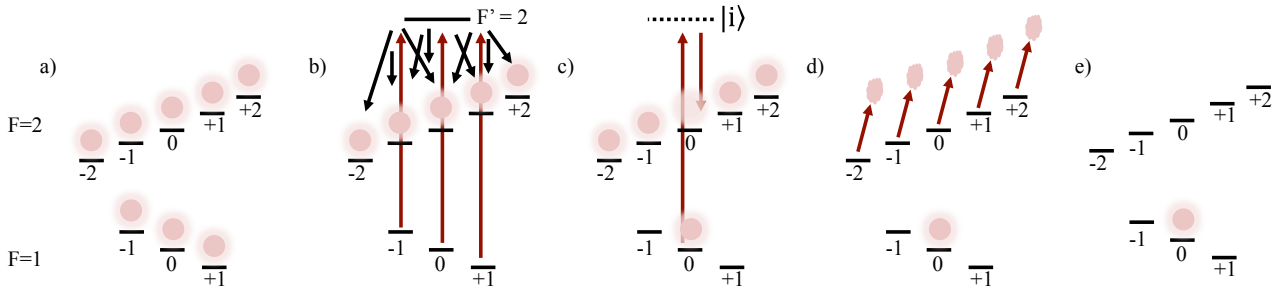

Figure 4.7: Preparing the cloud in F=1, $m_F = 0$. a) During Sisyphus cooling, the atoms are distributed amongst the 8 Zeeman levels of the two hyperfine ground states. b) Leaving the repump on during Sisyphus cooling and some time after deposits all atoms in the 5 Zeeman levels of the F=2 ground state. c) A π pulse transfers some population of $|2,0\rangle$ to $|1,0\rangle$. During co-propagating experiments, this pulse is typically a 15 μs square pulse and is resonant with the hyperfine splitting and the co-propagating transition. For the counter-propagating Doppler-sensitive experiments of the primary experiment, the pulse is 4.5 μs and slightly detuned (-72 kHz). d) The atoms left in the 5 Zeeman levels of F=2 are blown away using slightly blue-detuned cooling light (10 MHz) just above I_{sat}. e) The atoms left are all in $|1,0\rangle$, with all other states empty. The atom loss is severe; in b), around 20% of the total atom number is in the $|2,0\rangle$ state. In co-propagating, I select $\geq 90\%$ of these atoms. In Doppler-sensitive experiments, this falls to 14-17% of the total atom number.

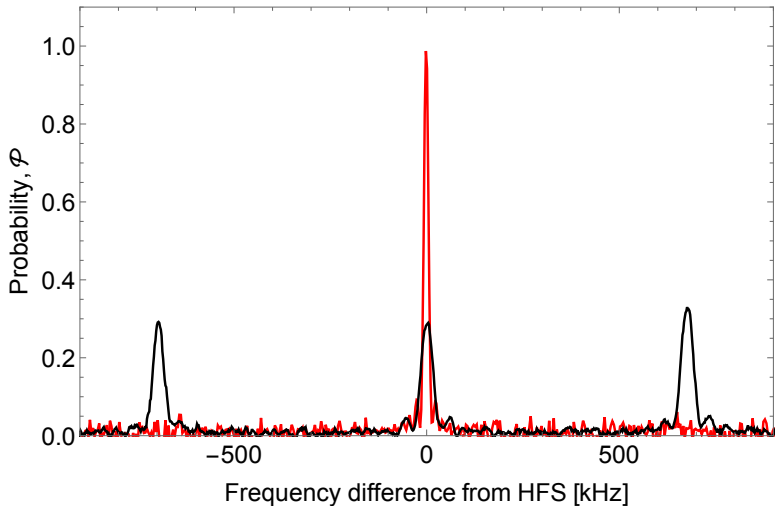

Figure 4.8: Clearing of states. In black, the co-propagating transitions showing equally filled magnetic levels of F = 1. In red, after state selection and clearing there are no atoms located in the $|1,-1\rangle$ and $|1,1\rangle$ states as evidenced by their being no detectable transition probability.

the oscillation loses coherence faster than at fall times closer to the peak intensity and smallest cloud size.

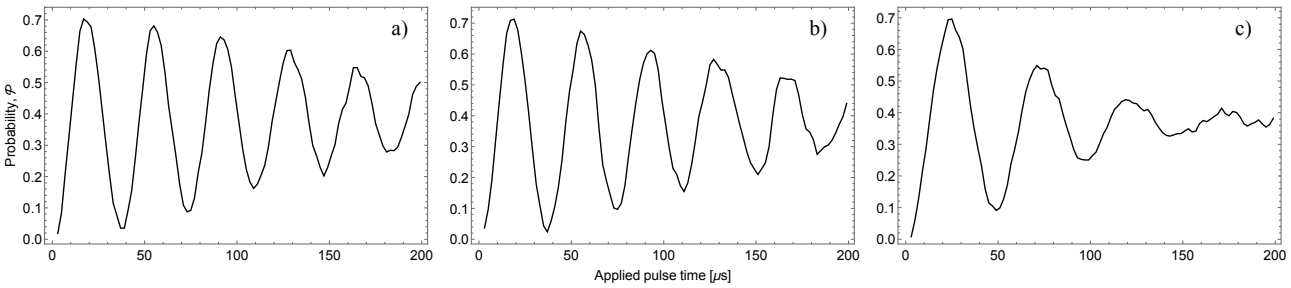

Figure 4.9: Co-propagating Rabi oscillations at multiple fall times. As time goes on, the cloud flops at a longer frequency, especially at later fall times, as the cloud travels through the Raman beam intensity profile and expands. The nominal pulse time is 18 μs. Fall time: a) 0 ms, b) 16 ms, and c) 32 ms.

4.1.3 Ramsey's method with frequency and phase scanning

Having shown that I could prepare a cloud in $|1,0\rangle$ and with Rabi oscillations mapped out throughout fall times up to 40 ms, it was the ideal time to add another pulse. First, I scanned the frequency of the two $\pi/2$-pulses, of duration τ, with a fixed free-propagation time T. I show an example with T = 1 ms and $\tau = 12$ μs, see Fig. 4.10. The red line is a fit to the function [7],

$$\mathcal{P} = A\frac{\Omega^2}{\delta^2+\Omega^2}\sin\left[\frac{\tau}{2}\sqrt{\delta^2+\Omega^2}\right]\Big|i(e^{i(0.5\delta_0 T-(\phi+(\tau+T)(\delta+\delta_0)))} - e^{-i(0.5\delta_0 T+\tau(\delta+\delta_0))})\times \left(\cos\left[\frac{\tau}{2}\sqrt{\delta^2+\Omega^2}\right] + \frac{i\delta}{\sqrt{\delta^2+\Omega^2}}\sin\left[\frac{\tau}{2}\sqrt{\delta^2+\Omega^2}\right]\right)\Big|^2 + B \tag{4.3}$$

where Ω is the Rabi frequency, δ is the frequency difference from the hyperfine splitting, δ_0 is the frequency offset from the hyperfine splitting, ϕ is the phase difference between the two pulses, and A is an amplitude scaling factor and B is the background. The equation was derived from the same method used to determine the probability for the three pulse interferometer, equation (2.13), with only three interaction matrices $\mathcal{Q}_5\mathcal{Q}_2\mathcal{Q}_1$; it includes two $\pi/2$ pulses sandwiching a free propagation time interaction matrix. For this test, the value of ϕ was set to 0. I found $A = .85$ and $B = .07$. The data in this scan under-samples the fringe pattern, with about one point per fringe. I look at the center 20 kHz, a) of Fig. 4.10, to illustrate more clearly that the

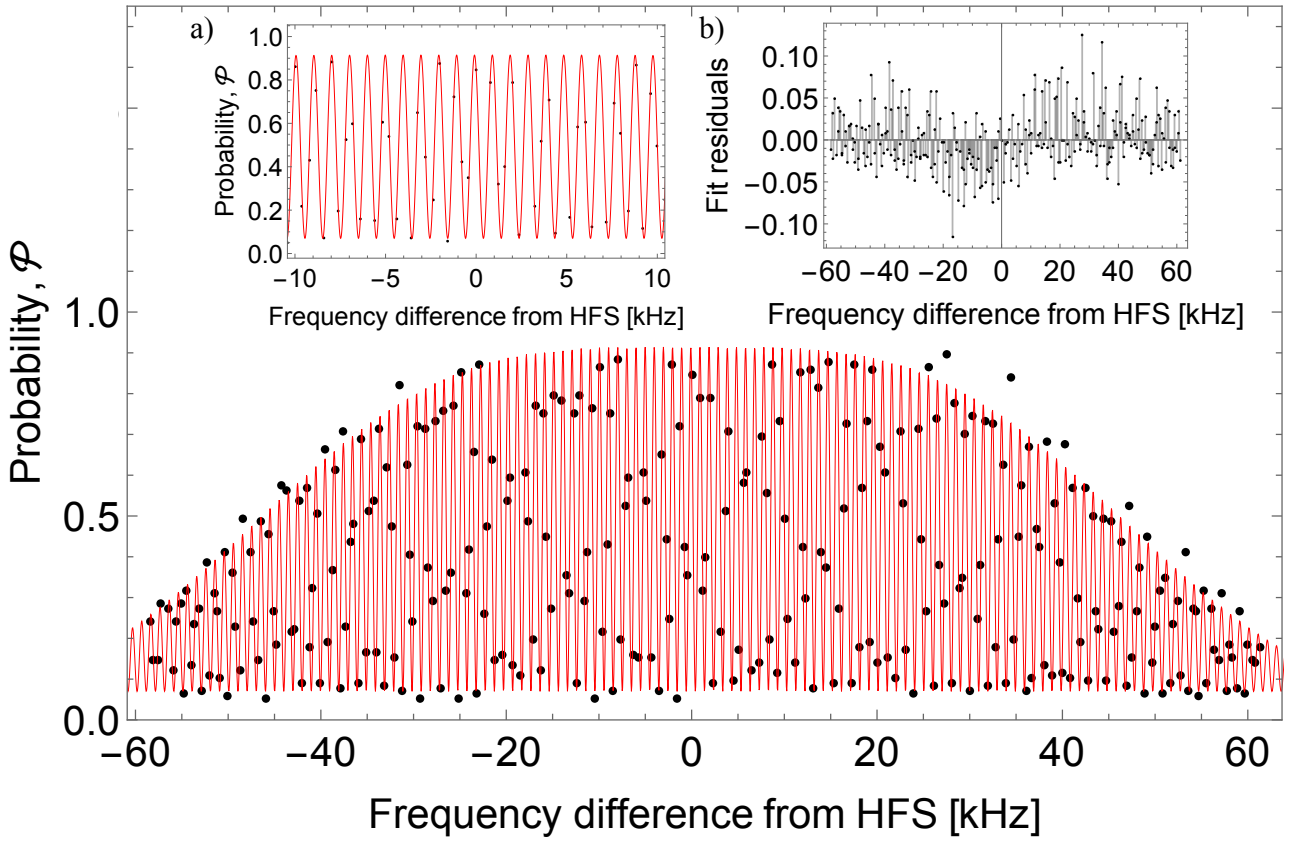

Figure 4.10: Ramsey's method: scanning the frequency of both pulses. Ramsey's method with T = 1 ms and τ = 12 μs. The fit to equation (4.3) is in red. a) Close inspection of the center 20 kHz to ensure the fit describes the data. The center fringe is slightly off the hyperfine splitting, missing it by +572 Hz; this is from light shift. b) Fit residuals versus the frequency difference. The fringes are undersampled, meaning the residuals are of limited use apart from observing gross disagreement with the fit.

fit describes the points. The fit confirms that I used a $\pi/2$ time of 12 μs and T = 1 ms. While I had applied a value for the frequency offset of $\delta_0 = 0$, the fit tells me $\delta_0/2\pi$ = +572 Hz. This is from the light shift due to intensity imbalance of the beams. The Rabi frequency was found to be Ω=41.5 kHz, in agreement with what I would expect for my $\pi/2$ time. In b) of Fig. 4.10 I examine the residuals. Since the scan is under-sampled, I miss out on any finer oscillations or patterns but I can see no gross disagreement with the fit. I do note some outliers around -15 kHz and above +20 kHz.

I can perform Ramsey's method in another way. I scan the phase difference ϕ between the Raman beat note between the first and second pulse. Fig. 4.11 shows these fringes. The phase scan starts with an offset from the trough because of the aforementioned intensity imbalance; the +572 Hz offset shifts the phase of the fringe pattern. The fringes were scanned with T =

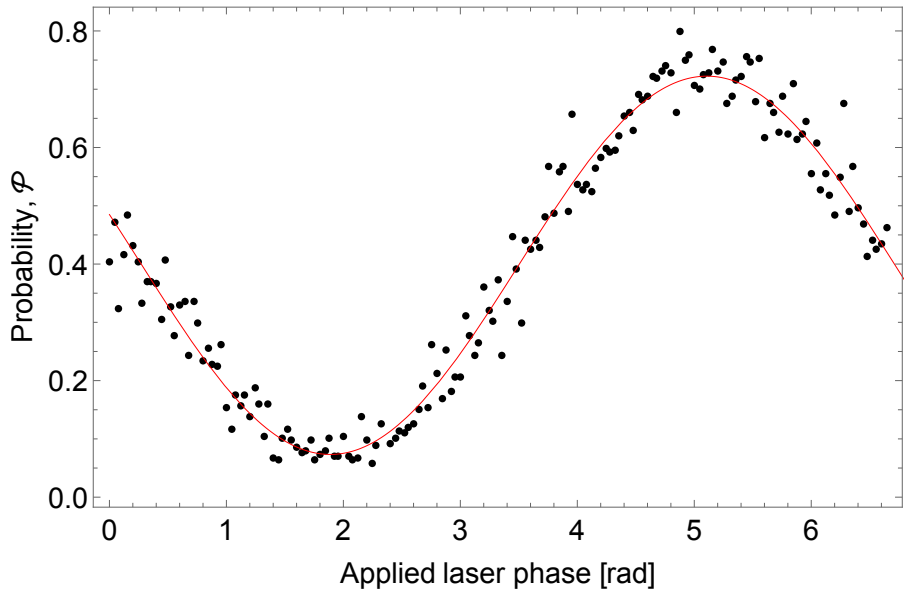

Figure 4.11: Ramsey's method: scanning the phase between the pulses. Note the same amplitude as Fig. 4.10. T = 30 ms and $\tau = 12$ μs. The thin red line is a fit to the $\cos^2$ function equation (4.4) implied by equation (4.3).

30 ms. I found that the $\pi/2$-time did not change in this case, even for such a long time T; both pulses required 12 μs pulses. Sufficiently close to the central fringe, equation (4.3) reduces to the form $\mathcal{P} \approx \cos^2[\phi/2]$ for fixed parameters bar ϕ. In 4.11, the thin red line is a fit to

$$\mathcal{P} = A\cos^2[\phi - \phi_0] + B \tag{4.4}$$

where A is the fringe amplitude, ϕ is the applied laser phase, ϕ_0 is the offset phase from the trough of the fringe and B is the background. The amplitude A is the same as the frequency scan, even at much longer times T. The phase scan data displayed in Fig. 4.11 suffered from low atom numbers due to short loading time and low partial pressure of Rb in the 2D MOT; the signal to noise ratio of these data is low, evidenced by the spread of points around the fit. These Ramsey tests confirmed that I could match theoretical interferometer predictions with the data. It told me that I needed to tweak the intensity balance between the Raman lasers and improve the signal to noise.

4.1.4 Spin Echo Interferometry

I now added a third pulse to the interferometer to make a spin echo. The same parameters were used as the Ramsey phase scan in Fig. 4.11 with the two noted improvements added; I increased the atom number and tweaked the intensity ratio. The pulses times were $(\pi/2 - \pi - \pi/2) \rightarrow (12\ \mu s - 24\ \mu s - 14\ \mu s)$ and the time between the pulses was T = 15 ms.

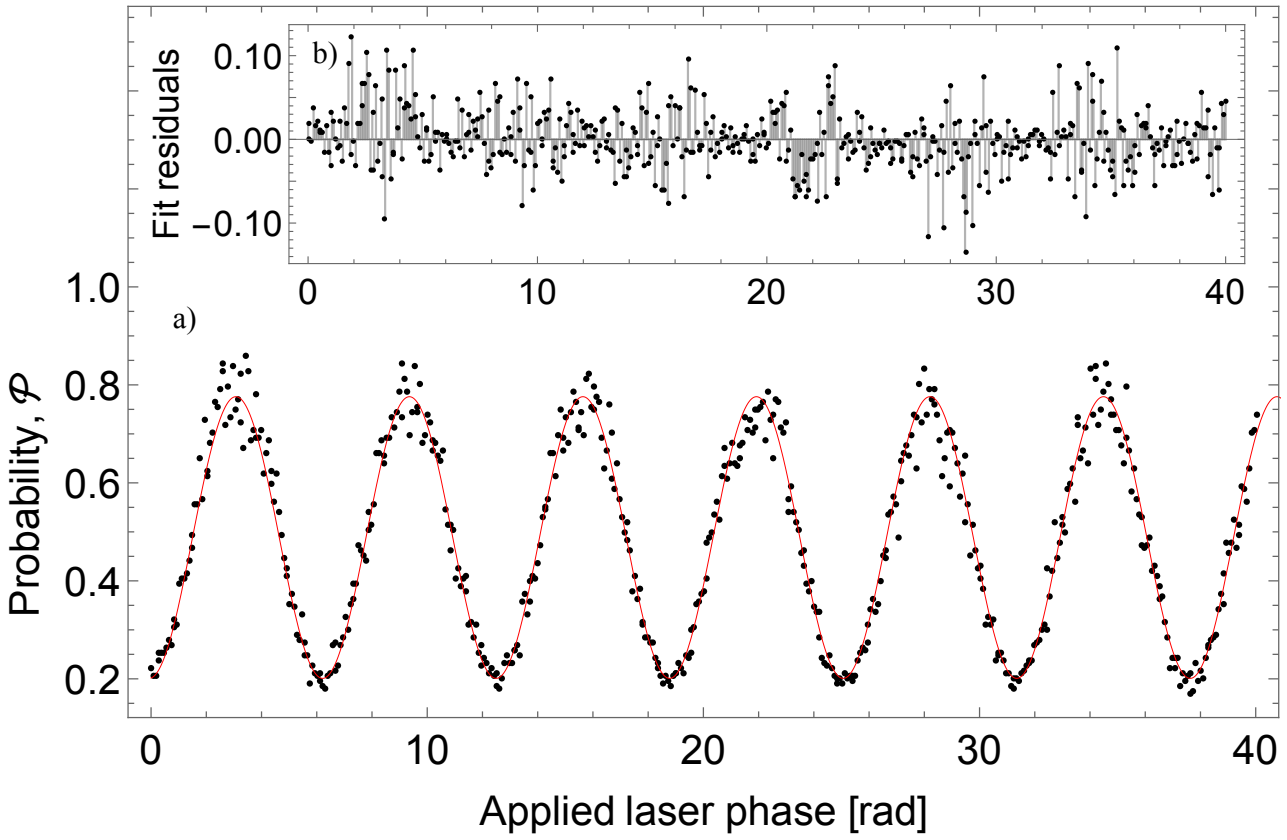

Figure 4.12: Velocity-insensitive spin echo interferometry. a) A phase scan for 2T = 30 ms showing 6 fringes up to 40 radians. The thin red line is the fit to equation (4.4). Note the fringes start at the trough instead of half way up the fringe like in Fig. 4.11, after adjusting the intensity ratio. b) Fit residuals versus the applied laser phase; far from being undersampled, these fringes show good agreement with the fit.

The phase scan, see a) in Fig. 4.12, shows fringes with the same peak probability as 4.11 but with a larger background. This is probably due to dephasing resulting from spontaneous scattering. The fit, from equation (4.4), is the thin red line. The data displays improved signal to noise and starts at the trough for $\phi = 0$. The residuals, see b) in Fig. 4.12, show increased dispersion at the peaks of the fringe pattern. This effect is primarily due to variations in the total atom number in the interferometer due to variations in the atom loading. The full

amplitude from peak to trough of the phase scan in Fig. 4.12 is 0.575.

The spin echo interferometer concluded my studies of co-propagating Raman transitions. Having demonstrated my ability to make a three-pulse interferometer, I now want to make the interferometer acceleration-sensitive; this requires counter-propagating Raman beams.

4.2 Studies with Counter-propagating Raman beams

4.2.1 Velocity selection

Removing the beam block gave the possibility of driving a Raman transition with counter-propagating laser beams, see b) and c) in Fig. 4.1. Experiments performed in this configuration are sensitive to the finite velocity distribution of the atom cloud [51]. For my first spectroscopy test, I use the configuration of b) in Fig. 4.1, but with the polarization Lin⊥Lin. I use a 10 μs π-pulse for the velocity selection step, c) of Fig. 4.7, which corresponds to a velocity selection width of $\pm$1 cm/s; the frequency of this pulse was detuned by -78 kHz which corresponds to a velocity selection centered around -3 cm/s. It is useful to understand the width of the velocity selection in terms of temperature. The pulse time corresponds to Fourier width of $\nu_f = (\tau)^{-1}$ of about 27 kHz. I can convert this to a velocity,

$$v = \frac{\nu_f c}{2\nu_{las}}, \tag{4.5}$$

where c is the speed of light and ν_{las} is the transition frequency. The temperature selection width of the 10 μs pulse is then

$$T = \frac{mv^2}{k_B} \approx 1.1\mu\text{K} \tag{4.6}$$

where m is the mass of the ^{87}Rb atom and k_B is Boltzmann's constant. In the configuration where both pairs of beams are resonant, b) of Fig. 4.1, I expect to observe two peaks despite my laser being detuned to -78 kHz; the opposite beam pair will be resonant with the equal but opposite velocity class along the beam axis. To observe my velocity selection, I apply a second

π-pulse of 50 μs. The Fourier width of this pulse is narrower than the velocity selection pulse, offering improved resolution.

The spectrum presented in Fig. 4.13 is a scan of the Raman difference frequency around the hyperfine splitting of the second pulse. The inset is a Rabi flop on the selection frequency, -78 kHz. The outermost peaks are the velocity selected atoms, shifted due to the Doppler effect, and the center peak is the co-propagating transition, resonant irrespective of velocity. The atoms have zero center-of-mass motion and are cold (5 μK, 0$\pm$2.2 cm/s); fewer atoms are selected the further I move the selection frequency away from the hyperfine splitting. The Fourier width of the selection pulse is sufficiently wide that the selection centered on -78 kHz selects atoms in the class centered at +78 kHz. To ensure the magnetically sensitive transitions were suppressed while using short Raman pulses, I set the applied magnetic field to 1.5 G for this entire section.

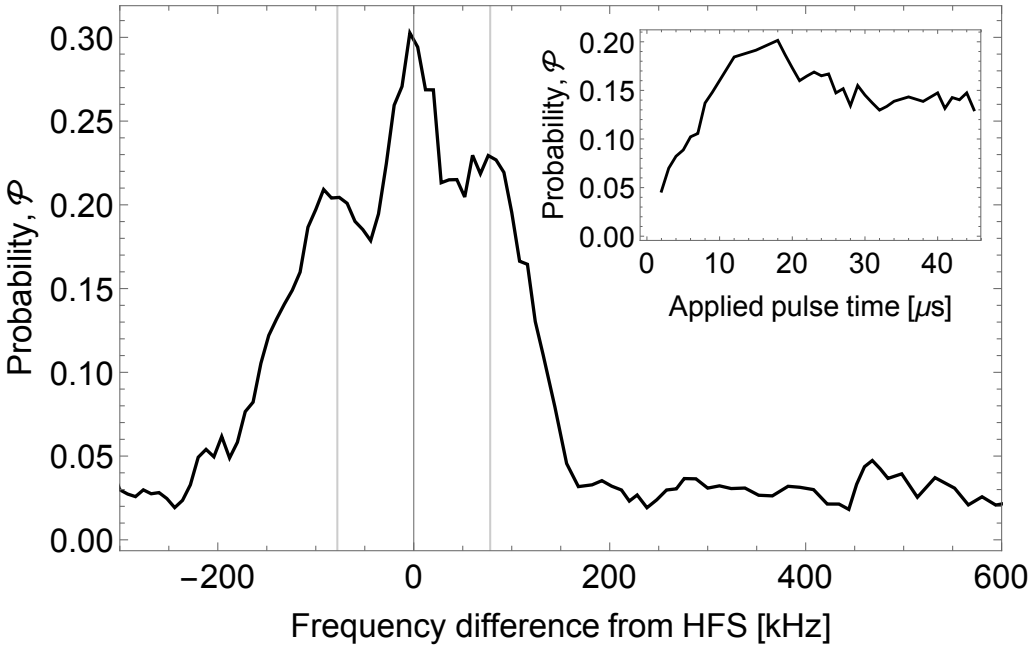

Figure 4.13: Counter-propagating Raman spectroscopy and Rabi flopping with two velocity classes. The velocity selection pulse, a 10 μs π-pulse, was detuned by -78 kHz. The spectrum was resolved with a 50 μs π-pulse. Note the two velocity classes, one to each side of the co-propagating transition, marked by gray lines. The center black line marks the co-propagating transition. Inset: a Rabi flop on the velocity selected atoms, in preparation for Fig. 4.15.

I change the optics, c) of Fig. 4.1, and test my ability to select a single velocity selection, Fig. 4.14. I make a velocity selection with a 4.5 μs π-pulse detuned by -72 kHz with respect to the

hyperfine splitting. It is probed by a 50 μs π-pulse. This selection addresses a Fourier width of about 58 kHz, equivalent to a velocity spread of $\pm$2.3 cm/s around the detuning of -72 kHz or -3 cm/s. The equivalent temperature is 5.4 μK. I had changed the waveplate orientation to circular to drive the $\sigma_-\sigma_-$ transition for this test; my failure to tweak the waveplate appropriately resulted in a reduced co-propagating peak still appearing. It was subsequently corrected. Fig. 4.14 shows the result of this scan; a large velocity peak centered around -72 kHz and no peak on the opposite side at +72 kHz.

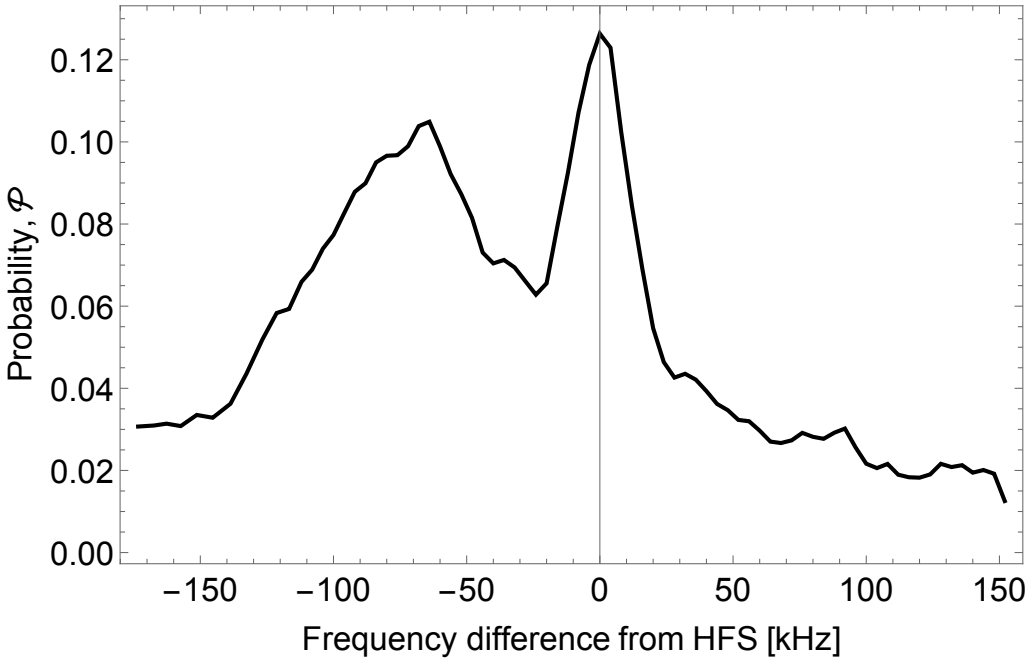

Figure 4.14: Single velocity selection. Doppler-sensitive two-pulse Raman spectroscopy investigating the momentum class selection. The polarization was improperly set, showing a reduced co-propagating transition.

4.2.2 Checking the applied phase accuracy with the atom interferometer

Using these velocity selections, I started out at small times 2T to observe interference patterns, see Fig. 4.15. I show a fringe pattern with 2T = 1 ms, using pulse times $(\pi/2 - \pi - \pi/2) \rightarrow (7\ \mu\text{s} - 14\ \mu\text{s} - 7\ \mu\text{s})$. I scanned the applied laser phase on the third pulse, out to 200 rad. This data serves a purpose beyond demonstrating acceleration-sensitive fringes; this dataset is a calibration of the applied laser phase. It is critical before continuing that I know how accurate

my phase commands are. Later, I flop the applied laser phase between ϕ_0 and $\phi_0 + \pi$ and perform a subtraction to suppress any amplitude and background fluctuations. The accuracy of the phase command is crucial when performing this subtraction $(\phi_0 + \pi) - (\phi_0)$. The red line is a fit to

$$\mathcal{P} = A\cos^2\left[q(\phi + \phi_0)\right] + B, \tag{4.7}$$

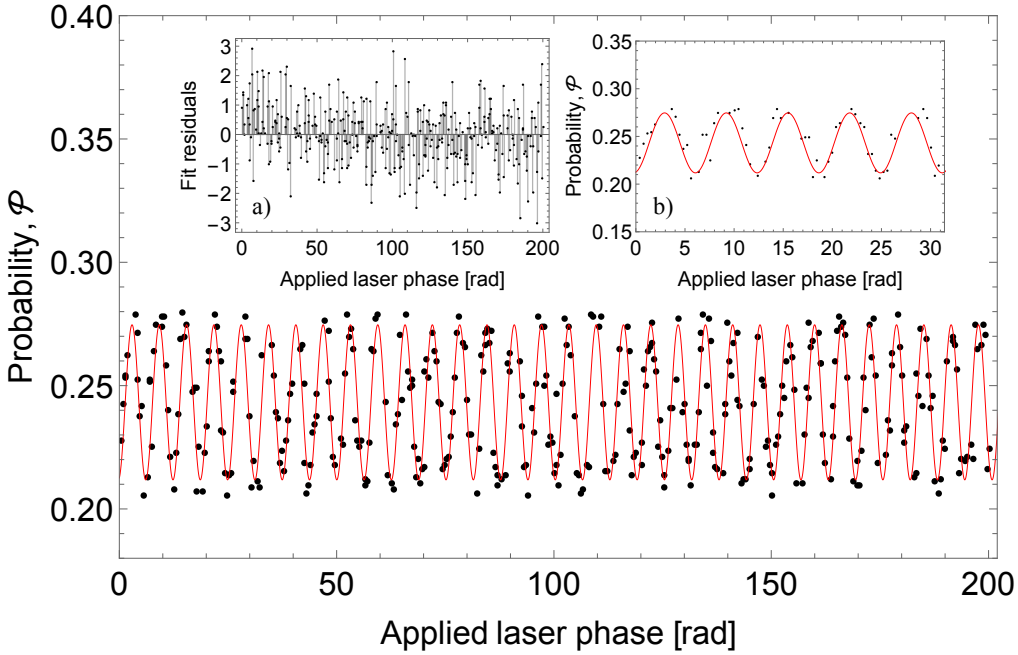

Figure 4.15: Atom interferometry with two velocity classes and circularly polarized light. The parameters for this trial are as follows: 2T = 1 ms and pulse lengths of $(\pi/2 - \pi - \pi/2) \rightarrow (7\ \mu s - 14\ \mu s - 7\ \mu s)$. The velocity selection π-pulse was 13 μs. The fit, in red, is to equation (4.7). This Raman beams were circularly polarized; there was no co-propagating component present. a) The fit residuals versus the applied laser phase. The points are well described by the fit. b) A closer look at the first few fringes.

where A is the amplitude, B is the background, ϕ_0 is the offset phase and q is my parameter of interest, the phase command calibration which I expect to be 1. I measure the same background as in Fig. 4.12, but I observe a reduced fringe amplitude. The peak to trough contrast is 0.06. The fit gives me a value for the calibration of $q = 1.0001 \pm 0.0004$; this is sufficient to ensure my phase commands do not add error to the subtraction. In a) of Fig. 4.15 I show the residuals. The residuals show this data is noisier than Fig. 4.12, probably due to vibrations and sensitivity to the initial position and velocity distribution of the atoms. To illustrate the data follows an oscillatory pattern, I zoom in on a selection of the dataset in b) of Fig. 4.15, where I show the first 30 rad.

Fringe pattern comparison for different velocity selections

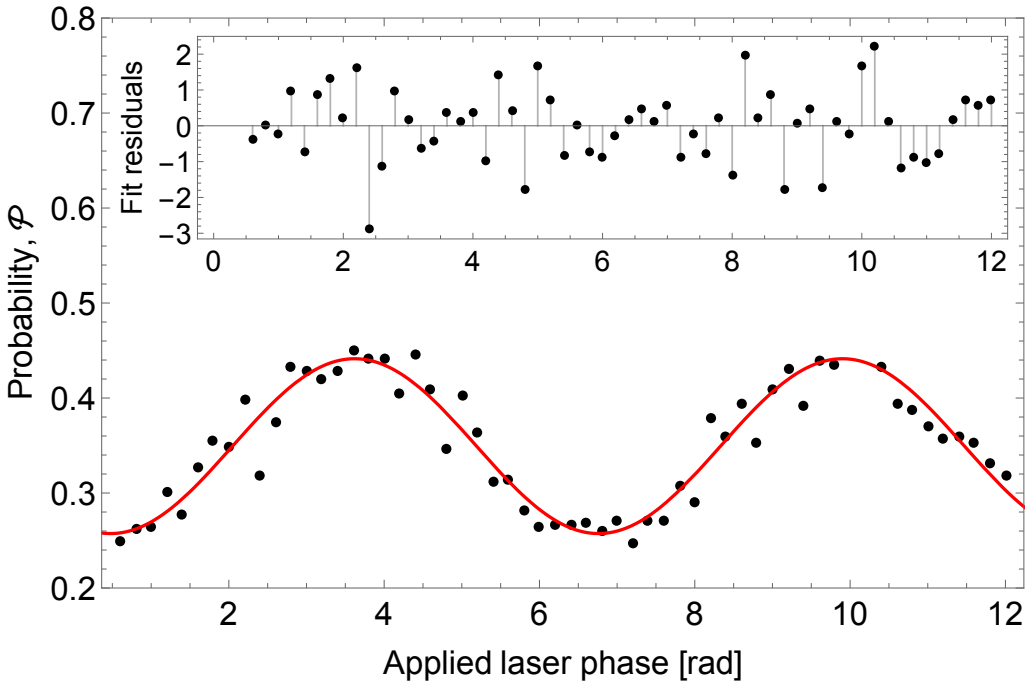

Figure 4.16: Single velocity class atom interferometry. Demonstrated here with a time 2T = 32 ms, the pulse times are short, $(\pi/2 - \pi - \pi/2) \rightarrow (2.05\ \mu s - 4.7\ \mu s - 3.2\ \mu s)$. The inset shows the fit residuals versus applied laser phase.

This method of making acceleration-sensitive fringes, using two velocity classes, proved difficult to realize at larger 2T times. The fringe contrast produced using this method was also limited. These limitations directly affected the prospective acceleration sensitivity. To see if I could get around these problems, I choose to extinguish a frequency at the retro-reflection, see c) in Fig. 4.1, and use a single velocity class, Fig. 4.14. Having extinguished a pair of beams, I leave only the $\sigma_-\sigma_-$ transition resonant. This beam polarization, in conjunction with my velocity selection around -72 kHz, selects an atom cloud that is moving toward the retro-reflection mirror. Using this cloud I make a Kasevich-Chu style atom interferometer, see Fig. 4.16.

I started with interferometers at small times 2T. I was able to increase the 2T time up to the point when the atom cloud leaves the beam cross section capable of driving Rabi flops, around 43 ms. The interferometer with the best contrast occurred with $2T = 32$ ms; this is just after the point when the last $\pi/2$ time starts to differ from the first. The pulse times used are very short, almost as short as the 4.5 μs velocity selective pulse: in order of $(\pi/2 - \pi - \pi/2)$, the times are $(2.05\ \mu s - 4.7\ \mu s - 3.2\ \mu s)$. This limits the contrast, but was required in order to

select enough atoms. The last $\pi/2$ time is 1 μs different from the first at 2T = 32 ms due to the atoms falling through the intensity profile of the Raman beam, changing the Rabi frequency; moving to times larger than 2T = 32 ms resulted in a loss of contrast due to the changing efficiency of the final pulse. These are the pulse times in the primary experiment described in the next chapter. I show a phase scan of 4π at 2T = 32 ms in Fig. 4.16. The red line is a fit to equation (4.7). The pattern displays a trough at zero phase and a full amplitude of 19%. The residuals displayed in the top inset of Fig. 4.16 are less noisy than Fig. 4.15 at significantly longer 2T time.

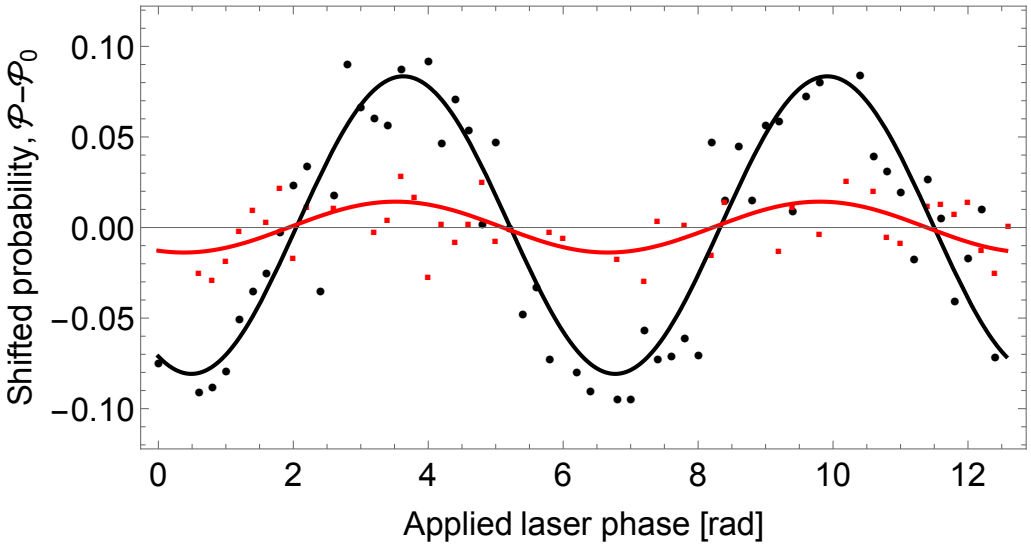

Figure 4.17: Comparison of velocity selection techniques. With a time 2T = 5 ms, the disparity in contrast and noise is readily apparent between the single velocity selection (black) and the double velocity selection (red).

I show a comparison between double and single velocity selection configurations. The fringe patterns have different backgrounds; to compare them, I modify the probability $\mathcal{P}$ by subtracting the mean probability from each fringe. I create the mean probability $\mathcal{P}_0 = B + A$, the background plus half the peak to trough amplitude. I show this in Fig. 4.17, where I display the double velocity selection case (red) and the single velocity selection case (black). These fringe patterns have the same pulse times and 2T time. The single-diffraction case (black) is higher contrast and less noisy than the same double single-diffraction case (red). I perform this test over a series of 2T times for both the double and single velocity selection fringe patterns and compare their peak to trough amplitude, see Fig. 4.18. The conclusion is clear; I will use the single velocity selection for maximum acceleration sensitivity.

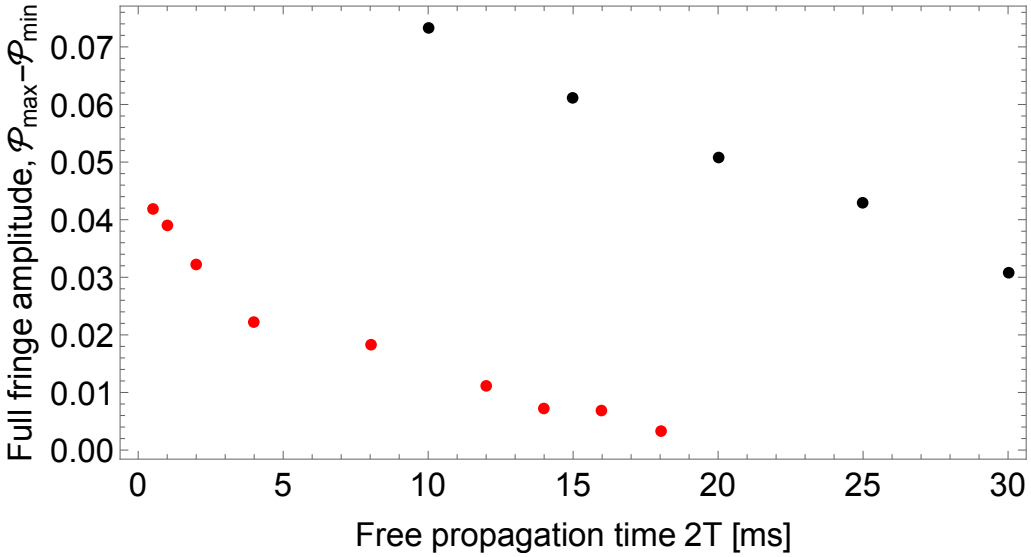

Figure 4.18: Velocity selection comparison. As the 2T time increases, the contrast shrinks as vibration and decreasing Rabi frequency of the last pulse smear out the fringe pattern. Clearly shown is the performance difference between the double velocity selection (red) and the single velocity selection (black) in this system.

4.2.3 Calibrating the MEMS accelerometer with the atom interferometer

The atom interferometer measures background accelerations as well as the small anomalous signal I seek. The MEMS accelerometer on the retro-reflector could separate all background accelerations from my signal because it is not sensitive to the anomalous acceleration while the atom interferometer is. Previously, I scanned the applied laser phase on the last $\pi/2$-pulse to observe a fringe pattern. Now, I simply let a combination of vibrations and table wallowing, the unrestricted and small tilting of the floated optical table, scan out a fringe pattern.

The MEMS accelerometer comes with a given calibration of $\Xi = 1.37572 \times 10^{-4}$ A/(m s^{-2}); this means there is a calibration value I can expect from the MEMS accelerometer. The current from the accelerometer is converted to a voltage reading of the ADC in the computer interface, see Fig. 3.16. The resistor there has been calibrated by injecting a known current, measured by a high-precision ammeter (Keysight 34461A, 6.5 digit), and recording the voltage, see Fig. 4.19. The values of multiple readings are plotted in Fig. 4.19; they give me a linear fit $V = 9816.68(18)I + 150(17) \times 10^{-6}$. Combining the slope, R, of this fit and the specified

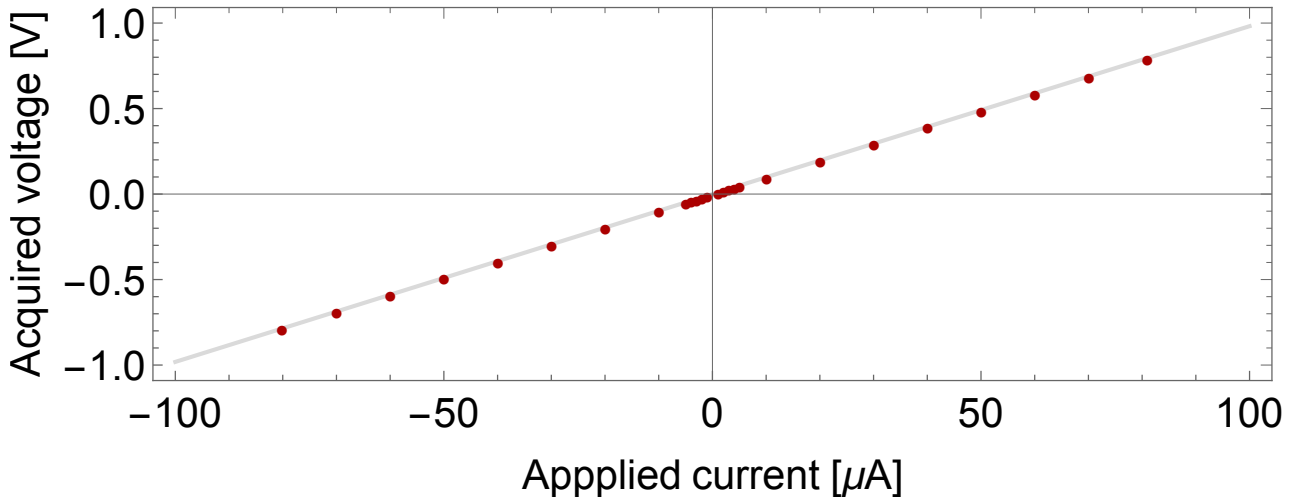

Figure 4.19: Response of MEMS electronics. The linear relationship between a known, applied current to the electronics of v) of a) in Fig. 3.16 and the acquired voltage, allowing me to determine the resistance R.

sensitivity Ξ of the MEMS accelerometer, I obtain the an expected calibration

$$\xi = \frac{1}{\Xi R} = 0.74046 \pm .00001 \ \frac{\text{m s}^{-2}}{\text{V}}, \tag{4.8}$$

where the error is dominated by the error in the measured value of the resistance.

I want to empirically measure this calibration using the atom interferometer, see Fig. 4.20. Before a data run, a phase scan allows me to establish a value for $\phi_{\text{las}} = \phi_0$ such that the interferometer is most sensitive to changes of acceleration, a scan which looks like Fig. 4.16. I measure the MEMS voltage for each shot as established in section 3.7, see a) in Fig. 4.20. I switch the phase from $\phi_{\text{las}} = \phi_0$ to $\phi_{\text{las}} = \phi_0 + \pi$ between shots and subtract, obtaining a fringe pattern with the background suppressed, see b) and c) in Fig. 4.20. In Fig. 4.20, this subtraction is performed on the atom accelerometer running near midday on August 28, 2017; c) shows a fringe pattern scanned out by the table tilting. I plot this data versus the MEMS accelerometer voltage reading. I use this to calibrate the MEMS accelerometer.

I fit the data of c) in Fig. 4.20, the red line, to

$$\mathcal{P}_* = A \cos\Big(\beta(V_0 + V_{\text{MEMS}})\Big), \tag{4.9}$$

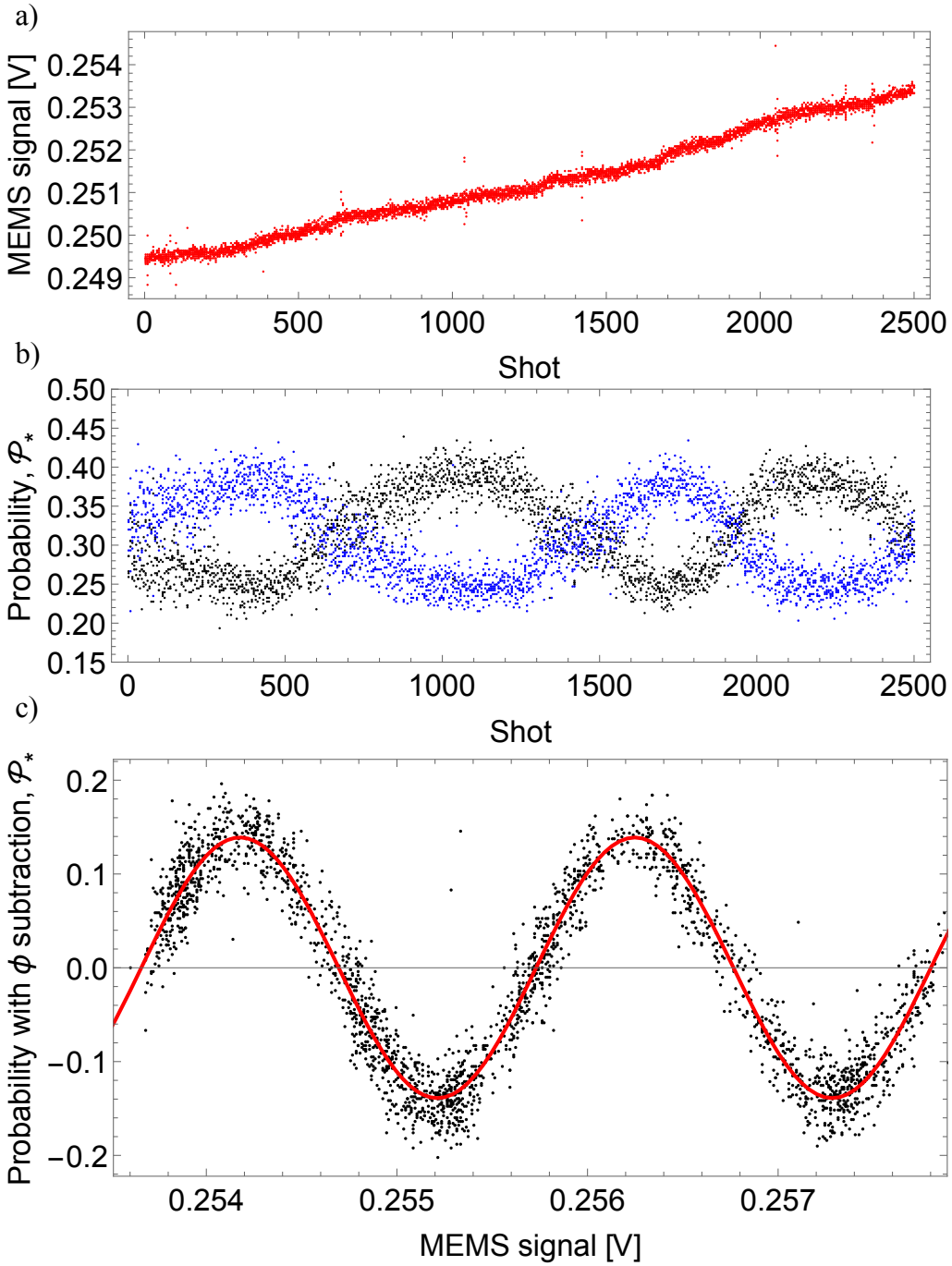

Figure 4.20: Atom interferometer correlation with MEMS accelerometer. a) MEMS voltage acquired during the run. The table is slowly tilting. b) The atom interferometer signal, fed some fixed $\phi_{\text{las}} = \phi_0$, flops between ϕ_0 (black) and $\phi_0 + \pi$ (blue), scanning fringe patterns as the table tilts. c) Correlating the atom interferometer and the MEMS. The red line is a fit to equation (4.9). This is data around midday. I have not removed any data points, evidenced by the occasional uncorrelated shot (all of which are from the laboratory door being slammed; the author notes, wryly, that other laboratory users fail to read clear signage/instruction when it doesn't involve their experiment).

where $\mathcal{P}_*$ is the probability $\mathcal{P}$ with the background suppressed through phase subtraction, β is the calibration factor in units of rad V^{-1}, and V_0 is the MEMS accelerometer offset voltage. I measure a fringe amplitude, peak to trough, of 0.26. I measure a value $\beta = 3044 \pm 12$ rad V^{-1}. This is not sufficiently precise for the primary experiment, see chapter 5, so I make another measurement where instead of letting the table tilting scan out a fringe pattern, I apply a series of lead weights to the table to see more fringes, see Fig. 4.21.

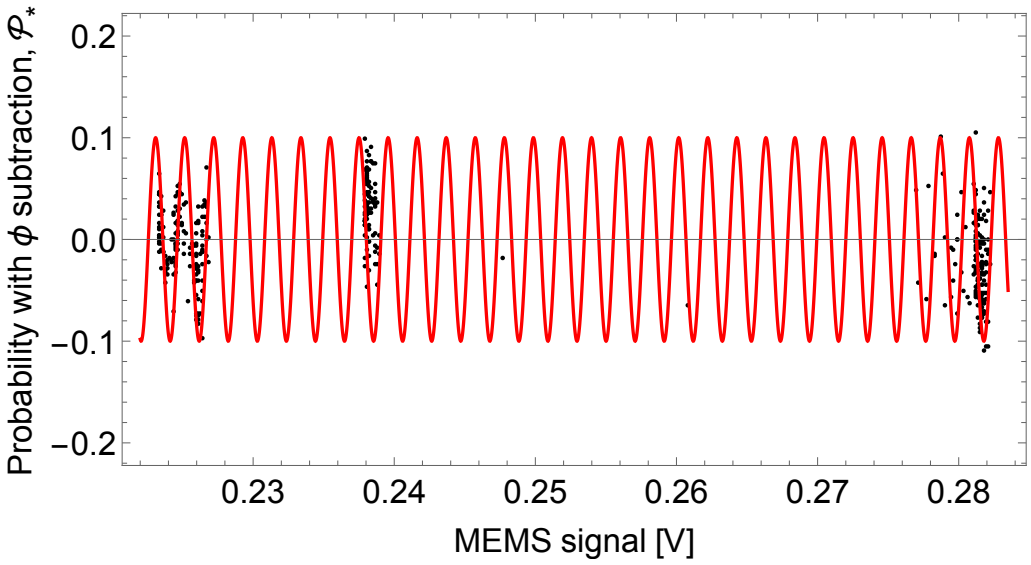

Figure 4.21: Big tilt trial. Data acquisition was begun with no weight and the table allowed to tilt freely. After some time, lead bricks were added to tilt table. After some time, the weights were removed and the table allowed to settle.

This measurement gives me the more precise value

$$\beta = 3051 \pm 2 \text{ rad/V}, \tag{4.10}$$

consistent with the last result and with a fractional error of 7 parts in 10^4. Knowing the atom interferometer fringes vary as

$$\mathcal{P}_* = A \cos\left(k_{\text{eff}} a T^2 + \phi_0\right), \tag{4.11}$$

I obtain the MEMS accelerometer calibration,

$$\frac{\mathrm{d}a}{\mathrm{d}V_{\text{MEMS}}} = \frac{\beta}{k_{\text{eff}} T^2}. \tag{4.12}$$

Here, I have

$$k_{\text{eff}} = \frac{2\pi}{c}(\nu_1 + \nu_2) \tag{4.13}$$

where c is the speed of light, ν_1 is the absolute frequency of laser 1, and ν_2 is the absolute frequency of laser 2. These frequencies are defined from the virtual level established -1.13 GHz below the $5^2S_{1/2}(F = 2) \rightarrow 5^2P_{3/2}(F = 3)$ transition:

$$\begin{aligned} \nu_1 &= 384.233820 \text{ THz } \pm \text{ 1 MHz} \\ \nu_2 &= 384.226985 \text{ THz } \pm \text{ 1 MHz,} \end{aligned} \tag{4.14}$$

where the error bar is from the reference laser lock point (lock-in amplifier fixed to the 2→3 crossover in Rb85, conservatively estimated good to 1 MHz). This gives a fractional error to a part in 10^9, small by comparison to the error in β.

The time of free propagation T, defined in chapter 2, is 16 ms. The error on the timing T is good to better than 1 ns; the timing is good to better than a few parts in 10^8. I know this from the error on the 300 MHz quartz oscillator (output clock frequency of 150 MHz) that times the FPGA; this functions as my pattern generator and system clock. Having used the atoms to calibrate the MEMS accelerometer, I obtain a calibration of

$$\xi = \frac{\beta}{k_{\text{eff}}T^2} = 0.7400 \pm .0005 \ \frac{\text{m s}^{-2}}{\text{V}}. \tag{4.15}$$

After building the experiment in chapter 3, here I have shown that I set up the interferometer experiment starting with co-propagating Raman beams and spectroscopy to an acceleration sensitive Kasevich-Chu atom interferometer. Further, I have calibrated a MEMS accelerometer on the back of the retro-reflector which I will use to separate environmental accelerations from anomalous accelerations.

Chapter 5

Primary experiment

5.1 Explanation of the experiment and the run pattern

The scientific aim of this thesis, to look for deviations from Newtonian gravity, was now possible with the conclusion of chapter 4. Here, I present the results of this experiment. First, I describe the experiment run pattern, where I explain which parameters were switched, how fast and why. Following this, I describe the data and the 36 independent datasets that comprise the result. This leads to a brief discussion of some of the systematics and limitations of the experiment. Last, I discuss how my result places constraints on theories of screened modified gravity.

The experiment strategy is shown in Fig. 5.1. The source mass can be placed in two positions, "Left" or "Right", defined in section 3.6. Viewed from the side, a) in Fig. 5.1, the source mass perturbs the scalar field from its background value ϕ_{bg}, which is determined by the chamber dimensions and the vacuum quality. I change the source mass position, changing the sign of the acceleration. The source mass does not block the raman beam, which can be seen more clearly when viewed from the top, b) in Fig. 5.1. It is also off axis, so I measure a projection of the force onto the Raman axis which I will treat in a section considering systematic corrections.

The experiment parameters are as previously established in the preceding chapter. In brief, starting with an ensemble of a few 10^6 atoms at 5 μK, all in the $|1,0\rangle$ ground state, I operate

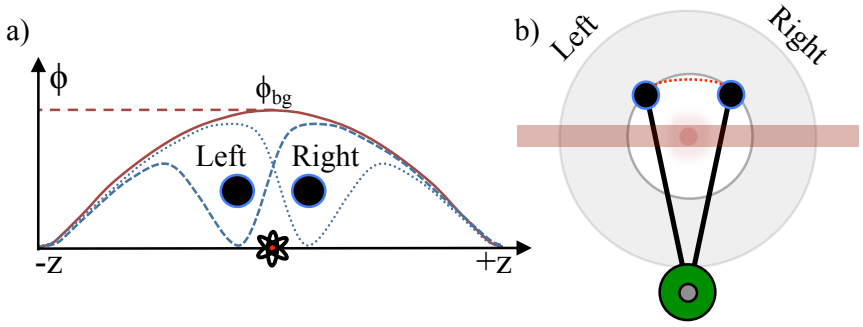

Figure 5.1: Experiment strategy. a) Perturbations induced by the presence of a source mass. The gradient direction changes with the switching of the source mass position. b) Top down view showing the source mass in relation to the atoms.

a Kasevich-Chu atom interferometer with 2T = 32 ms and pulse times $(\pi/2 - \pi - \pi/2) \rightarrow (2.05\ \mu s - 4.7\ \mu s - 3.2\ \mu s)$ at cm distances from a cm-sized source mass. I switch some parameters to mitigate the effects of drift [52, 53] and to suppress systematic errors, see Fig. 5.2. First, I switch the phase of the Raman beat note, on the third interferometer pulse, between ϕ_0 and $\phi_0 + \pi$ (see section 4.2.3). Second, I switch the source mass between the positions "Left" and "Right", see Fig. 5.1. Last, I flop the direction of the applied magnetic field. This was a precautionary measure; I will show there was no measured effect. A full experiment pattern requires 16 shots, shown in time order in Fig. 5.2.

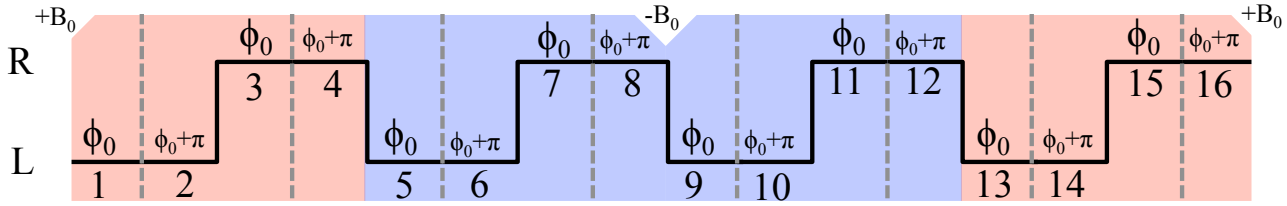

Figure 5.2: Experiment run pattern. A total of 16 shots make a single run pattern. The phase of the Raman beat note applied to the third pulse is changed every shot between ϕ_0 and $\phi_0 + \pi$. The source mass changes position every two shots. The magnetic field is switched, as a precaution, in a more complicated pattern; the first 4 shots are $+B_0$, the next 8 shots are $-B_0$, and the last four are $+B_0$. Each shot took 1.2 seconds, limited by the loading time of MOT. There was a dead time of about 1 second related to pattern generation and moving the source mass; the time between shots was 2.2 seconds.

A summary of how the measurement works helps dissect the run pattern. The atom interferometer has two outputs:

$$N_1 = A \sin^2 [\Phi/2] \text{ and } N_2 = A \cos^2 [\Phi/2], \tag{5.1}$$

where $\Phi = k_{\text{eff}} a T^2$ is the total phase difference along the two interferometer paths and A is the amplitude of the fringe pattern. I can rewrite these outputs as

$$N_2 = \frac{A}{2}(1 - \cos[\Phi]) \text{ and } N_1 = \frac{A}{2}(1 + \cos[\Phi]). \tag{5.2}$$

I introduce an additional contribution to Φ by changing the phase of the Raman beat note just before application of the third pulse. I apply a π phase flip, changing the fringe pattern to

$$N_2 = \frac{A}{2}(1 + \cos[\Phi]) \text{ and } N_1 = \frac{A}{2}(1 - \cos[\Phi]). \tag{5.3}$$

The experiment uses the photodetector voltage to measure N_2 and $N_{\text{tot}} = N_2 + N_1$ with their respective backgrounds,

$$V_2 = q(N_2 + b_2) \text{ and } V_{\text{tot}} = q(N_{\text{tot}} + b_{\text{tot}}), \tag{5.4}$$

where q converts voltage to atom number and $q\ b$ is the background light. The ratio of these voltages is

$$\mathcal{P} = \frac{V_2}{V_{\text{tot}}} = \frac{q(N_2 + b_2)}{q(N_{\text{tot}} + b_{\text{tot}})} = \frac{N_2 + b_2}{N_{\text{tot}} + b_{\text{tot}}}. \tag{5.5}$$

From equations (5.2) and (5.3), I have

$$\mathcal{P}_{\substack{\pi \\ 0}} = \frac{\frac{A}{2}\big(1 \pm \cos(\Phi)\big) + b_2}{A + b_{\text{tot}}}, \tag{5.6}$$

where the sign is determined by the phase shift (0 or π) applied on the third laser pulse. I take the difference:

$$\mathcal{P}_* = \mathcal{P}_\pi - \mathcal{P}_0 = \Big(\frac{A}{A + b_{\text{tot}}}\Big)\cos(\Phi) = C\cos(\Phi). \tag{5.7}$$

This is a fringe symmetrical around $\mathcal{P}_* = 0$ with an amplitude dependent upon the background. It might seem natural to subtract the background before constructing the ratio $\mathcal{P}$; I found empirically that this subtraction adds unwanted noise. Since a background-dependent amplitude does not compromise the measurement, I refrain from subtracting the background. For each pair of time bins in Fig. 5.2, I subtract the $\phi_0 + \pi$ interferometer signal from the ϕ_0 signal to

give a value of $\mathcal{P}_*$; I average the corresponding MEMS accelerometer signals.

The experiment runs with the source mass in either the "Left" or "Right" position. Switching the position will change the sign of the attractive force between the atom cloud and the source mass, resulting in an acceleration $\pm a_{\text{ball}}$. It may also change the acceleration due to the tilting of the table between $a_0 \pm \delta g$. I expect a $\mathcal{P}_*^L$,

$$\mathcal{P}_*^L = C_L \cos(\Phi_L), \tag{5.8}$$

where $\Phi_L = k_{\text{eff}} T^2 (a_0 + \delta g + a_{\text{ball}})$, and similarly a $\mathcal{P}_*^R$,

$$\mathcal{P}_*^R = C_R \cos(\Phi_R), \tag{5.9}$$

where $\Phi_R = k_{\text{eff}} T^2 (a_0 - \delta g - a_{\text{ball}})$. Here, δg allows for the possibility that the table may tilt when the source mass moves. Critically, the MEMS accelerometer measures δg but not a_{ball}, allowing me to separate δg from a_{ball}. If the calibration of the MEMS accelerometer voltage were inaccurate, there could be a residual systematic error as the method would not fully remove δg. I investigate this in the next section and find the calibration is good enough to avoid such an error.

Equations (5.8) and (5.9) can be re-written as

$$\begin{aligned} \mathcal{P}_*^R(V_M^R) &= C_R \cos\Big(\beta(V_M^R - V_{\text{bias}} - V_{\text{ball}})\Big), \\ \mathcal{P}_*^L(V_M^L) &= C_L \cos\Big(\beta(V_M^L - V_{\text{bias}} + V_{\text{ball}})\Big), \end{aligned} \tag{5.10}$$

where β converts voltage to phase, V_M^L (V_M^R) is the MEMS voltage for when the source mass is in the left (right) position, V_{bias} accounts for the tilt of the table as well as offset bias and V_{ball} is the offset associated with a_{ball}. By fitting the left (right)-position fringe pattern as a function of V_M^L (V_M^R), I distinguish the acceleration of interest, a_{ball}, from the uninteresting δg. Last, I switched the sign of the applied magnetic field, so $B_\pm = \pm 1.685$ G, just to check that this did not reveal any systematic effect.

To summarize, the run pattern has three modulations, each with its own orthogonal switching pattern. First, the applied laser phase ϕ_0 is changed between ϕ_0 and $\phi_0+\pi$ every shot (every 2.2 s). I take the difference, allowing me to suppress backgrounds and amplitude fluctuations. Next, I change the source mass position every two shots (4.4 s), the primary experiment. Finally, I changed the sign of the applied magnetic field.

5.2 The primary result

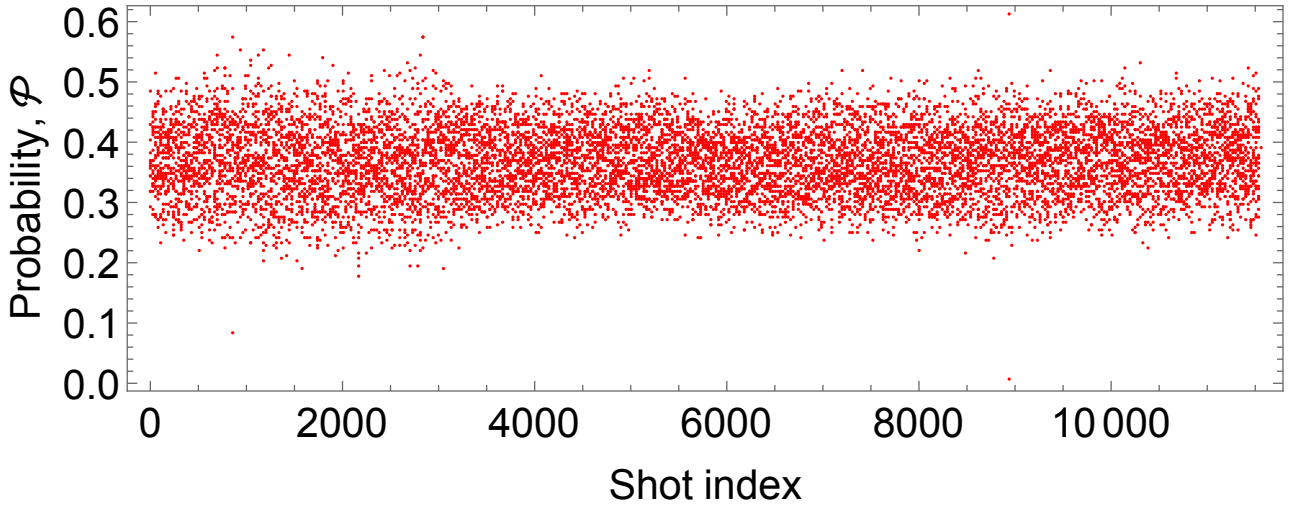

Figure 5.3: Raw data from one run of the primary experiment. The only data processing performed here was to create the probability $\mathcal{P}$, see equation (3.13), and to remove shots when a laser unlocked.

The apparatus was set to take data in multiples of 12000 shots. Fig. 5.3 shows the values of $\mathcal{P}$ measured in a typical run. These 12000 data points constitute 1500 run patterns giving 750 values for $\{V_M^L, P_*^L\}$ and 750 values for $\{V_M^R, P_*^R\}$. Half of these values have the applied magnetic field B_+ and the other half B_-.

Fig. 5.4 shows the $\mathcal{P}_*^L(V_M^L)$ and $\mathcal{P}_*^R(V_M^R)$ obtained from the data in Fig. 5.3. Please note, for display purposes in Fig. 5.4, I have inverted the sign of the "left" points so that they can be distinguished from the "right" points. Further, for ease of comparison to the fit, I have binned the data in bins of 135 μV. Without this last step, the data resembles that of Fig. 4.20. The

fit is to the data, before binning. I fit each fringe to the equation

$$\mathcal{P}_{\rm fit}^{L,R} = C\cos\Big(\beta\big(V_M^{L,R} + V_0^{L,R}\big)\Big), \tag{5.11}$$

where C is the same for both source mass positions. Here, $V_0^{L,R} = V_{\rm bias} \pm V_{\rm ball}$ so $a_{\rm ball} = \frac{\xi}{2}(V_0^L - V_0^R)$, where ξ is defined in equation (4.15). I acquired 36 datasets like Fig. 5.4, from which I obtain the values of V_0^L and V_0^R, see column 2 and 3 of Table 5.1. The mean of the left V_L^0 and right V_R^0 voltages, column 4, corresponds to the offset voltage $V_{\rm bias}$ of the MEMS accelerometer, as shown in equation (5.11). The value of $V_{\rm ball}$ is given in column 5. The variation in the bias is very large, the standard deviation is 299 μV, compared with the value of $V_{\rm ball}$. This bias variation corresponds to a bias noise of 221 μm s^{-2}, where I have used the conversion ξ. The data sheet for the MEMS accelerometer (Honeywell QA-750) specifies a bias change of < 60 μg/°C; the standard deviation I observe in $V_{\rm bias}$ is consistent with a standard deviation in the laboratory temperature of order 1/2°C. The heating, ventilation, and air conditioning system for this experiment is rated for temperature variations up to 2 °C, but the temperature logs report a standard deviation in the laboratory temperature consistent with the bias change of the measured MEMS accelerometer bias change, about 1/2°C. The author and his advisor note, for posterity, that the Honeywell QA750 MEMS accelerometer has performed admirably as the world's most elaborate thermometer.

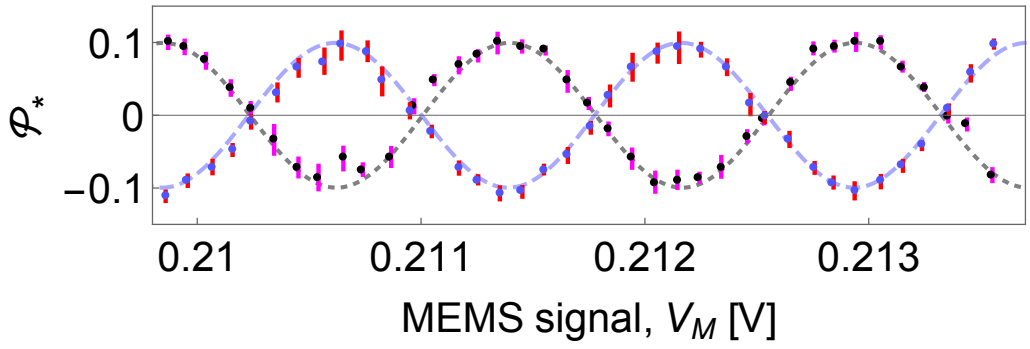

Figure 5.4: Sample of primary experiment data. Data taken in the "right" source mass position is denoted by the black diamonds and the "left" position by the lavender triangles. Taken over about 12 hours, this set is typical of the fringe patterns. The noise is reduced here by binning; Fig. 4.20, a similar dataset bar the binning, displays this noise. This pattern began on the left, near $V_M = 0.21$ V. Over the course of the measurement, the table tilted toward $V_M = 0.214$ V.

Table 5.1: MEMS accelerometer voltages for the primary experiment.

Run	V_0^L [μV]	V_0^R [μV]	$\frac{1}{2}\left({V_0}^R + {V_0}^L\right)$ [μV]	$\frac{1}{2}\left({V_0}^R - {V_0}^L\right)$ [μV]
1	88.427	90.419	89.423	-0.996± 0.931
2	-225.172	-228.175	-226.674	1.501±1.650
3	174.98	172.551	173.766	1.215 ±0.899
4	-387.892	-387.626	-387.759	-0.133±0.696
5	-263.586	-264.139	-263.862	0.276 ±0.929
6	482.588	480.665	481.627	0.962±1.362
7	-224.137	-222.523	-223.33	-0.807±1.400
8	-138.433	-132.999	-135.716	-2.717±1.489
9	245.717	244.479	245.098	0.619± 1.354
10	453.448	453.587	453.517	-0.069±1.267
11	-245.572	-246.986	-246.279	0.707±1.241
12	425.547	425.068	425.308	0.239 ±0.677
13	-399.578	-400.224	-399.901	0.323±1.179
14	-97.296	-92.783	-95.0395	-2.257±1.047
15	-420.431	-421.344	-420.888	0.456±2.171
16	278.323	279.585	278.954	-0.631±1.094
17	185.738	186.466	186.102	-0.364 ±1.054
18	571.298	570.71	571.004	0.294 ± 0.656
19	30.218	28.745	29.482	0.736±0.785
20	-329.507	-328.537	-329.022	-0.485±0.967
21	125.525	128.913	127.219	-1.694±0.895
22	-128.808	-131.236	-130.022	1.214±1.259
23	80.814	80.044	80.429	0.385±1.434
24	67.671	66.125	66.8982	0.773±1.953
25	234.78	231.159	232.969	1.810±1.874
26	-156.536	-153.57	-155.053	-1.483± 0.783
27	193.041	195.936	194.489	-1.447±0.492
28	435.774	432.925	434.349	1.425 ±0.732
29	616.171	617.848	617.009	-0.838± 0.699
30	279.021	283.67	281.346	-2.324± 0.498
31	-378.129	-376.76	-377.444	-0.684± 0.434
32	393.232	392.377	392.805	0.428± 0.508
33	243.155	243.876	243.516	-0.360± 0.516
34	343.014	346.5	344.757	-1.743± 1.161
35	177.633	178.189	177.911	-0.278± 1.340
36	236.898	237.225	237.062	-0.164± 1.697

Throughout all datasets, the most stable in terms of table wallowing covered only half a fringe while the least stable covered 10 fringes. Not all datasets contain 12000 shots; various conditions led some sets to be stopped early or to significant cuts being made. Some issues were as simple as lasers unlocking due to a change of lab temperature. Set 7 through 15 were high vibration tests where I slipped paper dampeners underneath various table legs in an attempt to reduce table wallowing while increasing vibrations. There was no evident change in the quality of the data, which showed the MEMS accelerometer was effective at removing the vibration noise. Set 26 through set 33 were full sets with minimal cuts.

For each of the 36 measurements I determine $V_{\text{ball}} = (V_0^R - V_0^L)/2$, shown in column 5 of Table 5.1. These have a weighted mean and standard error of

$$V_{\text{ball}} = +28 \pm 193 \text{ nV}. \tag{5.12}$$

After multiplying by ξ, given in equation (4.15), this gives

$$a_{\text{ball}} = +20 \pm 143_{\text{stat}} \text{ nm s}^{-2}. \tag{5.13}$$

I plot the individual values of a_{ball} in Fig. 5.5. Next, I interpret the sign of a_{ball} as indicating an attractive force. I follow this with a discussion of systematic corrections and uncertainties before stating the result for a_χ.

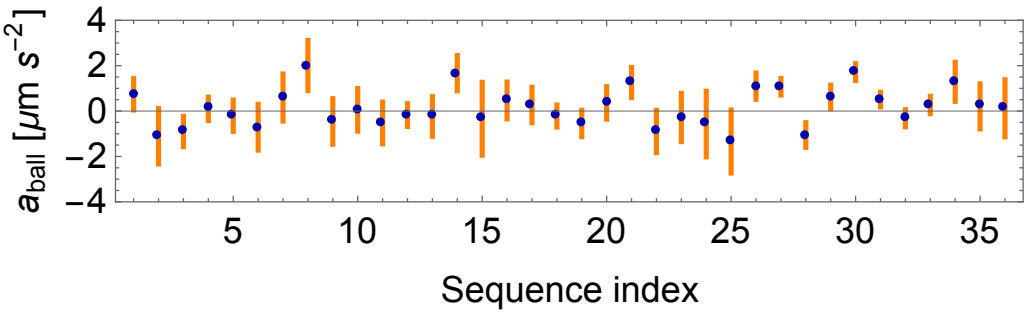

Figure 5.5: Determining a_{ball}. Here are the 36 independent measurements of a_{ball}. The mean and standard error of these values is given in equation (5.13). The gray line is through $a_{\text{ball}} = 0$ μm s^{-2}, for reference.

Determination of an attractive or repulsive result

Before I can apply systematic corrections and interpret my result, I must be clear on whether my result, a_{ball}, is an attractive or repulsive force. I use the correlation between the sign of the MEMS accelerometer voltage and the MEMS orientation, see Fig. 3.16, to determine the attractive or repulsive nature. When oriented like vi) in b) of 3.16, parallel with the force of gravity, I measure a positive voltage much larger than any possible bias error. With the MEMS accelerometer attached to the mirror, see vii) of b) in Fig. 3.16, I measure strictly positive voltages through all measured tilt angles of the experiment. The table is *always* tilted such the MEMS accelerometer measures a small component along gravity, strictly positive voltages $V_M^{L,R}$. This means a positive voltage is a force whose direction goes from "Left" to "Right", see Fig. 3.17. I performed a simple check by placing weights on the "right" side of the optical table, which made the MEMS accelerometer voltage more positive. If the force is attractive, I expect V_0^R to be a larger positive voltage than V_0^L, which is to say I expect an attractive force to produce a positive voltage for $V_0^R - V_0^L$. The mean of column 5 in Table 5.1, equation (5.12), is a positive voltage. I have measured an attractive force.

Systematic corrections

There are two systematic corrections I need to apply to the value of a_{ball}, equation (5.13). First, the a_{ball} I have measured is the component of the whole acceleration toward the source mass, projected onto the Raman beam axis. I must divide my result by $\cos(\theta)$, where $\theta = 48.8$ Deg is the angle between the line linking the center of the atom cloud and the source mass and a line through the center of the atom cloud and parallel to Raman beam axis, see section 3.6. Second, I must remove the contribution of the normal Newtonian gravitational acceleration between the atom cloud and the source mass from a_{ball}. The atom cloud has a center of mass velocity of 3 cm/s along the Raman beam, toward the "left" position. They fall under gravity from their starting point. The distance d, see a) in Fig. 3.17, from the center of the atom cloud to the center of the source mass, after following the trajectory for $2T = 32$ ms, is 30.1 mm in the case of the "right" position and 28.9 mm for the "left" position; this position difference is sufficiently

small as to not require a separate treatment of the gravitational acceleration of the two mass positions. The cloud expands during the interferometer time $2T = 32$ ms. Some atoms move closer to the mass and some further away. I measure the acceleration averaged over the cloud; the force over a spherical cloud is the same as the force on an atom at the centre of the cloud, in that the gravitational attraction to a sphere is as though the mass is all concentrated at the center. Knowing this, I can state the Newtonian gravitational acceleration due to the presence of the source mass as $a_{\mathrm{g}} = +7$ nm s^{-2} for both positions, where the sign is from determining whether the force is attractive or repulsive. Having determined that an attractive force is a positive voltage, I subtract this gravitational acceleration from a_{ball}. Applying both of these corrections to my result, I obtain

$$a_{\chi} = \frac{a_{\mathrm{ball}}}{\cos(\theta)} - a_{\mathrm{g}} = +24 \pm 210 \text{ nm s}^{-2}, \tag{5.14}$$

the anomalous acceleration between the source mass and the atomic cloud.

Systematic uncertainties

Here, I discuss systematic uncertainties in this experiment. I measure the change of interferometer phase when the source mass moves from "left" to "right". Aside from the effect of the Newtonian attraction and the proposed scalar field, there is also the possibility of an interferometer phase shift if the table tilts when the source mass is moved. This has been anticipated in the way the experiment is performed in that I remove this contribution δg with the MEMS accelerometer. The movement of the source mass could produce real or apparent phase shifts through other mechanisms - these potential systemic errors are considered here.

Magnetic field gradients from the source mass do not accelerate the atom when it is in the superposition $|1,0\rangle + e^{i\phi}|2,0\rangle$, but can create a systematic error as described in Appendix A. Movement of the atoms through a magnetic field gradient creates a phase shift in the

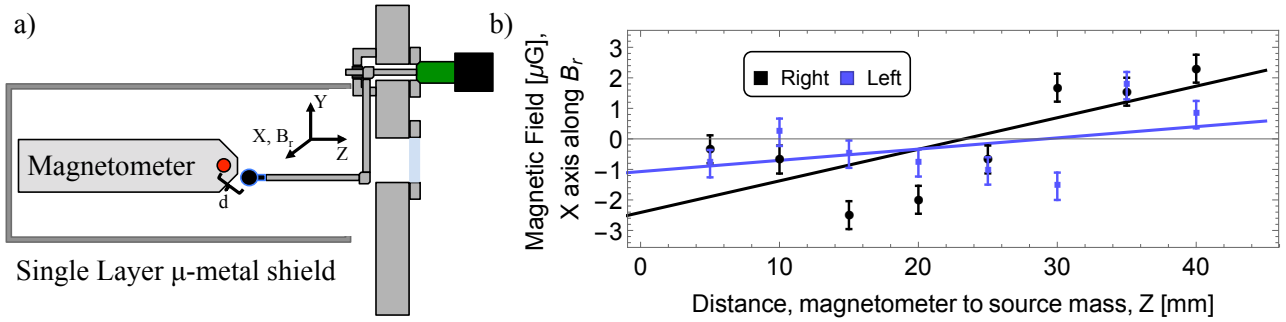

Figure 5.6: Source mass magnetism test. a) Schematic of the experiment to measure magnetic fields produced by the source mass. The axis labeling is for the 3 axes of the magnetometer. b) Magnetic field near the source mass versus distance of the source mass from the magnetometer. I moved the source mass assembly along the Z axis, measuring the X axis which I identify as the axis of B_r. I assume a linear magnetic field gradient and fit to the data.

interferometer, which looks like an acceleration. This phase shift is

$$\delta\phi = 4\pi\alpha_B B_0 \vec{\nabla} B \cdot \vec{a}\, T^3, \tag{5.15}$$

where B_0 is the magnitude of the magnetic field, $\vec{\nabla}B$ is its gradient, $\vec{a} = -g\ \hat{z}$ in my case, $\hat{z}$ is the vertical direction, T is the interferometer time, and $\alpha_B = 575.15$ Hz G^{-2} is the change in the frequency of the clock transition $|1,0\rangle \leftrightarrow |2,0\rangle$ (divided by B^2). This phase shift looks like an acceleration

$$\delta a = -\alpha_B B_0 \frac{\partial B_\mathrm{r}}{\partial z} g\lambda T, \tag{5.16}$$

where B_r is the magnetic field component along the Raman axis, and λ is the wavelength. I want this fake acceleration to be small; to control this to 100 nm s^{-2}, the field gradient must be ≤ 8.4 μG/cm. I tested the magnetic field and field gradient from the source mass. I placed a 3-axis flux-gate magnetometer (Bartington Instruments, MAG-03MC1000) in a fixed position inside of a cylindrical magnetic shield made of a single layer of μ-metal. The source mass assembly, all components i) through iv) of a) in Fig. 3.17, was positioned such that the X axis of the magnetometer directly measured the magnetic field component along the Raman axis B_r, see a) of Fig. 5.6. I use a 6.5 digit multimeter (Keysight 34461A) to log the voltage from the magnetometer. The magnetometer demonstrates a resolution of 0.2 μG. Starting with the magnetometer near the source mass surface, I moved the source mass assembly 40 mm down the Z axis of the magnetometer while measuring the X axis, see b) of Fig. 5.6. This is a

measurement of the field gradient; I approximate the field gradient as linear and fit to the data from the magnetometer. I obtain a field gradient of 1.0 ± 0.4 μG/cm for the "right" position and 0.4 ± 0.3 μG/cm for the "left"; my experiment is sensitive to the difference between the positions, $\delta a \sim \frac{1}{2}\left(\frac{\partial B_r^R}{\partial z} - \frac{\partial B_r^L}{\partial z}\right)$. This corresponds to a false acceleration $+4 \pm 3$ nm s^{-2}, note the positive sign from "right" - "left" makes for an attractive acceleration. I conclude the source mass makes negligible contributions to the systematic uncertainty due to the second-order Zeeman effect.

An electric field gradient would accelerate the atoms by

$$\delta a_{E'} = \alpha_E E' E_0 / m, \tag{5.17}$$

where α_E is the ground state DC polarizability, and m is the mass of a ^{87}Rb atom. The aluminum source mass is electrically grounded to the same potential as the vacuum chamber. However, aluminum forms a stable oxide layer upon exposure to air, called alumina (Al_2O_3), that is ∼4 nm thick. This makes it possible for the surface of the layer to become charged. The alumina film breaks down at electric fields above a few MV/cm, so the source mass cannot hold potentials more than ∼ 1 V. With the atoms placed 27 mm from the center of the source mass (of radius 19 mm), and the source mass charged up to 1V, this acceleration is 2 nm s^{-2}. This is small enough to neglect.

There is an electric analogue to the false acceleration given by equation (5.16), caused by the (changing) Stark shift of the clock transition, which goes like kE^2. I replace α_B is equation (5.16) with the Stark shift coefficient $k = -1.23 \times 10^{-10}$ Hz/(V/m)^2 [54]; this coefficient shows the clock transition is exceedingly insensitive to electric fields, making this effect much smaller than the second-order Zeeman shift. For the electric field previously considered, the electric analogue to equation (5.16) produces false accelerations below 1 nm s^{-2}. This shift can be dismissed.

If the calibration of the MEMS accelerometer voltage were inaccurate, there could be a residual systematic error as the method would not fully remove δg. To ensure this was not a problem

for my experiment, I measured $\langle V_M^R - V_M^L \rangle$ of the data. I obtain $\langle V_M^R - V_M^L \rangle = -6.615\ \mu$V. Therefore,

$$\delta g = \frac{\xi}{2}\langle V_M^R - V_M^L \rangle = -2.447 \pm 0.002\ \mu\text{m s}^{-2}, \tag{5.18}$$

where the error bar is from the uncertainty in the calibration ξ. The calibration is good enough to avoid such an error, as the uncertainty in the determination of δg is negligible.

Last, related to the switching of all waveforms in Fig. 5.2, I wanted to investigate the possibility of a systematic error arising from a correlation between the MEMS accelerometer voltage and the phase switching of the beat note between the Raman lasers. Such a correlation could produce a false acceleration a_χ; this problem of unwanted crosstalk, see section 6.1 of [55], is well studied. I performed a simple test of the MEMS accelerometer acquisition channel where I switched the phase of the Raman beat note between $\phi_0 + \pi$ and ϕ_0 while monitoring the MEMS accelerometer voltage for a switch dependent shift. I find that the mean shift due to switching of the Raman beat note phase is $\langle V_M^{\pi-0} \rangle \leq 0.4 \pm 1$ nV. Using the calibration ξ, this corresponds to an acceleration 0.3 ± 0.7 nm s^{-2}. This is negligible.

Noise from the background

I found that the background subtraction adds noise to the data. This is due to low voltage signal from the small atom numbers used in the experiment, a consequence of the lossy state and velocity selection technique I employ, see Fig. 4.7. I allude to this problem in my treatment of equations (5.4) to (5.7), where I conclude that without background removal, the amplitude of the fringe pattern becomes a function of the background. The data displayed in Fig. 5.4 and all the datasets in Fig. 5.5 have the background included. I record the background voltage b_{tot} of every shot in a measurement and found that it is constant over the duration of every measurement, so the fringe amplitude did not vary. That is important as one could imagine a systematic variation of amplitude might produce a systematic error in the measurement. Clearly, it would be desirable to have a more efficient optical pumping scheme, in which case it may make sense to reintroduce the background subtraction.

Conclusions about a_χ

First, and before discussion of how my result applies to the scalar fields discussed in chapter 2, I must set an upper bound for my result. Having considered the systematic uncertainties above, I arrive at the result $a_\chi = +16 \pm 4_{\text{syst}} \pm 210_{\text{stat}}$ nm s^{-2}. I can say, with 90% confidence that $a_\chi < +285$ nm s^{-2}, where the positive sign means an attractive acceleration. I take this as my upper limit.

5.3 Constraints on Chameleon Gravity

I seek to apply my result to one of the central mysteries of cosmology - dark energy. I focus on the chameleon gravity discussed in chapter 2. I ended my discussion on the origin of the proposed anomalous acceleration with equation (2.22). There, I give the acceleration a_χ of the atom toward the center of the source mass. I will now use this expression for a_χ, together with my experimental upper limit, to constrain the parameters Λ, the field self-coupling, and M, the field coupling to matter. First I will restate equation (2.22) in a slightly different form for ease of discussion:

$$a_\chi = \lambda_1 \lambda_2 \frac{\rho_1 R_1^3}{3M^2 r^2}, \tag{5.19}$$

where ρ_1 is the density of the source mass. Here, I have replaced the Planck mass $M_{\text{Pl}} = 1/\sqrt{8\pi G}$, the mass of source $m_1 = \frac{4}{3}\pi R_1^3 \rho_1$. The parameter λ_1, for the source mass and given by equation (2.23), is equal to $3M\phi_{\text{bg}}/(\rho_1 R_1^2)$ up to a maximum value of one. Here, ϕ_{bg} is the value of the field far from the source mass, which I take as the value near the center of the empty vacuum can. Similarly, λ_2, for the test mass - the atom - is characterized by $3M\phi_{\text{bg}}/(\rho_2 R_2^2)$ up to a maximum value of one. I must first evaluate ϕ_{bg} to find the functional relationship between Λ, M, and a_χ.

Determining ϕ_{bg}

Simply put, the background field ϕ_{bg} has two regimes: the first being where ϕ_{bg} is dominated by the background pressure inside the vacuum can, parameterized by the residual background pressure ρ of H_2, and a second where ϕ_{bg} is limited by the dimensions of the can, parameterized by the radius L.

The density of the wall of the vacuum can is high, so the scalar field has a low value. The density of background gas ρ inside the vacuum can is much lower than the density of the walls, so ϕ_{bg} has a higher equilibrium value. The field ϕ_{bg} can, however, be less than that if the size L of the vacuum can does not allow sufficient room for the field to become that large. Burrage *et. al.* [3] have shown that

$$\phi_{bg} = 0.69\sqrt[3]{\Lambda^5 L^2} \tag{5.20}$$

at the center of an evacuated spherical vacuum vessel, where L is the radius of the vacuum can. I can conclude then that ϕ_{bg} is size-limited if $0.69\sqrt[3]{\Lambda^5 L^2} < \sqrt{\Lambda^5 M/\rho}$, which I rewrite as

$$\Lambda^5\left(\frac{M}{M_{Pl}}\right)^3 > (0.69)^6 L^4 \rho^3 / M_{Pl}^3. \tag{5.21}$$

To determine whether ϕ_{bg} is pressure or size limited, I must establish what ρ and L are for my system.

The pressure, according to the ion pump current, is 4.4×10^{-10} mbar, calibrated to nitrogen; see xii) in b) of Fig. 3.1 for the placement of the ion pump. To adjust to the corresponding pressure of hydrogen, this value needs to be divided by 0.46 [56]; so a pressure of 9.6×10^{-10} mbar. This pressure corresponds to a mass density of $\rho = 8.6 \times 10^{-14}$ kg/m^3 or 3.7×10^{-34} GeV^4 (see Appendix B for conversion from SI units to GeV).

The open volume in my experiment is not spherical; there is no analytical form for ϕ_{bg} in my case. However, ϕ_{bg} will not be smaller than that of a sphere inscribed within my vacuum can that just touches the MOT electromagnet formers, as shown in a) in Fig. 5.7, where $L = 6.5$ cm or 3.3×10^{14} GeV^{-1}. I would expect ϕ_{bg} to be larger than this and $L = 8$ cm or 4.1×10^{14}

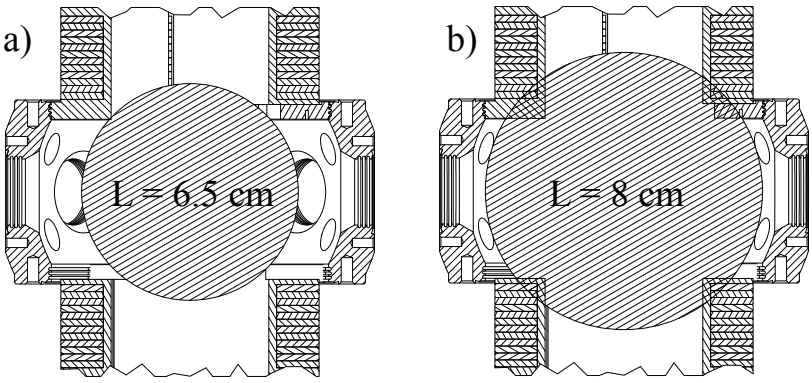

Figure 5.7: Size limit for size parameter L. a) a sphere with an open volume defined by $L = 6.5$ cm, where no mass is present other than the atoms and source mass. b) a larger volume defined by $L = 8$ cm.

GeV^{-1} is a more reasonable choice of L. The radius of the spherical octagon is 9 cm. Taking $L = 6.5$ and 8 cm together with the mass density ρ of the background gas, I now know that $(0.69)^6 L^4 \rho^3 / M_{\rm Pl}^3$ is between 0.5×10^{-98} and 1.6×10^{-98} GeV^5.

In Fig. 5.8, I show contours of $\phi_{\rm bg}$ as a function of Λ and M, taking $L = 8$ cm. I use the range of Λ and M established in Burrage *et al* [3]: from the observed accelerating expansion of the universe, Λ is expected to be of order 1 meV, so I take the range $10^{-2} < \Lambda < 10^2$ meV. M, however, is much less constrained. A lower bound of 10^4 GeV is established by the measured $1S - 2S$ transition in hydrogen [57–59]. A lack of clarity about physics above the Planck scale creates an upper bound defined by the reduced Planck mass, $M_{\rm Pl} \approx 2 \times 10^{18}$ GeV. The dashed red line, b), shows the boundary between the pressure-limited and size-limited regime. The dotted orange line, a), shows where this boundary would be for $L = 6.5$ cm. Note that, with this wide parameter space, it makes little difference whether I take $L = 6.5$ cm or 8 cm. With the value of $\phi_{\rm bg}$ established, I am ready to determine λ_1 and λ_2, the screening factors of the source mass and the atom respectively.

Screening of the source mass, λ_1

Up to a maximum value of one, the screening factors λ_i are given by $\lambda_i = \frac{3M}{\rho_i R_i^2}\phi_{\rm bg}$, see equation (2.23). Starting with the the size-limited regime for $\phi_{\rm bg}$, and knowing that $R_1 = 19$ mm and

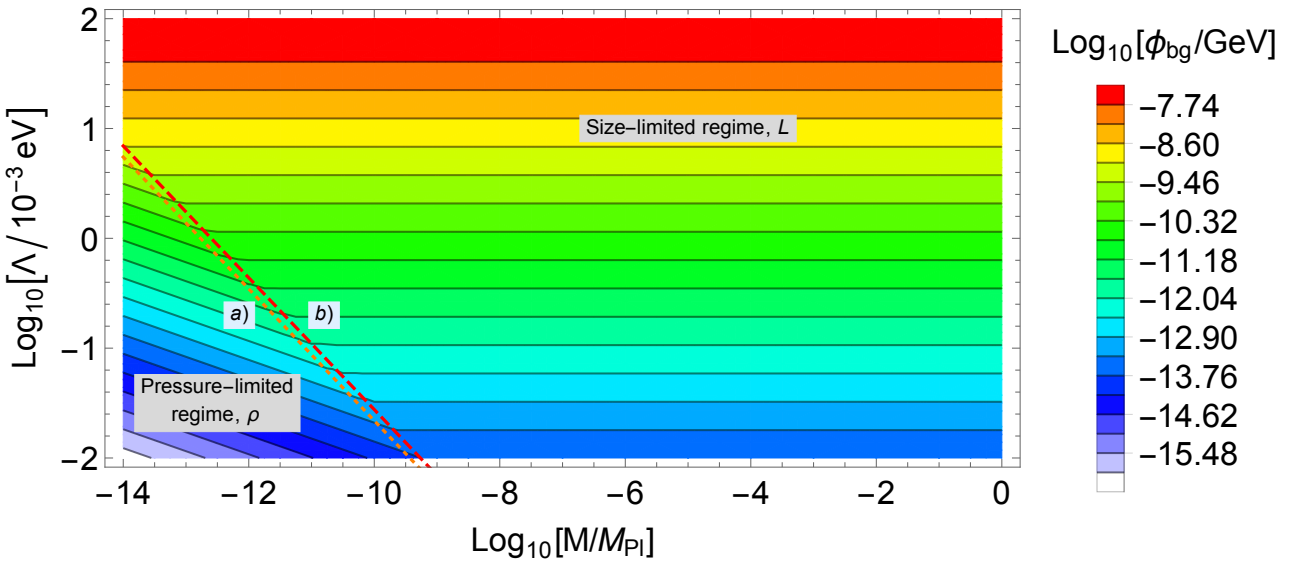

Figure 5.8: Contour plot showing the size-limited regime versus pressure-limited regime for $\phi_{\rm bg}$. This is the field at the center of my spherical vacuum chamber as a function of Λ and M. In the bottom left corner of the plot, $\phi_{\rm bg}$ is limited to $\sqrt{\Lambda^5 M/\rho}$ by the residual gas pressure, here taken to be 9.6×10^{-10} mbar of hydrogen (H_2). Outside of that corner, $\phi_{\rm bg}$ is limited by the size of the vacuum can to $0.69\sqrt[3]{\Lambda^5 L^2}$. a) This boundary, orange and dotted, is for $L = 6.5$ cm. b) For $L = 8$ cm, red and dashed. The boundary shift is negligible by comparison to the open parameter space.

$\rho_1 = 2700$ kg/m^3 for the aluminum source mass, I find

$$\lambda_1 = 2.6 \times 10^{17} \Lambda^{5/3} (M/M_{\rm Pl}), \tag{5.22}$$

where Λ is in GeV. The blue line in the upper right hand corner of Fig. 5.9 is where $\lambda_1 = 1$; over nearly all this parameter space, $\lambda_1 < 1$. This is often referred to as a screened source mass in the literature [3]. The entire pressure-limited regime is contained below the line $\lambda_1 = 1$.

Screening of the atoms, λ_2

The atom is composed of two parts, the electron cloud and the nucleus. Neither part is uniformly dense, but it is useful to note that $3M/\rho_2 R_2^2$ for a uniformly dense sphere of mass m_2 simplifies to $4\pi M R_2/m_2$. The nuclear mass of ^{87}Rb is ~ 4300 times larger than that of the electrons and the nuclear radius is ~ 10000 times smaller so it is the nucleus that limits $\lambda_2 < 1$.

I show $\lambda_2 = 1$ as the black line in Fig. 5.9, where I have estimated the nuclear radius of a ^{87}Rb

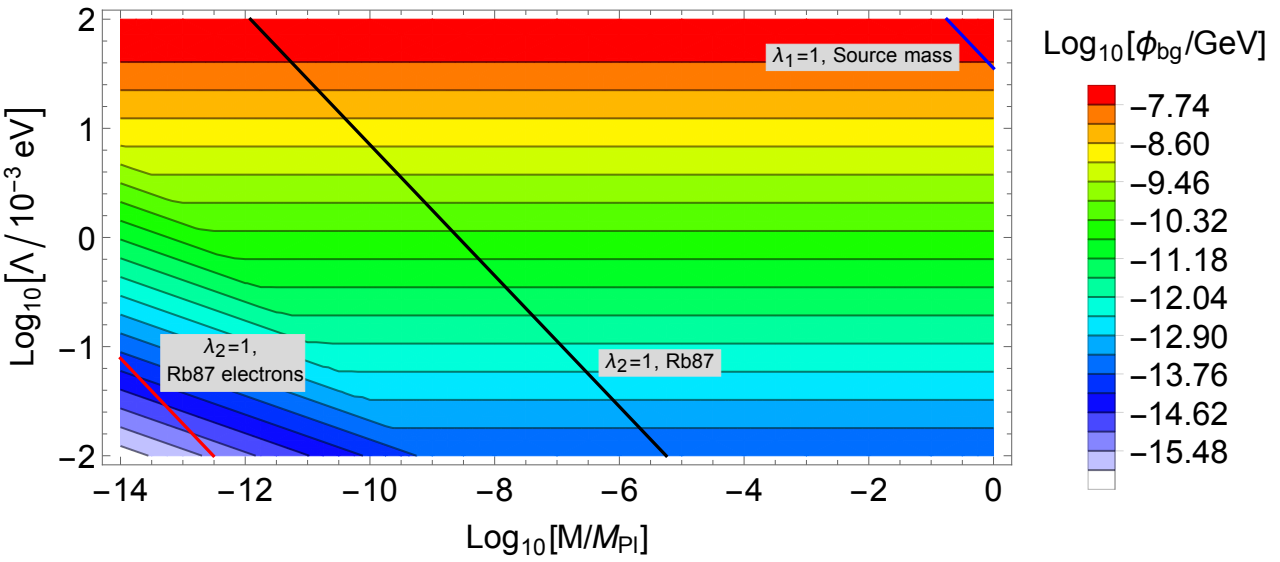

Figure 5.9: Contour plot showing $\phi_{\rm bg}$ and the screening regimes of λ_1, λ_2. The blue line shows $\lambda_1 = 1$. The black line displays $\lambda_2 = 2$ when considering the entire ^{87}Rb atom. The red line is $\lambda_2 = 1$ when considering only the electron cloud of ^{87}Rb.

atom from the liquid drop model, so $r_{\rm nuc} = 1.25 \times 10^{-15}\ A^{1/3}$ m, where A is the atomic mass number. Above the line, the atom is unscreened, so the factor is unity, and below the line it is screened, so the screening factor falls below unity.

As a point of comparison, the red line in Fig. 5.9 shows $\lambda_2 = 1$ calculated using parameters from the electron cloud. For R_2 I take the measured covalent radius of the ^{87}Rb atom, so 235±5 pm [60].

Plotting the constraints together

Now, having investigated the terms in equation (5.19), I am able to show how my measurement of a_χ constrains Λ and M. The contours in Fig. 5.10 show the anomalous acceleration in units of gravity on Earth g. Shaded in gray is the parameter space excluded by the experiment presented in this thesis. The solid black line is for $\Lambda_0 = 2.4$ meV, the the value corresponding to the universal acceleration measured by the Planck Collaboration [61, 62], see appendix B. In this plot, I show the regimes discussed above: a) is the pressure (left) versus size (right) boundary for $\phi_{\rm bg}$, b) is the line $\lambda_2 = 1$, the screening of the atoms (to the left is screened and to the right is unscreened), and c) is the line $\lambda_1 = 1$, the screening of the source mass (to the

left is screened and to the right is unscreened). All these regimes shape how my measurement constrains the two parameters. There is an M-insensitive region between a) and b) due to the value $\lambda_2 < 1$ below b) until it lifts off at a) due to changing $\phi_{\rm bg}$ at low $M/M_{\rm Pl}$, the pressure ρ versus size L boundary. In the upper right hand corner, at $M/M_{\rm Pl}$ nearing unity, my measurement stops covering parameter space; this is due to the source mass being screened past $\lambda_1 = 1$ and so a_χ becomes independent of Λ. This can be observed in the straight line turning up in the contours. This means that my experiment has a nearest approach to the planck scale, $M/M_{\rm Pl} = 1$, exactly at this point when a_χ becomes insensitive to Λ. For my experiment, this is $\text{Log}_{10}[M/M_{\rm Pl}] = -0.647$, the black vertical line labelled d) in Fig. 5.10. The calculations and program that led to figures 5.8, 5.9, and 5.10 were made by Prof. E. A. Hinds FRS, for reference [3].

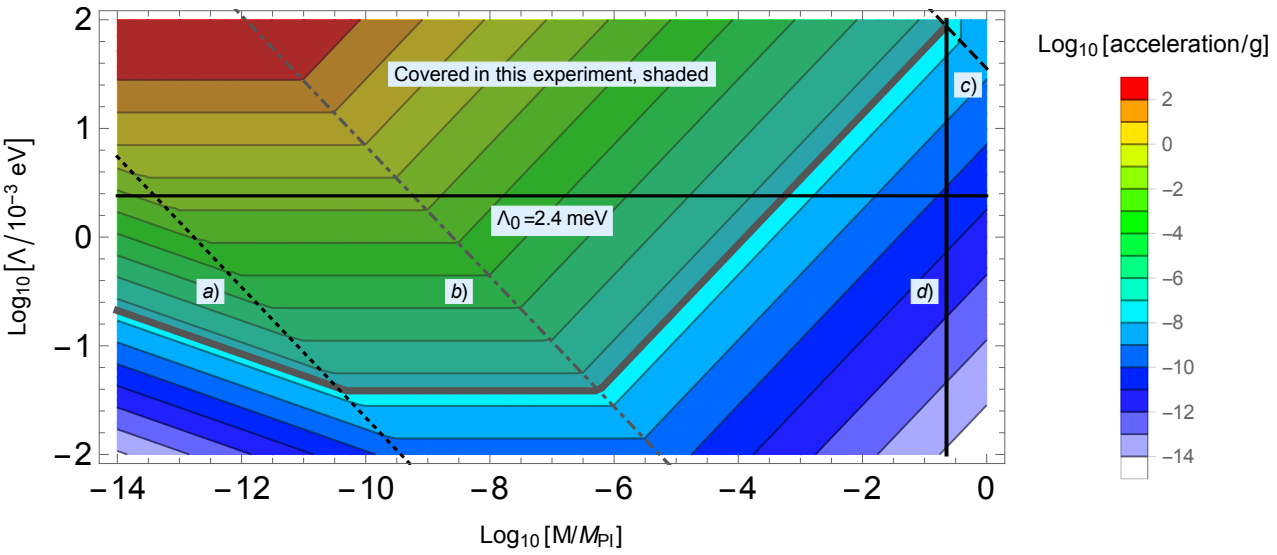

Figure 5.10: Chameleon constraints on Λ versus M from this thesis, $n = 1$ model. Using the 90% confidence bound on a_χ, I place constraints on Λ and M. Shaded in gray is the parameter range tested by the experiment presented in this thesis. The dark energy scale, the cosmological constant i.e. the energy density of the vacuum of space, $\Lambda_0 = 2.4$ meV, is the black line cutting across. a) Coming from $\phi_{\rm bg}$, this is the pressure ρ versus vacuum can size L boundary. b) This liftoff is from the $\lambda_2 = 1$ line, where to smaller values of $M/M_{\rm Pl}$, $\lambda_2 < 1$ and to higher values of $M/M_{\rm Pl}$, $\lambda_2 = 1$. c) This boundary is from $\lambda_1 = 1$; $\lambda_1 < 1$ over almost the entire parameter space. d) this is the closest approach to the reduced Planck mass $M_{\rm Pl}$ in my experiment, due to screening of the source mass: $\text{Log}_{10}[M/M_{Pl}] = -0.647$.

Comparison with other tests

In Fig. 5.11, I show how my experiment, in lavender, compliments other experiments to constrain the parameter space available to the chameleon theory. I use the range of parameters previously established. The black line is $\Lambda = \Lambda_0 \approx 2.4$ meV [61, 62] (see appendix B), and could drive the observed cosmological expansion today.

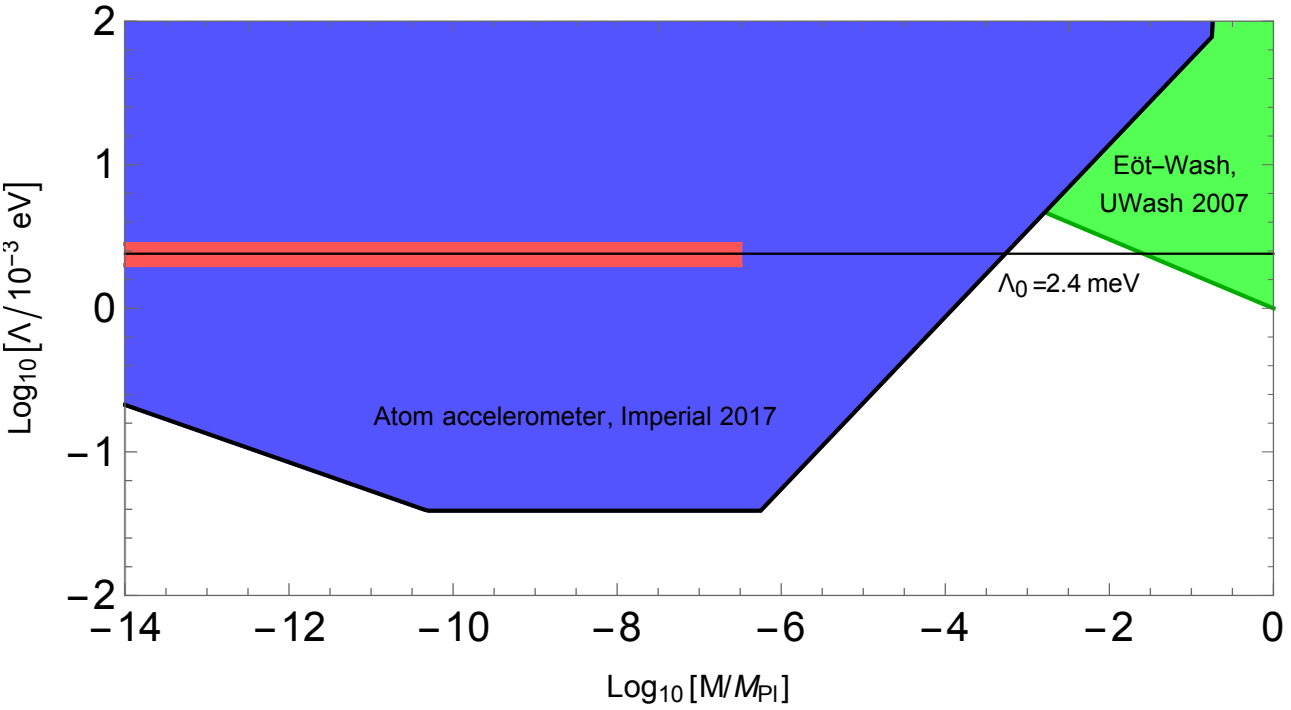

Figure 5.11: Constraints on Chameleon gravity. In lavender is my atom accelerometer experiment. The Eöt-Wash torsion balance experiment is shown in green. Gravitational resonance spectroscopy with ultra-cold neutrons and neutron interferometry constraints are shown in light red. The black line is the energy density of the vacuum of space. Note the small parameter space left open around Λ_0, between $\mathrm{Log}_{10}[M/M_{\mathrm{Pl}}] \sim -1.6 \rightarrow -3.4$.

State-of-the-art torsion balance experiments, namely those of the Eöt-Wash group, consist of a mass that acts as a pendulum that is suspended above a another mass that sources a gravitational field, acting as an attractor [63–65]. The two masses are arranged in a manner that cancels the inverse-square contribution to the total force so that the experiment is sensitive to any deviations. The experiment uses two circular disks as the test masses. These disks have holes bored into them to remove mass. This creates a net torque due to dipole (and higher-order multipole) moments. By rotating the upper disk at an angular velocity such that the contribution from any inverse-square force to the torque is zero, any measured residual force

is non-Newtonian. The group has measured no such force, which places strong constraints on non-inverse-square law modifications of gravity. This includes any scalar-tensor theory where the field is massive, including Yukawa interactions. Constraints due to these tests are wide ranging and shown in light green with a forest green border in Fig. 5.11. Assuming the Planck value of $\Lambda = \Lambda_0$, Neutron interferometry [67,68] places a lower limit on $M/M_{\rm Pl}$ (shown in light red straddling the black line in Fig. 5.11), but my experiment places a more stringent lower limit of -3.4 on $\mathrm{Log}_{10}(M/M_{\rm Pl})$, while the torsion balance experiment places an upper limit of -1.6. This leaves only a small region unconstrained between $\mathrm{Log}_{10}[M/M_{\rm Pl}] \sim -1.6 \rightarrow -3.4$. A different type of atom interferometer experiment has been proposed [69] which might be able to probe this region. This proposed experiment involves using asymmetric parallel plates as the source mass; the plates being asymmetric in terms of their thickness.

During the production of this thesis, the author was made aware of an attempt to constrain these same theories using a different atom interferometer technique, that of a cavity gravimeter [70–72]. That experiment excludes almost exactly the same parameter space as the experiment presented in this thesis, though the boundary line differs in detail due to differences in the chamber geometry, gas pressure, and atom species.

A comment on the symmetron

In this thesis, I focus on chameleon gravity. Closely related to the chameleon scalar field is the symmetron model, with its own screening mechanism [3,35,73]. A symmetron scalar field has an effective potential symmetric under $\phi \rightarrow -\phi$. The simplest effective symmetron potential is of the form

$$V_{\rm eff}(\phi) = \frac{\lambda}{4}\phi^4 + \frac{1}{2}\Big(\frac{\rho}{\mathcal{M}} - \mu^2\Big), \tag{5.23}$$

where λ is the field self-coupling, $\mathcal{M}$ is the suppression scale for the matter coupling, and μ is the potential mass scale; $\mathcal{M}$ and μ are in GeV while λ is dimensionless.

At low densities ρ, V has a double minimum; the field picks one of the minima and breaks the symmetry. It is in this asymmetric phase, with a non-zero field value, that the symmetron

sources a fifth force. At high densities, $\rho > \mu^2 M$, the potential has a single minimum at $\phi = 0$ and no fifth force is sourced. I show the constraints placed on the symmetron parameter space by my experiment in Appendix C; this plot was created by Dr. Clare Burrage.

Chapter 6

Conclusion

6.1 Summary of achievements

I designed and built a complete cold atom experiment that created 5 μK ensembles of ^{87}Rb. After this, I investigated the Raman transition, first with co-propagating beams and, after observing interference fringes, with velocity-sensitive counter-propagating beams. Building up from single pulses to triple pulses, I came to a working acceleration-sensitive atom interferometer. I used it to calibrate a MEMS accelerometer on the back of the retroreflector. I then pressed on to the main experiment, where I made a series of measurements looking for anomalous accelerations. My result was consistent with no anomalous acceleration. This allowed me to exclude most of the parameter space in chameleon theories of modified gravity, and some of the parameter space of symmetron theories.

Applications

This experiment, while primarily scientific, was part of a program to develop atom interferometry for the purpose of measuring accelerations with high sensitivity. This program, funded by the Dstl, aims to integrate an atom interferometer into navigation suites for inertial navigation. Some of the advances made in this work were helpful to this navigation project.

6.2 Improvements for future work

There are several ways in which the experiment could be improved in the future.

(i) [**High importance I**] Improving the number of atoms participating in the interferometer. My state preparation scheme is inefficient. While the state is pure, as shown in Fig. 4.8, the scheme throws most of the atoms away. A factor of 5 improvement in atom number would be gained by optical pumping to drive more atoms into the $|1,0\rangle$ or $|2,0\rangle$ ground state before starting the interferometer. Moving the 2D MOT closer to the 3D MOT chamber could produce an improvement greater than or equal to a factor of four. Having more atoms would open the option of selecting a narrower velocity distribution; for interferometer pulse times presented in chapter 5, this would increase my interferometer contrast and so, for the same amount of data, the acceleration sensitivity.

(ii) [**High importance II**] There can be a time lag between the acceleration and the signal registered by the MEMS accelerometer. These time delays can range up to 10 ms [74–76], depending on the placement of the accelerometer/seismometer; in my system, the accelerometer is directly attached to the retro-reflector. In the experiment I performed in chapter 5, I did not account for any time delay. Subsequently, I checked to see if the noise could be reduced by compensating for a delay. Fig. 6.1 shows the noise measurements of 200 shot fringe patterns, resembling Fig. 4.20, taken with delay times ranging from no delay to 500 μs. The standard error versus delay time exhibits a minimum at a delay of 100 μs. This suggests that the noise in my experiment could be reduced by about 35% if it were run again.

(iii) [**Modified technique I**] Launching the atoms can increase the $2T$ time and so the acceleration sensitivity. In my interferometer time of $2T = 32$ ms, the atoms fall 5 mm. The distance the atoms move is proportional to T^2 and so is the acceleration sensitivity. To double the sensitivity, I must double the distance covered; to keep the atoms within range of the source mass, this would require an increasingly larger mass which will then begin to interfere with Raman beam and producing a significant ϕ_{bg}. If the atoms were launched in an arc against gravity, as originally specified in [3], the time would be doubled but the distance travelled folds

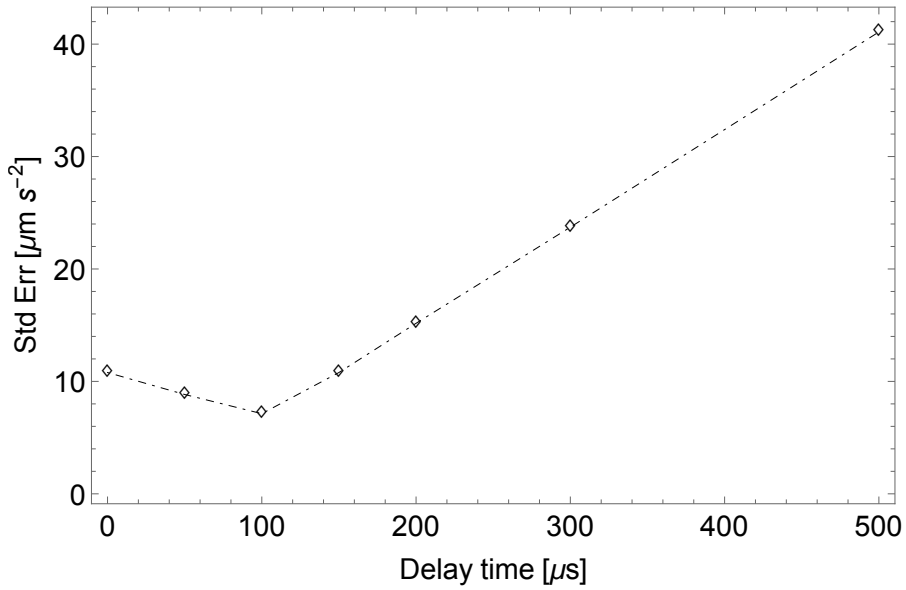

Figure 6.1: Delay time trials. Small datasets similar to Fig. 4.20 were taken for varying delay times. Fitting these fringes and considering the standard error on the offset acceleration creates the trend shown.

on top of itself; doubling the time $2T$ with launching would give me a factor 4 improvement in sensitivity.

(iv) [**Modified technique II**] Another way to improve the sensitivity of the interferometer is to increase the number of momentum recoils received. While this scales linearly with k_{eff} by comparison to quadratically for the time T, it is still useful for increasing sensitivity. One way to do this is to use multiple π and $\pi/2$ Raman pulses in the interferometer sequence.

(v) [**Small technical point**] Laboratory temperature stability drift in the lock point of the reference and repump lasers for the MOT, limiting datasets to 4000 to 15000 shots before a laser would unlock. Improvements to the temperature stability of the lab is one solution. Another would be to improve the technique that frequency stabilizes the lasers.

These improvements, (i) through (v), would readily allow the experiment to reach nm s^{-2} sensitivity.

Acknowledgements

I would be remiss to not thank the following for their contributions to my thesis, in no particular order:

- Jon Dyne, professional mechanical engineer: for machining, vacuum know-how, the occasional and often warranted kick in the rear, and all the hard and clever work you put in to this project. You have my undying gratitude and respect. I really look up to you.

- Sanja Maricic, my co-advisor: You kept it all together for me. Thank you a thousand times over for putting up with the nightmare that was taking care of me; without your undying support, I would have either quit or been dragged out by immigration... I loved every celebration, every afternoon spent helping you, and will miss our chats. Take care, I'll see you soon!

- Steve Maine, David Williams and Giovanni Marinaro, all of the mechanical workshop: for their machining assistance on various jobs, major and minor. Good times!

- Valerijus Gerulis, professional electronics engineer: for help with electronics and power supplies... good fun talking to you. I'll miss you! Expect emails from me on occasion, asking for designs and advice!

- Judith Baylis, coordinator: Thank you for your help guiding me through everyday business with the EU... your help was invaluable in bringing me to the UK and keeping me here. Loved our morning chats!

- Dr. Clare Burrage, cosmologist and collaborator: for being so passionate, interested and helpful. You helped make this entire thesis possible and I'm indebted to you. I'll be in touch, we can't let these theories slip past us without proper tests!

- Tobias Rechberger, Dr. Tobias Jenke, and Prof. Dr. Hartmut Abele of the reactor squad: for letting me anywhere near your fascinating experiment... I had the time of my life working with you all at the ILL in Grenoble. I hope to be back soon to contribute more!

- Dr. Indranil Dutta, postdoc and friend: We had some great times. Thanks for being there and keeping me sane.

- The venerable Prof. E. A. Hinds FRS, my advisor: It was all good fun. Of particular note is how regularly we realized I was probably the luckiest graduate student in CCM. I've learned so much from you I could fill a book. I hope this thesis will suffice, for now.

Appendix A

Magnetic field sensitivity

In chapter 5, equation (5.15), I give an expression for the phase shift to the interferometer due to a magnetic field gradient. I will show here how one arrives at this result. This is based on the work of Prof. E. A. Hinds FRS.

In the rest frame of the atom an applied magnetic field of magnitude $B(\vec{r})$, where $\vec{r}$ the position of the atom. I will Taylor expand the field and consider terms up to the gradient,

$$B(\vec{r}) = B_0 + \vec{\nabla}B \cdot \vec{r}. \tag{A.1}$$

I describe the position of the atom by $\vec{r}(t) = \vec{v}_0 t + \frac{1}{2}\vec{a}t^2$. I use states that are only sensitive to the second-order Zeeman shift ($m_f = 0$). The hyperfine interval has a Zeeman frequency shift, given as a function of time by

$$f(t) = \alpha\Big(B_0 + \vec{\nabla}B \cdot \vec{r}(t)\Big)^2 \simeq \alpha B_0^2 + 2\alpha B_0 \vec{\nabla}B \cdot \vec{r}(t). \tag{A.2}$$

For the first free propagation time T, the corresponding accumulated phase shift is $-2\pi \int_0^T f(t)\mathrm{d}t$. The application of a π pulse swaps the population in states $F = 1$ and $F = 2$, giving a sign flip. The phase accumulated over the second time T is $2\pi \int_T^{2T} f(t)\mathrm{d}t$. The total phase shift of

the interferometer is therefore,

$$\delta\phi = 4\pi\alpha B_0 \vec{\nabla} \cdot \Big(\int_T^{2T} \vec{r}(t)\mathrm{d}t - \int_0^T \vec{r}(t)\mathrm{d}t \Big) = 4\pi\alpha B_0 \vec{\nabla} B \cdot (\vec{v}_0 T^2 + \vec{a} T^3), \tag{A.3}$$

The magnitude of B is only sensitive (in first order) to changes of B_r, the field component along the Raman beam axis, allowing me to replace $\vec{\nabla} B$ with $\vec{\nabla} B_r$. The acceleration $\vec{a}$ is vertical, so along gravity, allowing me to replace $\vec{a}$ by $-g\hat{z}$. The initial velocity is $\vec{v}_0 = 0$. Therefore,

$$\delta\phi = -4\pi\alpha B_0 \frac{\partial B_r}{\partial z} g T^3. \tag{A.4}$$

I want to know how this phase shift due to the magnetic field gradient equates to a false acceleration δa measured by the interferometer along the Raman beam axis. Using the relation $\phi = k_{\text{eff}}\, \delta a\, T^2 \simeq \frac{4\pi}{\lambda}\, \delta a\, T^2$, I can write

$$\frac{4\pi}{\lambda}\, \delta a\, T^2 = -4\pi\alpha B_0 \frac{\partial B_r}{\partial z} g T^3, \tag{A.5}$$

and solving for δa,

$$\delta a = -\alpha B_0 \frac{\partial B_r}{\partial z} g \lambda T, \tag{A.6}$$

This is equation (5.16).

Appendix B

SI to GeV conversion

It is useful, for section 5.3, to establish how to convert SI units to GeV.

Table B.1: SI to GeV conversions

SI	GeV
Meters	$(\frac{e}{\hbar c} \times 10^9)$ GeV^{-1}
Seconds	$(\frac{e}{\hbar} \times 10^9)$ GeV^{-1}
Kilograms	$(\frac{c^2}{e} \times 10^{-9})$ GeV
Kelvins	$(\frac{k_B}{e} \times 10^{-9})$ GeV
Joules	$(\frac{1}{e} \times 10^{-9})$ GeV

The Planck mass, expressed in GeV: $M_{\rm Pl} \rightarrow \frac{1.22}{\sqrt{8\pi}} \times 10^{19}$ GeV. One can calculate $\Lambda_0 = 2.4$ meV, the physical scale that could describe the accelerating expansion of the universe, using the above. This is calculated from the the dark energy density required to completely explain the present rate of expansion [62].

$$\rho_{\rm DE} \sim 10^{-29}\ {\rm g/cm}^3 \approx (2.4\ {\rm meV})^4. \tag{B.1}$$

Interestingly enough, using the above numbers one can obtain a length scale that clearly explains

the interest in sub-millimeter forces,

$$\lambda_{\mathrm{DE}} = \sqrt[4]{\frac{\hbar c}{\rho_{\mathrm{DE}}}} \approx 0.085 \text{ mm}. \tag{B.2}$$

Appendix C

Symmetron constraints

In this thesis, I focus my attention on the chameleon field. This experiment is also a test of similar scalar field theories; of particular note is the symmetron theory. The plot below shows the constraints placed on the parameter space open to the symmetron by this experiment. This has been provided by Dr. Clare Burrage.

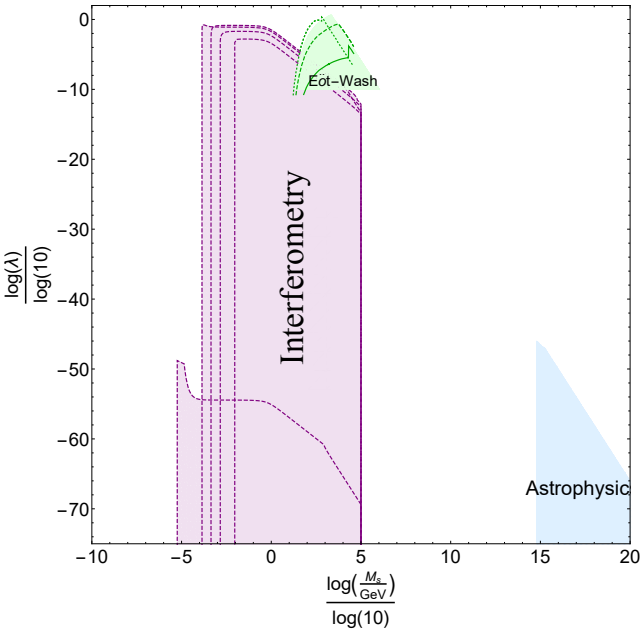

Figure C.1: Constrained symmetron parameter space, M_S vs λ for different values of μ. For the atom interferometer constraints, the different dashed lines correspond to choices of $\mu = \{10^{-4}, 10^{-4.5}, 10^{-5}, 10^{-6},\ 2.4 \times 10^{-3}\}$ eV from top to bottom [73]. The Eöt-Wash bounds are for values $\mu = \{10^{-4}, 10^{-3}, 10^{-2}\}$ eV, displayed by the solid, dashed and dotted green lines respectively. The astrophysical bounds are insensitive to the value of μ.

Bibliography

[1] J. Khoury and A. Weltman. *Phys. Rev. D* **69**, 044026 (2004).

[2] D. F. Mota and D. J. Shaw. *Phys. Rev. D* **75**, 063501 (2007).

[3] C. Burrage, E. J. Copeland, and E. A. Hinds. *JCAP* **03**, 042 (2015).

[4] Alexander Franzen, GW Optics component library.

[5] M. Kasevich and S. Chu. *Phys. Rev. Lett.* **67**, 181-184 (1991).

[6] P. D. Lett, R. N. Watts, C. I. Westbrook, W. D. Phillips, P. L. Gould, and H. J. Metcalf. *Phys. Rev. Lett.* **61**, 169172 (1988).

[7] N. F. Ramsey. "Molecular Beams", Oxford University Press, Oxford (1956).

[8] Ch. Bordé. *Phys. Lett. A*, **140** 10 (1989).

[9] Ch. Bordé and J. L. Hall. "Laser Spectroscopy", Plenum Press, New York (1973).

[10] D. S. Weiss, B. C. Young and S. Chu. *Appl. Phys. B*, **59**, 217 (1994).

[11] A. Bertoldi, G. Lamporesi, L. Cacciapuoti, M. De Angelis, M. Fattori, T. Petelski, A. Peters, M. Prevedelli, J. Stuhler, and G. M. Tino. *Eur. Phys. J. D* **40**, 271 (2006).

[12] F. Sorrentino, Y.-H. Lien, G. Rosi, L. Caccoapuoti, M. Prevedelli, and G. M. Tino. *New J. Phys.* **12** 095009 (2010).

[13] S. Dimopoulos, P. W. Graham, J. M. Hogan, M. A. Kasevich, *Phys. Rev. D.* **78**, 042003 (2008).

[14] S. Dimopoulos, P. W. Graham, J. M. Hogan, and M. A. Kasevich. *Phys. Rev. Lett.* **98**, 111102 (2007).

[15] A. Louchet-Chauvet, T. Farah, Q. Bodart, A. Clairon, A. Landragin, S. Merlet, and F. P. D. Santos. *New J. Phys.* **12**, 065025 (2011).

[16] A. Peters, K. Y. Chung, and S. Chu. *Metrologia* **38**, 25 (2001).

[17] T. Müller, M. Gilowski, M. Zaiser, P. Berg, C. Schubert, T. Wendrich, W. Ertmer, and E.M. Rasel. *Eur. Phys. J. D* **53**, 273 (2009).

[18] E.J. Copeland, M. Sami, and S. Tsujikawa. *Int. J. Mod. Phys. D* **15**, 1753-1936 (2006).

[19] S. Perlmutter *et al. Astrophys. J.* **517**, 565 (1999).

[20] A. G. Riess *et al. Astron. J.* **116**, 1009 (1998); *Astron. J.* **117**, 707 (1999).

[21] A. G. Riess *et al.* [Supernova Search Team Collaboration], *Astrophys. J.* **607**, 665 (2004).

[22] R. Jimenez, P. Thejll, U. Jorgensen, J. MacDonald, and B. Pagel. *MNRAS* **282**, 926 (1996).

[23] H. Richer *et al. Astrophys. J.* **574**, L151 (2002).

[24] B. Hansen *et al. Astrophys. J.* **574**, L155 (2002).

[25] D. N. Spergel *et al.* [WMAP Collaboration], arXiv:astro-ph/0603449.

[26] W. L. Freedman *et al. Astrophys. J.* **553**, 47 (2001).

[27] M. Tegmark *et al.* [SDSS Collaboration], *Phys. Rev. D* **69**, 103501 (2004).

[28] U. Seljak *et al. Phys. Rev. D* **71**, 103515 (2005).

[29] S. Weinberg. *Rev. Mod. Phys.* **61**, 1 (1989).

[30] Van der Bij, J. J. H. Van Dam, and Y. J. Ng. *Physica* **116A,** 307 (1982) and W. Buchmuller and N. Dragon. *Phys. Lett. B* **207**, 292 (1988).

[31] E. Baum. *Phys. Lett. B* **133**, 185 (1983); S.W. Hawking. *Phys. Lett. B* **134**, 403 (1984); S. R. Coleman. *Nucl. Phys. B* **310**, 643 (1988).

[32] S. Kachru, M. Schulz, and E. Silverstein. *Phys. Rev. D 62*, 045021 (2000); N. Arkani-Hamed, S. Dimopoulos, N. Kaloper, and R. Sundrum. *Phys. Lett. B* **480**, 193 (2000); S.-H. Tye and I. Wasserman. *Phys. Rev. Lett.* **86**, 1682 (2001); H. T. Cho, C. L. Ho and K. W. Ng. arXiv:hep-ph/0508018.

[33] P. Fre, M. Trigiante and A. Van Proeyen. *Class. Quant. Grav.* **19**, 4167 (2002); M. de Roo, D. B. Westra and S. Panda. *JHEP* **0302**, 003 (2003); Y. Aghababaie, C. P. Burgess, S. L. Parameswaran and F. Quevedo. *Nucl. Phys. B* **680**, 389 (2004).

[34] R. Garattini. *Nucl. Phys. Proc. Suppl.* **88**, 297 (2000); *Int. J. Mod. Phys. D* **4**, 635 (2002).

[35] K. Hinterbichler and J. Khoury. *Phys. Rev. Lett.* **104**, 231301 (2010).

[36] K. Moler, D. S. Weiss, M. Kasevich, and S Chu. *Phys. Rev. A* **45** (1992).

[37] M. Kasevich and S. Chu. *Appl. Phys. B* **54**, 321 (1992).

[38] SAES Alkali dispenser catalog

[39] Vacuum Technology, Pfeiffer Vacuum (2017).

[40] A. S. Arnold, J. S. Wilson, and M. G. Boshier. *Rev. Sci. Instrum.* **69**, 1236 (1998).

[41] C. P. Pearman, C. S. Adams, S. G. Cox, P. F. Griffin, D. A. Smith, and I. G. Hughes. *Journal of Physics B* **35**, 24 5141 (2002).

[42] Samuel Pollock. Integration of Magneto Optical Traps in Atom Chips. PhD thesis, Imperial College London (2010).

[43] D. A. Steck. *Rubidium 87 D Line Data Version 2.1.5*, (2015).

[44] G. Ritt, G. Cennini, C. Geckeler and M. Weitz. *Appl. Phys. B* **79**, 363 (2004).

[45] Benjamin Canuel. Étude d'un gyromètre à atomes froids, PhD thesis. Université Paris Sud - Paris XI, 2007. French.

[46] H. J. Metcalf and P. van der Straten. "Laser Cooling and Trapping" Springer-Verlag, New York (1999).

[47] C. J. Foot. "Atomic Physics", Oxford University Press, Oxford (2005).

[48] Aviv Keshet, Cicero Word Generator and Atticus Hardware Server, (2008).

[49] P. Cheinet, B. Canuel, F.P.D. Santos, A. Gauguet, F. Yver-Leduc and A. Landragin. *IEEE Transactions on Instrumentation and Measurement* **57** (2008).

[50] N. F. Ramsey. *Physical Review* **78** (1950).

[51] M. Kasevich, D. S. Weiss, E. Riis, K. Moler, S. Kasapi, S. Chu. *Phys. Rev. Lett.* **66**, 2297 (1991).

[52] G. E. Harrison, M. A. Player, and P. G. H. Sandars. *J. Phys. E: Sci. Instrum.* **4**, 750 (1971).

[53] J. J. Hudson, M. R. Tarbutt, B. E. Sauer, and E. A. Hinds. *New J. Phys.* **16**, 013005 (2014).

[54] M. S. Safronova, D. Jiang, B. Arora, C. W. Clark, M. G. Kozlov, U. I. Safronova, and W. R. Johnson. *IEEE Transactions on Ultrasonics, Ferroelectrics and Frequency Control* **57** (2010).

[55] D. M. Kara, I. J. Smallman, J. J. Hudson, B. E. Sauer, M. J. Tarbutt, and E. A. Hinds. *New Journal of Physics* **14**, 103051 (2012).

[56] MKS instruments, Gas Correction Factors for Ionization Vacuum Gauges, Technical information, 2018.

[57] J. Jaeckel and S. Roy. *Phys. Rev. D* **82**, 125020 (2010).

[58] C. Schwob, L. Jozefowski, B. de Beauvoir, L. Hilico, F. Nez, L. Julien, F. Biraben, O. Acef, J.J. Zondy, and A. Clairon. *Phys. Rev. Lett* **82**, (1999).

[59] G. Simon, C. Schmitt, F. Borkowski, and V.H. Walther. *Nucl. Phys. A* **333**, (1980).

[60] J. C. Slater. *J. Chem. Phys.* **41**, 3199 (1964).

[61] Planck Collaboration. Planck 2013 results. arxiv: 1303.5076

[62] P. J. Steinhardt and N. Turok. *Science* **312**, 1180-1183 (2006)

[63] D. J. Kapner, T. S. Cook, E. G. Adelberger, J. H. Gundlach, B. R. Heckel, C. D. Hoyle, and H. E. Swanson. *Phys. Rev. Lett.* **98** 021101 (2007).

[64] E. G. Adelberger, B. R. Heckel, S. A. Hoedl, C. D. Hoyle, D. J. Kapner, and A. Upadhye. *Phys. Rev. Lett.* **98**, 131104 (2007).

[65] A. Upadhye. *Phys. Rev. D* **86**, 102003 (2012).

[66] A. D. Rider, D. C. Moore, C. P. Blakemore, M. Louis, M. Lu, and G. Gratta. *Phys. Rev. Lett.* **117**, 101101 (2016).

[67] H. Lemmel, P. Brax, A. N. Ivanov, T. Jenke, G. Pignol, M. Pitschmann, T. Potocar, M. Wellenzohn, M. Zawisky, and H. Abele. *Phys. Lett. B* **743** (2015)

[68] K. Li, M. Arif, D. G. Cory, R. Haun, B. Heacock, M. G. Huber, J. Nsofini, D. A. Pushin, P. Saggu, D. Sarenac, C. B. Shahi, V. Skavysh, W. M. Snow, and A. R. Young. *Phys. Rev. D* **93** 062001 (2016).

[69] C. Burrage, E. J. Copeland, and J. A. Stevenson. *JCAP* **08**, 070 (2016).

[70] P. Hamilton, M. Jaffe, J. M. Brown, L. Maisenbacher, B. Estey, and H. Müller. *Phys. Rev. Lett.* **114**, 100405 2015.

[71] P. Hamilton, M. Jaffe, P. Haslinger, Q. Simmons, H. Müller, and J. Khoury. *Science* **349**, 849-851 (2015).

[72] M. Jaffe, P. Haslinger, V. Xu, P. Hamilton, A. Upadhye, B. Elder, J. Khoury, and H. Müller. *Nature Physics* **13**, 938942 (2017).

[73] C. Burrage and J. Sakstein. *Living Rev. Relativity* **21**, 1 (2018).

[74] J. Lautier, L. Volodimer, T. Hardin, S. Merlet, M. Lours, F.P.D. Santos, A. Landragin. *Appl. Phys. Lett.* **105**, 144102 (2014).

[75] S. Merlet, J. Le Gouet, Q. Bodart, A. Landragin, F.P.D. Santos and P. Rouchon. *Metrologia* **46**, 87-94 (2009).

[76] Indranil Dutta. Stability improvement of a sagnac cold atom interferometer : towards continuous operation, PhD thesis. Université Pierre et Marie Curie - Paris VI, 2015. English.